The Dissertation Committee for Jason Dale Jaacks
certifies that this is the approved version of the following dissertation:

# The Birth of Cosmic Complexity

Committee:

Volker Bromm, Supervisor

Steve Finkelstein, Co-Supervisor

Shardha Jogee

Michael Boylan-Kolchin

Milos Milosavljevic

Naoki Yoshida

# The Birth of Cosmic Complexity

**by**

**Jason Dale Jaacks**

**DISSERTATION**

Presented to the Faculty of the Graduate School of

The University of Texas at Austin

in Partial Fulfillment

of the Requirements

for the Degree of

**DOCTOR OF PHILOSOPHY**

THE UNIVERSITY OF TEXAS AT AUSTIN

May 2018

Dedicated to all my family, friends and colleagues who have supported me on this journey.

# The Birth of Cosmic Complexity

Publication No. _____

Jason Dale Jaacks, Ph.D.
The University of Texas at Austin, 2018

Supervisors: Volker Bromm
Steve Finkelstein

In this thesis, we construct custom built sub-grid models for the first and second generation of stars, the so-called Population III and II (Pop III/II). Implementing them in the state of the art hydrodynamical/N-body code GIZMO, we explore the legacy left by star formation processes in the first billion years of the Universe. With this powerful tool, we are able to create a virtual universe in a computational box with which we can study, in detail, the processes of star and galaxy formation. This technique is well suited to investigate epochs in cosmic history which are currently still beyond the reach of existing telescopes. More specifically, we examine how Pop III stars, which form from primordial, metal-free gas, leave behind a legacy of metal enrichment, thus setting the stage for the observable second generation of stars and first galaxies. They also begin the process of creating the basic chemical building blocks, the elements beyond H and He, for everything we know. We have found that Pop III star formation continues at a high rate down to $\sim$ 750 million

years after the Big Bang. While we find that Pop III dominated galaxies are likely to remain beyond our view, the inferred high rate of star formation could lead to the detection of the theorized pair-instability supernova (PISN), thought to be the consequence of the death of high mass Pop III stars. We also find that the metal enrichment provided by the death of Pop III stars is insufficient to significantly redden the spectrum from the first galaxies, but that it is critical to determining where and when the second generation of stars forms. Finally, we are able to quantify the number density of galaxies with specific brightness to determine that the number of galaxies at low luminosities assumes a near-plateau value. This is in contrast to the current paradigm, where it is assumed that this number will continue to grow along a power-law track. With the launch of the next generation James Webb Space Telescope (*JWST*) on the horizon, this thesis provides key constraints for future frontier observations.

# Table of Contents

# List of Tables

# List of Figures

# Chapter 1

# Introduction

## 1.1 Motivation

Approximately 400,000 years after the Big Bang the Universe has cooled sufficiently enough that electrons are able to recombine with the primordial plasma and emit photons. These cosmic microwave background (CMB) photons are the last which will be allowed to propagate freely through the Universe for more than 100 million years. This period in cosmic evolution is often referred to as the cosmic "dark ages" and consists of neutral, homogeneous, isotropic gas which is made up of mostly hydrogen and helium. One of the greatest quests in astronomy is understanding how we got from this dark, homogeneous, isotropic Universe to the bright, complex, structure filled Universe we reside within. In part, the understanding can be gained through the study of the life and death of the first stars and galaxies.

Big Bang nucleosynthesis (BBN) details the primordial composition of the Universe mere seconds after its inception. Primarily made up of hydrogen, helium and trace amounts of lithium, the Universe is devoid of all heavier elements (i.e. metals) and remains metal free until the process of stellar nucleosynthesis begins with the formation of the first generation of stars, so-called population III stars (Pop III). By definition these stars are metal free as they form directly from primordial

gas clouds. Since metals are the primary agent by which gas can radiatively cool, temperatures in Pop III star forming regions are much higher which leads to Pop III stars having higher typical masses than their second generation (Pop II) counterparts as the mass at which a gas cloud becomes gravitationally unstable is proportional to the gas temperature to the three halves power ($M_{\rm J} \propto T^{3/2}$) . More massive stars have the ability to generate large amounts of metals through fusion in short evolutionary time scales (~few Myr), which can then be returned to the interstellar medium (ISM) through supernova processes.

The enrichment of the ISM with metals is the primary contribution of the first generation of stars (Pop III) to the galactic evolutionary sequence. This enrichment sets the stage for the second generation of stars (Pop II) to form and assemble into the first massive galaxies in the early universe, which have been the targets of many Hubble Space Telescope (*HST)* large surveys such as CANDELS (PI Faber & Ferguson), HUDF09/UDF12 (PI Illingworth/Ellis), BoRG (PI Trenti) and the *HST* Frontier Fields (PI Lotz). This makes quantifying the enrichment history of the Universe of particular interest to the observing community as it helps to pinpoint where and when the first observable galaxies can be observed.

More massive stars also produce a larger number of photons possessing energies sufficient enough to ionize hydrogen ($h\nu > 13.6$ eV). This means that Pop III could also play an important role in the beginning of the end of the cosmic dark ages. A process know as reionization which takes the Universe from a neutral, homogeneous medium to a mostly ionized, structure filled Universe. Observations and models are able to roughly constrain the reionization history of the Universe

predicting a quick transition from neutral to mostly ionized between 450 Myr to 1 Gyr after the Big Bang. This history is highly dependent on the number of ionizing sources (i.e stars and galaxies). Unfortunately, even the most powerful telescopes are unable to probe deep enough into the cosmic dark ages to constrain all of the sources of ionizing photons, making numerical experiments, such as the work presented here, valuable tools to peering into a dark Universe.

Advances in computational power and sophisticated numerical algorithms have allowed modern astronomers/physicists to explore beyond the limited number of photons which reach our telescopes. We are essentially able to create a universe in a box with which we can conduct numerical experiments to gain insight into the fundamental physics which drive the systems we observe. The past two decades have seen tremendous advancement in the field of computational astrophysics. From Navarro et al. (1997) which utilized only gravitationally interacting particles (N-body) to study the profiles of dark matter haloes, to contemporary cosmological volume simulations which contain sophisticated sub-grid physics designed to study gas dynamics, star formation, chemistry, cosmic rays, and radiation transport along with their complex interplay in the context of galaxy formation.

Observations combined with numerical simulations and classic theoretical physics have provided tremendous insight into the key physics which govern the formation of the first stars and subsequent first galaxies. The work presented in this dissertation leverages the insights gained and advancements made over the past decades to create a new suite of cosmological volume simulations which are specifically designed to mimic future frontier observation from *JWST*. Our custom

built sub-grid physics modules are designed to take advantage of our meso-scale resolutions and produce representative galaxy populations with which we can make predictions for the next generation of ground and space based telescopes.

## 1.2 Outline

In **Chapter 2** we detail the numerical methods and physics which governs our Pop III legacy star formation model (P3L). We then create an idealized simulation in which Pop III star formation is the only star mode aloud. With this applied constraint we are able to study the baseline enrichment from Pop III stars only. In this chapter we compare our work to previous numerical experiments and current cutting edge observations which provide valuable constraints for our sub-grid models. We then explore the mean metal enrichment, volume filling fraction and create a simulated spectra for a Pop III only enriched system.

In **Chapter 3** we utilize our P3L model to study the minimum reddening by dust created from Pop III metals. Observations at intermediate redshifts ($z \sim 3$) have shown that $\beta_{\rm UV}$ is correlated with far-infrared (FIR) dust emission (e.g. Meurer et al., 1999; Reddy et al., 2012). These results indicate that UV photons are readily absorbed and scattered by dust grains which are in turn heated, and re-radiating in the far-IR. Our idealized Pop III only simulation allows for the explore what the minimum $\beta_{\rm UV}$ would be in the first galaxies.

In **Chapter 4** we present the numerical methods of our newly developed the Pop II legacy star formation model (P2L). We combine our P3L and P2L star formation models which new metal cooling and UB background physics to create

a new simulation which is specifically designed to emulate a single pointing by the upcoming James Webb Space Telescope (*JWST*). We compare the physical and photometric properties of our simulated galaxies to frontier observations and make key predictions which can be verified (falsified) by the future space and ground telescopes.

In **Chapter 5**, we summarize the work described within this dissertation, and give a brief outlook for future studies.

# Chapter 2

# Baseline Metal Enrichment from Population III Star Formation in Cosmological Volume Simulations[1]

## 2.1 Overview

Massive, short lived, and forming from nearly pristine (metal free) environments, the first generation of stars to form in the Universe, the so-called Population III (Pop III), plays a critical role in the cosmic evolutionary sequence. Metals left behind by the death of Pop III stars in supernova (SN) explosions enrich the early interstellar/intergalactic medium (ISM/IGM) (e.g. Yoshida et al., 2004) to a critical metallicity ($Z_{\rm crit} \sim 10^{-4}\ Z_{\odot}$, Bromm et al., 2001a), required to engender a second generation of low-metallicity, predominantly lower mass Population II (Pop II) stars. The transition from a top-heavy primordial initial mass function (IMF) to a lower mass IMF (Salpeter, 1955; Chabrier, 2003) marks a critical point in cosmic evolution as Pop II stars constitute the high redshift galaxies which are the focus of current surveys (e.g. HUDF, CANDELS, BoRG, HST Frontier fields), and ultimately the old populations of galaxies we observe locally. Further, the UV ionizing photons produced during the life and death of massive Pop III stars make

[1]This chapter has been published as Jaacks J., Thompson R., Finkelstein S. L., Bromm V., 2018, MNRAS, 475, 4396. R. Thompson provided insight into the GIZMO code base. S. L. Finkelstein, and V. Bromm supervised the project.

an important contribution to ending the cosmic dark ages (e.g. Tumlinson & Shull, 2000; Bromm et al., 2001b; Schaerer, 2002, 2003a). This renders understanding where and when Pop III stars formed and evolved essential to understanding galaxy evolution in the first billion years of the Universe.

Due to their short life spans and the epoch in which they dominate cosmic star formation ($z \gtrsim 15$) (e.g. Tornatore et al., 2007; Pallottini et al., 2014; Xu et al., 2016b), direct observations of Pop III stars and star forming regions is beyond the capabilities of even our most powerful telescopes (e.g. Cai et al., 2011; Pawlik et al., 2011; Cassata et al., 2013; Sobral et al., 2015; Kehrig et al., 2015). We therefore must rely on indirect evidence derived from observations of lower redshift systems. Damped Lyman alpha (DLA) and Lyman alpha (Ly$\alpha$) absorbers, as well as Lyman limit systems, can offer insight into the column densities and metallicities of the IGM near distant, faint sources. For example, Rafelski et al. (2014), using high resolution spectroscopy to study DLAs, found evidence that the mean metallicity of neutral gas rapidly drops at $z \sim 5$ to $\langle Z \rangle \simeq 10^{-2.0}\ Z_{\odot}$. Using similar techniques, Simcoe et al. (2012) detected a system of high column density neutral gas at $z$=7.04 (if the system is bound), estimated to have $Z < 10^{-4}\ Z_{\odot}$, which is near the critical metallicity for the Pop III to Pop II transition. However, these systems have only been observed at $z \lesssim 8$, thus showing potential contamination from Pop II star formation. To disentangle any such multi-component enrichment, we must therefore rely on numerical simulations, tracking in detail the contribution from Pop III star formation to the metallicity of the early Universe.

Early analytical efforts to derive the cosmological impact of Pop III star

formation (Carr et al., 1984) considered the contribution of Pop III remnants to the "missing matter" (i.e. dark matter) problem, the contribution to reionization and the enrichment of the IGM. It was determined in this work that the remnants of Pop III stars could significantly contribute to the "missing matter" if their IMF was Salpeter-like, implying a significant number of stars with $M < 0.1 M_{\odot}$. It was also determined that intermediate mass Pop III stars could be an important contributor to reionization and pre-galactic enrichment.

Yoshida et al. (2004) concluded, based on cosmological simulations from Yoshida et al. (2003), that a significant fraction of the IGM could be enriched to a critical value of $10^{-3.5}\ Z_{\odot}$ by $z$=15. It was also concluded that Pop III star formation was a "self-terminating" process due to the rapid enrichment and radiative feedback produced. This result is however based on the assumption that Pop III stars had masses of $100-300\ M_{\odot}$, thus ending their life as pair instability supernovae (PISNe), with metal yields $\sim 5$ times higher compared to their lower mass counterparts. Since this study, advancements in computational power have allowed for simulations with greatly increased mass and spatial resolutions leading to the discovery that, due to fragmentation, not all Pop III stars have masses $> 100\ M_{\odot}$ (Turk et al., 2009; Stacy et al., 2010). Consequently, far fewer PISN events are predicted. The results from Yoshida et al. (2004) can be looked at now as an upper limit for the metallicity evolution.

Utilizing smoothed particle hydrodynamics (SPH) simulations, Tornatore et al. (2007) found that, while experiencing rapid quenching by $z \sim 6$, Pop III star formation could continue down to $z \approx 2.5$, suggesting that direct observations of

systems powered by Pop III stars could be possible. They also concluded that only a small fraction of the baryons at $z = 3$ ($\Omega_{\rm III} \sim 10^{-5}\Omega_b$) are enriched by Pop III star formation only, making detection of Pop III enriched gas regions difficult as the vast majority have been further enriched by subsequent Pop II star formation. While cutting edge at the time, these simulations did not fully track the primary primordial coolants ($H_2$, HD) and lacked the spatial resolution to fully resolve Pop III star forming regions. Further, as with Yoshida et al. (2004), only PISNe were considered for metal feedback/enrichment.

A more recent study by Pallottini et al. (2014) utilized adaptive mesh refinement (AMR) simulations to study the cosmic metal enrichment by the first galaxies. The use of AMR allows for enhanced spatial resolution in pre-selected regions of interest (i.e. high density star forming regions). This work estimates the Pop III star formation rate density (SFRD) to peak at $\sim 10^{-3} M_\odot$ yr$^{-1}$ Mpc$^{-3}$ at $z$=9, which is only a factor of ten lower than the observed SFRD, thought to be dominated by Pop II star formation. It was also estimated that the volume filling fraction of gas with metallicities $Z > Z_{\rm crit}$ is $\sim 10^{-4}$ at $z$=10 and $\sim 10^{-2.5}$ at $z$=6. This estimate however did not distinguish between the contribution of metals originating from Pop III as compared to those from Pop II stars.

Studying the enrichment from Pop III stars only, which is the focus of this work, we are able to determine the baseline enrichment in our simulated Universe. Thus having an estimate for the Pop III metal enrichment will help to provide insight into the impact, frequency, origins and evolutionary path of extremely low metallicity systems such as Cosmos Redshift 7 (CR7), an extremely luminous Lyman-$\alpha$ source

that is seemingly devoid of metals (Sobral et al., 2015), and the Simcoe et al. (2012) DLA. Theoretical studies have suggested that a direct collapse black hole (DCBH) is a more likely explanation for the Sobral et al. (2015) observations (e.g. Pallottini et al., 2015; Smith et al., 2016; Agarwal et al., 2016, 2017; Pacucci et al., 2017). Also, follow up observations of this system have also suggested that it may be more metal enriched than previously estimated (Bowler et al., 2017; Matthee et al., 2017; Sobral et al., 2017). In either case this work will also allow us to provide a heuristic map of CR7-type objects which can be utilized by current HST wide field surveys and future *James Webb Space Telescope (JWST)* observations and which will probe even earlier epochs where such systems would, in theory, be more numerous (Smith et al., 2017).

In this work we detail a newly developed Pop III star formation model in our cosmological volume simulations and utilize it to study the baseline metal enrichment legacy left by Pop III stars at $z \geq 7$. We would like to point out to the reader, when examining these results, that we are only considering metal enrichment from Pop III star formation. Therefore, what we present here is an idealized numerical experiment, providing an upper limit to the ability of Pop III to enrich the early Universe. The paper is structured as follows. In Section 2.2 we describe the simulations and methods used. Specifically, we provide details of our new Legacy Pop III model in Sec 2.2.1. In Section 2.3 and 2.4 we present our results and conclusions.

## 2.2 Numerical Methodology

This work takes advantage of recent advancements in hydrodynamical numerical techniques through the utilization of the public version of the new GIZMO (Hopkins, 2015) simulation code. GIZMO employs a Lagrangian meshless finite-mass (MFM) method for solving the equations of hydrodynamics which improves on previous generations of smoothed particle hydrodynamics (SPH) and adaptive mesh refinement (AMR) codes (see Hopkins (2015) for method comparison details). In this section, we will describe our newly developed sub-grid physics modules, along with the physical parameters adopted in this work.

Our simulation volume, designed to approximately replicate a single pointing with the *JWST* at redshift $z \sim 10$, has a box size of $4h^{-1}$ Mpc and contains $512^3$ particles of both gas and dark matter. We will refer to this simulation run as N514L4 throughout. Full details of the simulation set-up can be found in Table 2.1. We adopt a $\Lambda$ cold dark matter ($\Lambda$CDM) cosmology, consistent with the recent *Planck* results: $\Omega_m = 0.315$, $\Omega_\Lambda = 0.685$, $\Omega_b = 0.047$, $\sigma_8 = 0.829$, and $H_0 = 67.74$ (Planck Collaboration et al., 2016). Our initial conditions are generated at $z = 250$, using the MUSIC initial conditions generator (Hahn & Abel, 2011).

Primordial chemical abundances and radiative cooling rates are calculated for 12 species (H, $H^+$, $H^-$, $H_2$, $H_2{}^+$, He, $He^+$, $He^{2+}$, D, $D^+$ HD, $e^-$), using methods detailed in Bromm et al. (2002) and Johnson & Bromm (2006), in turn based on earlier work (Cen, 1992; Galli & Palla, 1998). As $H_2$ and HD are the primary low-temperature coolants in primordial gas, it is critical to properly account for their formation and destruction. Therefore, we also include $H_2$ photo-dissociation,

Table 2.1: Simulation parameters used in this paper. The parameter $N_p$ is the number of gas and dark matter particles; $m_{DM}$ and $m_{gas}$ are the particle masses of dark matter and gas; $\epsilon, h_{sml}$ are the comoving gravitational softening length/hydrodynamical smoothing length (adaptive). Both simulation runs utilize the Pop III Legacy model (P3L), detailed in Section 2.2.1, and differ only in the inclusion of the proxy for Pop II star formation (see Section 2.2.3.2).

| Run | Box size (Mpc $h^{-1}$) | $N_p$ (DM, Gas) | $m_{DM}$ ($M_\odot$) | $m_{gas}$ ($M_\odot$) | $\epsilon, h_{sml}$ (kpc) | Pop III model | Pop II model |
|---|---|---|---|---|---|---|---|
| N512L4 | 4.0 | $2\times512^3$ | $4.31\times10^4$ | $9.64\times10^3$ | 0.45 | P3L | None |
| N512L4_P2P | 4.0 | $2\times512^3$ | $4.31\times10^4$ | $9.64\times10^3$ | 0.45 | P3L | P2P |

and photo-detachment of $H^-, {H_2}^+$ in our chemical network (see Section 2.2.3.1 for details).

Dark matter haloes are identified via a post processing 3D friends-of-friends (FOF) algorithm with a minimum particle requirement of 32 and a linking length of 0.15 times the inter-particle distance. Gas particles and their respective properties (mass, temperature, metallicity, density, position) are then associated with each dark matter halo by searching within its virial radius. Grouping and data extraction are aided by the *yt* (Turk et al., 2011) and (Thompson, 2014) software packages.

### 2.2.1 Legacy Pop III star formation

Formation of Pop III stars, and the resulting supernova (SN) pollution of the surrounding medium with metals, is vital to accurately predict where and when the second generation of star formation will occur and, by extension, the first galaxies form. To model Pop III SN explosions in full detail would require sub-parsec scale resolution (e.g. Ritter et al., 2012), which is not achievable in cosmological volume

simulations. Therefore, we implement what we term the "Legacy" approach, where we are concerned with modeling the final impact of an episode of Pop III star formation, specifically the resulting metal enrichment, persistent ionization, and thermal energy, but where we do not model the feedback event itself.

Our Legacy approach allows us to form Pop III stellar populations from a randomly sampled input IMF after which we essentially "paint" fully formed Pop III supernova remnants onto the fluid, centered on the star forming regions with physical properties calibrated with high-resolution simulations (e.g. Greif et al., 2007; Stacy & Bromm, 2013), and with select analytic solutions (Sedov, 1959; Taylor, 1950). Each star formation event gives rise to a stellar population which is randomly drawn from a given initial mass function (IMF). This allows each star forming region to exhibit a unique feedback signature, involving energy and nucleosynthetic yield, as stars with different masses end their lives differently (i.e. type II SN, black hole, pair instability SN). The feedback radius of influence, metallicity, thermal energy and ionization are directly calculated for each individual stellar population. Thereafter, the enriched gas simply advects with the local hydrodynamical flow. This approach enables Pop III star formation to have both time and spatial dependence, rather than the idealized uniform metallicity floor which was implemented in our previous simulations (Jaacks et al., 2012a,b, 2013; Thompson et al., 2014).

#### 2.2.1.1 Star formation criteria

Pop III star formation is triggered when a preset threshold density, $n_{\rm th} = 100$ cm$^{-3}$, is reached for a gas (SPH) particle with $T \leq 10^3$ K and $Z \leq Z_{\rm crit}$. Here,

the critical metallicity required to transition from Pop III star formation to Pop II is $Z_{\rm crit} \approx 10^{-4} Z_{\odot}$ (Bromm et al., 2001a; Schneider et al., 2002). This density is adopted due to the mass/spatial resolution limitations of our simulation volumes, which are only able to resolve molecular cloud scale objects and not the individual star forming clumps contained within. The choice of $n_{\rm th} = 100$ cm$^{-3}$ as our star formation threshold is to ensure that the gas has reached a density such that cooling via molecular processes is efficient.

#### 2.2.1.2 Stellar population

Our mass resolution of $3.0 \times 10^5$ $M_{\odot}$, where $M_{\rm res} = m_{\rm gas} N_{\rm neighbor}$, is insufficient to simulate the formation of individual Pop III stars. Therefore, we assume the formation of a simple stellar population (SSP), with a total mass of $M_{*,\rm Pop\ III} \sim 500 M_{\odot}$. This mass corresponds to a primordial pre-stellar core, as found in high resolution simulations of Pop III star formation in minihalo hosts (Greif et al., 2011; Hirano et al., 2014; Stacy et al., 2016). We adjust the star formation efficiency parameter, $\eta_*$, for each run such that $M_{*,\rm Pop\ III} = \eta_* m_{\rm gas}$. Here $m_{\rm gas}$ is the mass of a single gas particle in a given simulation run (see Table 2.1), implying a Pop III star formation efficiency of $\eta_* \approx 0.05$ (see Table 2.2).

Each star formation event is assigned a unique stellar population which is randomly drawn from a user provided initial mass function (IMF), until the sum of the individual stellar masses exceeds, or is equal to, the desired total mass of the cluster

$$\sum_{i=1}^{N_*} M_{*,i} \geq M_{*,\rm Pop\ III} \tag{2.1}$$

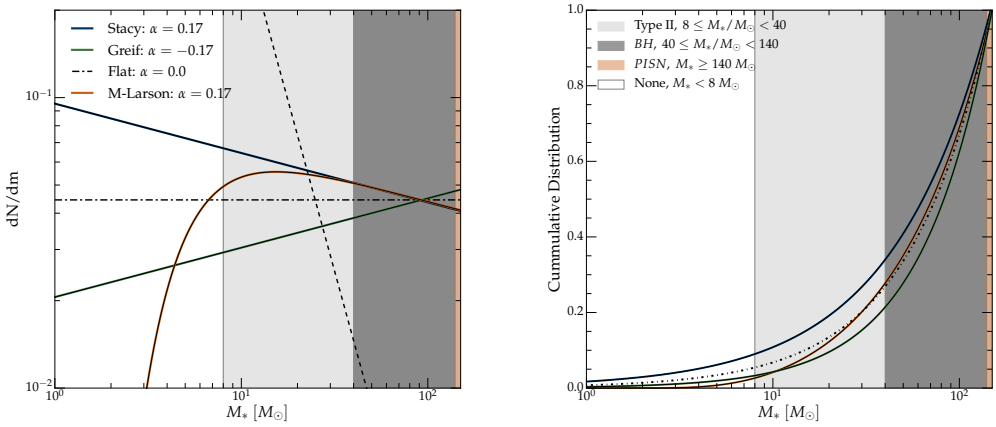


Figure 2.1: *Left:* Compilation of several theoretical models for Pop III initial mass functions which are normalized to our total stellar mass of $M_* = 500 \, M_\odot$. Shown are three power-law IMFs with varying slopes of $\alpha = 0.17, -0.17, 0.0$ (Stacy & Bromm, 2013; Greif et al., 2011), and one which is a modified Larson (1998) IMF with a steeper exponential cut-off, designed to minimize low mass star formation ($\alpha = 0.17, M_{\rm cut} = 4.47 \, M_\odot$). For comparison, the dashed black line represents a power-law with slope $\alpha = 2.35$ (Salpeter, 1955), consistent with a local IMF. *Right:* The cumulative probability distribution function for each of the IMFs shown on the left, utilized for the random draw process in our star formation algorithm. The shaded regions in both panels indicate the mass range associated with the different stellar fates (i.e. no feedback, Type II SN, black hole, or PISNe).

Table 2.2: Mean values of stellar mass, $\langle M_* \rangle$, mean total number of stars, $\langle N_* \rangle$, and fractional contribution to the total number from each mass range, $\langle N_i/N_* \rangle$, calculated for each of the IMFs studied. We derive the averages for $10^5$ unique star forming events, drawn from each of the IMFs indicated.

| Run | IMF | $\alpha$ | $\eta_*$ | $\langle M_* \rangle$ $[M_\odot]$ | $\langle N_* \rangle$ | $\langle N_{\rm TypeII}/N_* \rangle$ | $\langle N_{\rm BH}/N_* \rangle$ | $\langle N_{\rm PISNe}/N* \rangle$ | $\langle N_{\rm lowmass}/N_* \rangle$ |
|---|---|---|---|---|---|---|---|---|---|
| N514L4 | Stacy | 0.17 | 0.05 | 547.57 | 8.12 | 0.25 | 0.62 | 0.06 | 0.07 |
| | Greif | −0.17 | 0.05 | 550.60 | 6.76 | 0.18 | 0.71 | 0.08 | 0.03 |
| | Flat | 0.0 | 0.05 | 549.64 | 7.31 | 0.21 | 0.67 | 0.07 | 0.05 |
| | M-Larson | 0.17 | 0.05 | 548.48 | 7.49 | 0.25 | 0.66 | 0.06 | 0.03 |

Here, $M_{*,i}$ is determined by a random number, uniformly drawn between $[0-1]$, which is then associated with the corresponding stellar mass via a cumulative probability distribution function, derived from the IMF (see Figure 2.1). The summation is required to reach at least the desired stellar mass to avoid biasing our stellar population towards low mass stars in our random draw. We do not insert a "star particle" tracer into the simulation, implying that the information is lost once the feedback loop has completed.

#### 2.2.1.3 Initial Mass Function

The true nature of the Pop III IMF has yet to be determined. From the theory side, the field must rely on high resolution hydrodynamical simulations to study the IMF. Unfortunately, there is no clear convergence from the various studies towards a consensus shape or slope. Due to the lack of metals to cool the primordial gas in the very early Universe, the typical Jeans mass of proto-stellar clouds is thought to lead to higher mass stars when compared to local star formations. Estimates of

typical Pop III stellar masses are on the order of $20 - 100\ M_{\odot}$, in contrast to the $< 1\ M_{\odot}$ we observe locally (Salpeter, 1955). Due to the uncertainty in the Pop III IMF, we present several IMFs from the literature as an illustration the differences.

In Figure 2.1, we present a compilation of Pop III IMFs explored in this study. Three of these have been determined by various studies using high resolution hydrodynamical simulations (Stacy & Bromm, 2013; Greif et al., 2011), and can be characterized by a simple power-law

$$\Phi(M) \propto M_{*}^{-\alpha} \tag{2.2}$$

with $\alpha = -0.17, 0.0, 0.17$. A third option is a modification of the Larson IMF (Larson, 1998), which consists of an exponential cut-off to a power-law slope originally developed to exclude very low mass stars in the local IMF. We utilize this cut-off in much the same way (i.e. reduce the probability of stars with $M_{*} < 8\ M_{\odot}$), and include a modification which squares the exponential terms to promote a more rapid turn-over:

$$\Phi(M) \propto M_{*}^{-\alpha} \exp\left(\frac{-M_{\rm cut}^{2}}{M_{*}^{2}}\right) \tag{2.3}$$

where $\alpha = 0.17$ and $M_{\rm cut} = 4.47\ M_{\odot}$. For contrast we also include a typical local Salpeter IMF (Salpeter, 1955) with a slope of $\alpha = 2.35$ (dashed gray line). We normalize each IMF to the total Pop III mass ($M_{*,\rm PopIII}$) by integrating over a mass range of 1 $M_{\odot}$ to 150 $M_{\odot}$

$$M_{*,\rm PopIII} = A \int_{1}^{150} \Phi(M)\ M_{*}\ dM_{*} \tag{2.4}$$

where A is the normalization constant. This mass range allows for a stellar population which can have several post main-sequence evolutionary outcomes, as follows:

$$\begin{aligned} 140 \leq M/M_{\odot} \leq 150 &\rightarrow \text{Pair} - \text{instability SN (PISN)} \\ 40 \leq M/M_{\odot} < 140 &\rightarrow \text{Black hole (BH)} \\ 8 \leq M/M_{\odot} < 40 &\rightarrow \text{Core collapse SN (Type II)} \\ M/M_{\odot} < 8 &\rightarrow \text{Low mass stars} \end{aligned}$$

Each of which will contribute a different amount of energy and metallicity to the total budget of the subsequent SN remnant (Heger & Woosley, 2002). The upper mass limit is chosen to reflect recent observational constraints on the rarity of PISN events in establishing the fossil chemical abundance record in extremely metal-poor stars (e.g. Fraser et al., 2017).

Prior to implementation into GIZMO, a sample set of $10^5$ stellar populations was generated to determine the ability of our randomly drawn Legacy Pop III SF method to reproduce a global IMF. The results of this test are presented in Figure 2.2, where the histogram gives the distribution of the global population as compared to the input IMF (solid orange line). Evidently, our sampling procedure reproduces the input IMF extremely well. We further illustrate this in Table 2.2, where we provide the mean total mass ($\langle M_* \rangle$), mean total number of stars ($\langle N_* \rangle$), and fractional contribution to the total number from each mass range ($\langle N_i/N_* \rangle$), calculated for each of the IMFs represented by $10^5$ unique star forming events.

We note that, based on the data summarized in Table 2.2 and results presented in Pallottini et al. (2014), our results are mostly insensitive to the detailed choice of Pop III IMF. For this reason, we here only show results for the IMF given by Equation 2.3.

### 2.2.2 Legacy Feedback Prescription

#### 2.2.2.1 Enrichment radius

The physics of the initial SN explosion and the subsequent interaction with the surrounding interstellar medium (ISM) can be described by well-known analytical models for each phase of the expansion. Employing the solution for each phase (i.e. free expansion, Sedov-Taylor, pressure/momentum-driven snowplow), we can robustly predict the radius of the SN shell, $R_{\rm SN}$, which can then be compared to detailed, high-resolution hydrodynamics simulations.

Prior to the SN explosion, ionizing radiation and stellar winds have established a low density region surrounding the host star (see Figure 2.3 for physical properties adopted). Since the supernova remnant (SNR) has a much higher density than the surrounding medium it expands freely at early times. This expansion continues until the mass swept up by the expanding SNR becomes equal to the mass of the ejecta ($M_{\rm sw} = M_{\rm ej} \approx M_{*,\rm PopIII}$). The radius at which this equality occurs can be estimated by

$$r_{\rm fe} \approx \left( \frac{3 X M_{\rm ej}}{4\pi m_p n_H} \right)^{1/3}, \tag{2.5}$$

where $X = 0.76$ is the primordial hydrogen mass fraction, $m_p$ the mass of a proton, and $n_H \approx 0.1$ cm$^{-3}$ the hydrogen number density in the HII region (Kitayama &

Yoshida, 2005). Simple conservation of energy arguments allow us to estimate the time to the end of the FE phase,

$$t_{\rm fe} = r_{\rm fe} \left( \frac{M_{\rm ej}}{2E_{\rm tot,POPIII}} \right)^{1/2}. \tag{2.6}$$

Here, $E_{\rm tot,POPIII}$ is the total supernova energy produced by the Pop III stellar population,

$$E_{\rm tot,PopIII} = \sum_{i=1}^{4} N_i E_i, \tag{2.7}$$

where $N_i$ is the total number of SNe associated with each mass range, as defined in Section 2.2.1.3, and $E_i$ the respective explosion energy (see Table 2.3).

Upon completion of the FE phase, the SNR enters the Sedov-Taylor (ST) phase in which it can be modeled as a point explosion (Sedov, 1959; Taylor, 1950). During this energy-conserving phase, we utilize the well-known scaling for the radius as a function of time, density and energy,

$$r_{\rm st} = \beta \, E_{\rm tot,POPIII}^{1/5} \, \rho_{\rm ISM}^{-1/5} \, t^{2/5}, \tag{2.8}$$

where $\beta \simeq 1.15$ (Draine, 2011), and we take $n_{\rm ISM} \approx 1.0$ cm$^{-3}$.

The ST phase ends when radiative loses become significant, such that energy conservation is no longer a valid assumption. Based on high resolution simulations with conditions similar to our physical assumptions of the first SN explosions, this occurs at $t_{\rm ST,end} \sim 10^5$ yr (Greif et al., 2007). It is at this point that the SNR enters the pressure-driven snowplow phase (PDS), where it reaches into the IGM. At this stage, the evolution is driven by the adiabatic expansion of the hot gas interior to the shell, and will continue until pressure equilibrium is reached between the interior

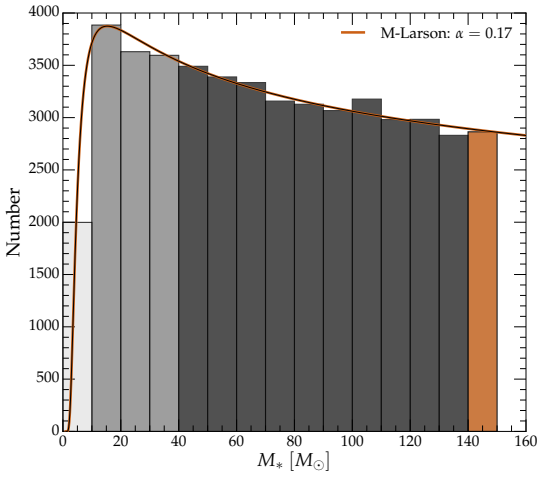


Figure 2.2: Histogram of $10^5$ unique star formation events, randomly drawn from the M-Larson IMF ($\alpha = 0.17$, $M_{\rm cut} = 4.47\ M_\odot$). This test demonstrates that our sampling procedure indeed reproduces the intended global IMF (solid orange line). The shaded regions represent the same mass ranges as in Figure 2.1.

Table 2.3: Energy and fraction of the total stellar mass which is injected into the surrounding medium for each post main-sequence evolutionary outcome adopted, in our model (Karlsson et al., 2013).

| Type | Energy [erg] | Metal yield ($Y_Z$) |
|---|---|---|
| Pair-instability SN | $10^{52}$ | 0.50 |
| Black hole | 0.0 | 0.0 |
| Core collapse SN | $10^{51}$ | 0.10 |
| Low mass stars | 0.0 | 0.0 |

value, $P_i$, and the pressure in the surrounding medium. In this case, we take this medium to be the the IGM, with corresponding pressure $P_{\rm IGM}$.

To derived the PDS scaling, we start with Newton's second law of motion,

$$\frac{d(m_{\rm sw} v_{\rm sh})}{dt} = 4\pi r_{\rm sh}^2 P_i, \tag{2.9}$$

where $m_{sw}$ is the mass ($\propto r_{\rm sh}^3$) and $v_{sh}$ is the velocity of the shell as it travels through the ISM. Given that adiabatic expansion is governed by $PV^\gamma$ = const., where $\gamma = 5/3$, we find that $P_i \propto r_{\rm sh}^{-5}$. For the density scaling, we assume an isothermal profile with $\rho \propto r^{-2}$. Inserting these expressions into Equation. 2.9, we arrive at the following scaling,

$$r_{\rm pds} = r_{\rm st,end} \left( \frac{t}{t_{\rm st,end}} \right)^{2/5}. \tag{2.10}$$

The SNR will continue to expand until it slows to a speed which is comparable to that of the local sound speed, $c_s = \sqrt{k_{\rm B} T_{\rm IGM}/m_{\rm H}}$. We can estimate the velocity during the PDS phase,

$$\frac{dr_{\rm sh}}{dt} = v_{\rm sh} \approx \frac{2}{5} \frac{r_{\rm st,end}}{t_{\rm st,end}} \left( \frac{t}{t_{\rm st,end}} \right)^{-3/5}. \tag{2.11}$$

Setting $v_{\rm sh} = c_s$,we rearrange Equation 2.11 to estimate the time at which the PDS phase ends, $t_{\rm final}$, and the corresponding terminal radius of the SNR, $r_{\rm final}$. Here, we assume that $c_s \approx 10$ km s$^{-1}$, which represents the hot phase of the IGM (i.e. $T_{\rm IGM,hot} \approx 10^4$ K), consistent with an IGM heated by an ionization front preceding the shock front (R-type).

One important omission in the above derivation is the influence of gravity which will act to slow the expanding shell. To account for this, we carry out a simple

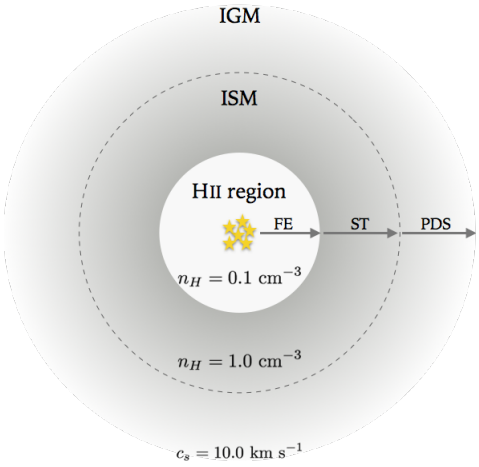


Figure 2.3: Conceptual illustration of typical star-forming region in our model, along with physical properties assumed in each region for the post star-burst, pre-SN phase. Physical properties are taken to be consistent with simulations of $H_{ii}$ regions around Pop III stars (Kitayama & Yoshida, 2005).

comparison of the initial explosion energy to the binding energy of a gas cloud in a typical dark matter minihalo with mass $M_h \approx 10^6\ M_\odot$,

$$E_{\rm bind} \simeq \frac{G M_{\rm vir} M_b}{R_{\rm vir}}, \tag{2.12}$$

where $M_{\rm vir} = 10^6\ M_\odot$, $R_{\rm vir} \approx 100$ pc (at $z$=15) and $M_b \approx \Omega_b/\Omega_m \times M_{\rm vir}$. If $E_{\rm tot,PopIII} < E_{\rm bind}$, we take $r_{\rm sh}$ to be equal to $R_{\rm vir}$. However, if $E_{\rm tot,PopIII} \geq E_{\rm bind}$, we fix the final radius to be at the pressure equilibrium point calculated from Equation 2.11.

In Figure 2.4, we consider the sample of $10^5$ randomly drawn stellar populations from Section 2.2.1.3 to derive a relationship between the final radius and total

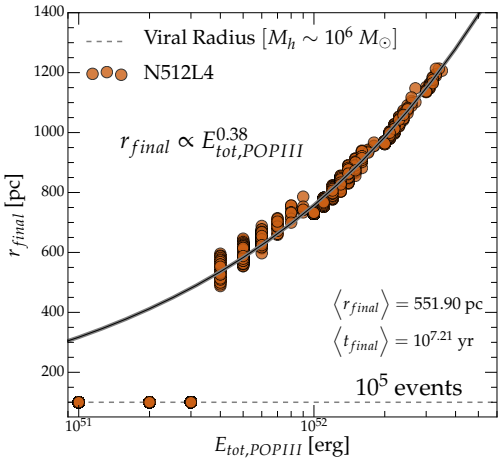


Figure 2.4: Relation between total energy ($E_{\rm tot,PopIII}$) and final enrichment radius ($r_{\rm final}$), derived from a least-square fit (solid line) to the $10^5$ sample (orange circles) stellar populations drawn from the M-Larson IMF. This relation is utilized in our simulation runs to determine the radius for each unique population.

energy injected. A least-squares fit results in

$$r_{\rm final} = R_Z \propto E^{0.38}_{\rm tot,PopIII}\,, \tag{2.13}$$

indicated by the solid line. This relation is clearly an approximation, given that it has been derived under the assumption of spherical symmetry in the explosion, as well as isotropy and homogeneity in the surrounding medium. Conditions in the actual ISM and IGM of these systems will undoubtedly be far more complicated, widely varying from region to region. However, we are encouraged by the fact that our mean final radius, $\langle r_{\rm final} \rangle \approx 550$ pc, is quite consistent with high resolution, single-event simulations by Jeon et al. (2014). Therefore, we adopt Equation 2.13 as our default model in our simulations for the final radius of enrichment.

#### 2.2.2.2 Metallicity Feedback

Enrichment of metals into the surrounding ISM by a single SF event is determined by summing the contribution from each individual member of the randomly drawn Pop III stellar population:

$$M_{\mathrm{Z,PopIII}} = \sum_{i=1}^{4} y_i M_{*,i}, \tag{2.14}$$

where $M_{\mathrm{Z,PopIII}}$ is the metal mass returned to the ISM, $y_i$ is the yield, and $M_{*,i}$ is the total mass in each mass range, defined in Section 2.2.1.3 and Table 2.3. When a SF event occurs, $Z_{\mathrm{tot,Pop\ III}}$ is instantly distributed to the surrounding gas contained within a radius of $r_{\mathrm{final}}$. The enriched material is subsequently advected with the general gas motion, thus setting the foundation for the next generation of star formation.

#### 2.2.2.3 Thermal and Ionization Feedback

While the radius of metal enrichment, $R_Z$, is dictated by the physics of the shock front expanding through the ISM, the thermal and ionization impact of the star forming events is governed by the propagation of photons through the ISM/IGM. The corresponding radius can be estimated with an R-type ionization front, which precedes the shock front, via

$$R_{\mathrm{ion}} = \left( \frac{3\dot{N}_{\mathrm{ion}} \langle N_* \rangle}{4\pi n_{\mathrm{H_I}}^2 \alpha_B} \right)^{1/3} \approx 2\ \mathrm{kpc}. \tag{2.15}$$

This estimation assumes an ionizing flux of $\dot{N}_{\mathrm{ion}} \approx 10^{50}\ \mathrm{s}^{-1}$(Schaerer, 2002), an IGM neutral hydrogen density of $n_{\mathrm{H_I}} \approx 0.10\ \mathrm{cm}^{-3}$, and case-B recombination with $\alpha_B = 2.59 \times 10^{-13}\ \mathrm{cm}^3\mathrm{s}^{-1}$.

It should be noted that we do not impart kinetic energy to the particles in the form of a velocity/momentum change. Rather, this energy is injected into the internal energy of each particle (i.e. thermal energy) at the time of star formation, such that

$$T_i \approx T_{\rm IGM,Hot} \approx 10^4 \ {\rm K} \, . \tag{2.16}$$

This approximation for the interior temperature of the legacy bubble is adopted to be consistent with our radius stalling criterion, i.e. $P_i = P_{\rm IGM}$. We also self-consistently assign the degree of ionization by allowing our chemistry solver to update the mean ionization fraction, $\langle x_e \rangle$, within $R_{\rm ion}$, based on the thermal energy increase. Our choice of values is intended to represent the environment left behind after a SN event has expanded and faded away. Cooling and recombination processes will quickly erase the legacy, imprinted by these parameters (Ritter et al., 2012).

A consequence of our Legacy model is that a stellar population can form, exclusively containing stars that end their lives as black holes or a combination of black holes and low mass stars ($M_* < 8 \ M_\odot$). Both possibilities will leave little to no metallicity imprint on the surrounding environment. They will however emit a large flux of ionizing photons which is deposited within $R_{\rm ion}$. Table 2.4 summarizes both the metallicity radius and the thermal/ionization radius for each evolutionary outcome.

Our instantaneous enrichment scheme is adopted due to the fact that cosmological volume simulations lack the sub-parsec spatial resolution required to model the expanding shell of a SN remnant through the ISM. This approximation is justified by roughly reproducing the results from select high resolution (sub-parsec)

Table 2.4: Summary of radii used in our Legacy model for both the chemical and thermal/ionization feedback for each evolutionary outcome.

| Type | $R_Z$ [pc] | $R_{ion}$ [kpc] |
|---|---|---|
| Pair-instability SN | $\propto E_{\rm tot,POPIII}^{0.38}$ | 2.0 |
| Black hole | 0.0 | 2.0 |
| Core-collapse SN | $\propto E_{\rm tot,POPIII}^{0.38}$ | 2.0 |
| Low-mass stars | 0.0 | 2.0 |

simulations (Jeon et al., 2014).

### 2.2.3 Terminating Pop III Star Formation

#### 2.2.3.1 Lyman-Werner Background

The primary coolant ($H_2$) which leads to the collapse and subsequent formation of Pop III stars is highly susceptible to the radiation produced by Pop III stars. In particular, molecular hydrogen can easily be dissociated by Lyman-Werner (LW) photons, which have energies in the range 11.2 eV to 13.6 eV. To account for the destruction of $H_2$, we implement a self-consistent prescription for a spatially homogeneous LW background with an intensity estimated by,

$$J_{\rm LW,21}(z) \approx 2 \left(\frac{\eta_{\rm LW}}{10^4}\right) \left(\frac{\dot{\rho}_*(z)}{10^{-2} M_\odot \ {\rm yr}^{-1} \ {\rm Mpc}^{-3}}\right) \left(\frac{1+z}{10}\right)^3 . \tag{2.17}$$

Here $J_{21} \equiv J/10^{-21}$ erg s$^{-1}$ cm$^{-2}$ Hz$^{-1}$ sr$^{-1}$, $\eta_{\rm LW}$ represents the number of LW photons produced per stellar baryon and $\dot{\rho}_*$ is the total star formation rate density

(SFRD). To arrive at this normalized equation (e.g. Safranek-Shrader et al., 2012), a stellar population is assumed to last for $\sim 5$ Myr, and the IMF to be top-heavy, for consistency with our Pop III IMF, i.e. $\eta_{\rm LW} \approx 1 \times 10^4$ (Greif & Bromm, 2006).

Rates for both photo-dissociation ($k_{\rm di}$) of $H_2$ and photo-detachment ($k_{\rm de}$) of $H^-, {H_2}^+$ can then easily be calculated by,

$$k_{\rm di} = 1.38 \times 10^{-12}\ \beta\ J_{\rm LW,21} f_{\rm shield,H_2} \tag{2.18}$$

$$k_{\rm de} = 1.10 \times 10^{-10}\ \alpha\ J_{\rm LW,21}\,, \tag{2.19}$$

where $\alpha, \beta$ are parameters that reflect the detailed spectral shape of the incident radiation (see below). We add these photo-processes to our overall chemical reaction network (Abel et al., 1997; Yoshida et al., 2003). The dimensionless factor $f_{\rm shield,H_2}$ accounts for the ability of molecular hydrogen to self-shield against LW photons at high column densities. At $f_{\rm shield,H_2}$=1, the $H_2$ is completely unshielded and susceptible to photo-dissociation, whereas at $f_{\rm shield,H_2}$=0 it is fully shielded from the LW background. This self-shielding factor is calculated in our code using the fit provided by Draine & Bertoldi (1996):

$$f_{\rm shield,H_2} = \frac{0.965}{(1 + x/b_5)^a} + \frac{0.035}{(1+x)^{0.5}} \exp\left[-8.5 \times 10^{-4} (1+x)^{0.5}\right], \tag{2.20}$$

where $x = N_{\rm H_2}/5{\times}10^{14}\,{\rm cm}^{-2}$, $b_5 = b/10^5\,{\rm cm\ s}^{-1}$, $a = 1.1$, and $b = 9.12\,{\rm km\ s}^{-1}(T/10^4\,{\rm K})^{1/2}$, the latter representing the velocity spread for the thermal motion of $H_2$ (Ahn & Shapiro, 2007; Wolcott-Green & Haiman, 2011). The $H_2$ column density is estimated on-the-fly in our simulations via $N_{\rm H_2} \approx n_{\rm H_2} L_{\rm char}$, where $n_{\rm H_2}$ is the molecular

hydrogen number density and $L_{\rm char}$ is a local characteristic scale length. To reduce computational overhead, we take $L_{\rm char} \approx L_{\rm J}$ (Bromm & Loeb, 2003a), employing the local Jeans length $L_{\rm J} = \sqrt{15 k_B T / 4\pi\rho G m_H}$. This approach compares favorably to more computationally expensive estimates, such as 'six-ray' or Sobolev approximations. See the discussions in Safranek-Shrader et al. (2012) and Wolcott-Green & Haiman (2011) for detailed comparisons between methods.

The shape of the assumed spectrum plays an important role in determining the photo-detachment/dissociation rate for $H^-, {H_2}^+$. The values $\alpha = 1.71$ and $\beta = 0.97$ in $k_{\rm de}$ and $k_{\rm di}$ (Equation 2.18,2.19) for Pop III SF are taken from Agarwal & Khochfar (2015), who use stellar population models (STARBURST99, Leitherer et al., 1999; Schaerer, 2002) to generate realistic stellar spectra in order to determine the normalization, rather than blackbody curves at $10^4 - 10^5$K. Agarwal & Khochfar (2015) conclude that the $\alpha$ and $\beta$ parameters for Pop II SF vary depending on the star formation history, metallicity and age of the stellar population. For this work, we adopt the same $\alpha$ and $\beta$ for Pop II as Pop III for simplicity, closely representing a Pop II starburst with an age of $\sim 20$ Myr and $Z = 0.05\ Z_\odot$. In future work, we will consider explicit Pop II star formation, at which time we will be able to determine these values in a more self-consistent manner.

#### 2.2.3.2 Pop II Contribution to LW Flux

Since we are not explicitly forming Pop II stars in our simulation, we must approximate their contribution to the total SFRD and ultimately the global LW flux. This is accomplished by combining observed values at $z = 6 - 10$ with theoretical

estimates for $z > 10$ to obtain an approximate functional form for the global Pop II SFRD. We find that a simple exponential function of the form

$$\dot{\rho}_{*,\mathrm{PopII}} = Ae^{-B(1+z)^2}, \tag{2.21}$$

with $A = 0.15$ and $B = 0.024$, provides a good fit to both observations and theory at $6 \leq z \leq 25$.

In Section 2.3.1.1, in conjunction with our SFRD results, we present estimates of the high-$z$ SFRD, derived from the (dust-corrected) UV luminosity function (UVLF), obtained by integrating the UVLF down to a given limit (Finkelstein, 2016). Specifically, observations currently reach down to a limit of $M_{\mathrm{UV}} = -17$ (green circles). Integrating of the UVLF down to $M_{\mathrm{UV}} = -13$ represents an effort to account for systems which are below the observations threshold (gray diamonds). We also consider a theoretical estimate (dashed cyan line) from hydrodynamical simulations of the Pop II SFRD out to $z \sim 25$, found in Maio et al. (2010). It is evident that our ad-hoc estimation above agrees well with both observations and theory (see Section 2.3.1.1 for further discussion). It should be noted that the Pop II contribution is calculated using Equation 2.17 with $\eta_{\mathrm{LW}} \approx 2 \times 10^3$ to reflect the Salpeter IMF of Pop II stars.

#### 2.2.3.3 UV Background

The final component to terminating Pop III star formation is the UV ionizing background (UVB) produced by Pop II stars. This background radiation ionizes gas in both the host and adjacent haloes, effectively suppressing star formation in metal

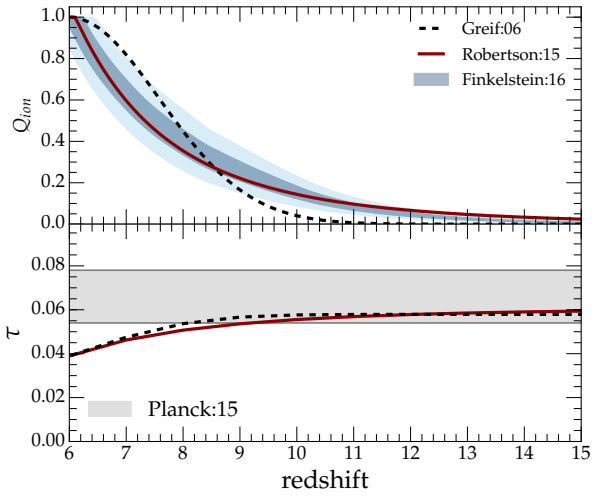


Figure 2.5: *Top:* Ionization volume fraction $Q_{\rm ion}$, based on observational constraints (Finkelstein, 2016), indicated by the dark/light blue shaded region (68%/95% confidence), and Robertson et al. (2015) shown as dark red solid line. Also shown is the model employed in this work (Greif & Bromm, 2006), where the ionization fraction is represented by a Gaussian at $z \geq 6$. *Bottom:* Thomson optical depth, $\tau$, calculated for each of the estimates presented in the top panel, along with the Planck 2015 constraints (gray shaded region). Here we demonstrate that none of the ionization histories discussed can be ruled out.

free systems by limiting their ability to effectively cool. Due to the short mean free path of ionizing radiation, the UVB cannot be considered homogeneous, as was the case with the LW background. Since we are not explicitly forming Pop II stars, we adopt a statistical approach to model the patchy nature of the UVB, similar to that employed in Greif & Bromm (2006). In our Pop II proxy model (P2P), the probability that a star forming region lies in a region which has been previously ionized can be calculated by

$$p_{\rm ion} = Q_{\rm ion}[1 + \xi_{\rm hh}(z)], \tag{2.22}$$

where $Q_{\rm ion}$ is the current cosmic ionization fraction, and the halo correlation function, $\xi_{\rm hh}$, can be interpreted as an excess probability based on the cosmology of our specific simulation volume, see Greif & Bromm (2006) and references therein for the calculation of $\xi_{\rm hh}$. For the halo mass range encountered in our simulations, $10^6 - 10^{10}\ M_\odot$, we find $\xi_{\rm hh} \sim 10^{-2}$, effectively rendering $p_{\rm ion} \approx Q_{\rm ion}$. We model $Q_{\rm ion}$, following Greif & Bromm (2006), with a Gaussian of the form

$$Q_{\rm ion} = \exp(-(z - 6)^2/w). \tag{2.23}$$

Here $w = 5$ provides a reasonable representation of the observations (note $Q_{\rm ion} = 1.0$ at $z \leq 6$). Each time a gas particle qualifies for Pop III star formation, a pseudo random number, $\mathcal{R}_{\rm ion}$, between [0-1] is drawn. If $\mathcal{R}_{\rm ion} \leq p_{\rm ion}(z)$, the region is considered to be ionized and a Pop III star is not allowed to form. We do not explicitly include the ability of dense gas to self shield in our UVB treatment. However, this phenomenon is implicit in the estimates of $Q_{\rm ion}$ upon which our model is based.

The top panel of Figure 2.5 shows several observational estimations for $Q_{\rm ion}$ from Robertson et al. (2015) and Finkelstein (2016), which are in good agreement with each other. Our assumed ionization history, generated by Equation 2.23, is not intended to be an exact fit to the observational estimates, but rather an approximation which gives a reasonable representation of the data which indicates a late reionization scenario. We note that estimates for the total number of ionizing sources and dark matter halo escape fractions are subject to large uncertainties, rendering determinations of the detailed reionization history of the Universe highly uncertain as well. While the true nature of $Q_{\rm ion}$ is thus uncertain, our choice of a late reionization scenario allows us to provide an upper limit for the amount of metals which can be formed via Pop III star formation.

## 2.3 Results

We again would like to point out to the reader, that we are only considering metal enrichment from Pop III star formation. Therefore, in the absence of Pop II chemical feedback, what we present here is an idealized numerical experiment, providing an upper limit to the ability of Pop III to enrich the early Universe.

### 2.3.1 Global Properties

#### 2.3.1.1 Star Formation Rate Density

One of the principal observational constraints that can be placed on Pop III star formation comes from frontier galaxies observations at $z \gtrsim 6$ in the form of the total star formation rate density. While not directly probing Pop III star formation,

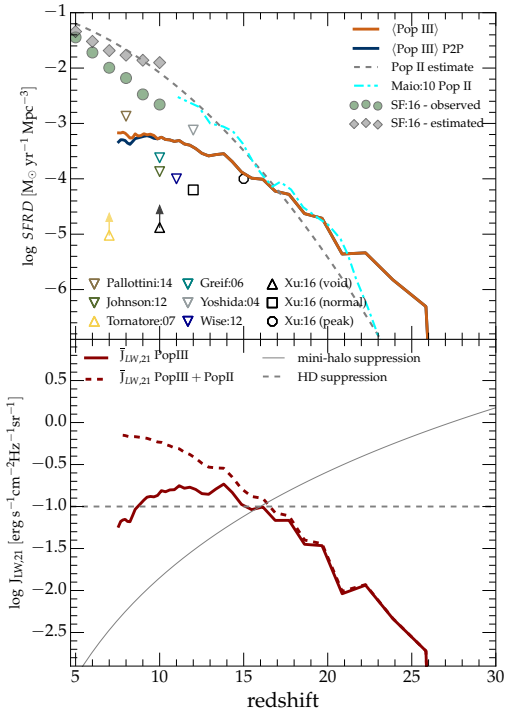


Figure 2.6: *Top:* Mean Pop III SFRD from our simulations with P2P on and off (solid blue/orange lines). We also show observations for the Pop II SFRD, derived from the reference UVLF (gray diamonds, green circles) discussed in Finkelstein (2016), which combines frontier observations $z \geq 5$ from published studies, as well as the simulation prediction by Maio et al. (2010) (cyan dashed-dotted line). The difference between the estimated total (gray diamonds) and observed (green circles) points is that the former are determined by integrating the UVLF down to a limit of $M_{\rm UV} = -13$ to account for systems which are below the current observational threshold. The gray-dashed line represents our model Pop II SFRD from Equation 2.21. We also include comparisons to previous numerical studies which are estimates for the peak of each Pop III SFRD and the redshift at which it occurs. *Bottom:* Lyman-Werner background flux calculated from Equation 2.17 for Pop III only (solid red line) and Pop III + Pop II P2P (dashed red line). The solid gray line represents the estimated threshold beyond which $H_2$ formation will be suppressed in minihaloes, and the dashed gray line indicates the flux level required to suppress HD.

observations of the Pop II dominated deep-field galaxies (e.g. Finkelstein et al., 2015; Bouwens et al., 2015, 2016; Bowler et al., 2014; Schmidt et al., 2014; McLure et al., 2009, 2013; Oesch et al., 2013, 2014) set an upper limit for the combined total of both Pop II and Pop III. In the top panel of Figure 2.6, we present the mean SFRD calculated from our simulation volumes both with (blue) and without (orange) the P2P model enabled, along with estimates of the observed SFRD calculated from a compilation of studies presented in Finkelstein (2016). Here we see that both our simulation runs peak and saturate at $\sim 10^{-3}$ $M_\odot$ $yr^{-1}$ $Mpc^{-3}$ which is roughly an order of magnitude less than the estimated total SFRD at that epoch (gray diamonds).

We compare our results for the Pop III SFRD to previous studies which have employed a variety of numerical techniques, such as AMR (Pallottini et al., 2014; Johnson et al., 2013), SPH (Yoshida et al., 2004; Tornatore et al., 2007; Johnson et al., 2013), and semi-analytic (Greif & Bromm, 2006). To make a direct comparison to the results found in different studies we examine the peak of the Pop III SFRD and the corresponding redshift (see triangles in Figure 2.6). While the peak redshifts vary, our results broadly agree with those found in Pallottini et al. (2014); Johnson et al. (2013); Wise et al. (2012); Greif et al. (2007); Yoshida et al. (2004). However, our results are more than an order of magnitude higher than those found in Xu et al. (2016a) and Tornatore et al. (2007). In the case of the Tornatore et al. (2007) results, this discrepancy is likely due to the much lower halo mass resolution ($M_h \sim 10^8\ M_\odot$) utilized in their study which did not allow for Pop III star forming regions to be fully resolved. The Xu et al. (2016a) work utilized highly resolved AMR simulations to look at star formation in void, normal, and peak density regions. Our results are

only significantly different when compared to the SFRD in the void regions.

Due to the P2P model, the blue line in Figure 2.6 begins to deviate to lower values at $z \sim 10$. This behavior is expected as the P2P model is directly coupled to the ionization fraction utilized which begins to ramp up at the same redshift. From Figure 2.5 and Equation 2.23 it can be seen that $Q_{\rm ion} \approx 0.64$ at $z$ =7.5. While resulting in only a small variation at the terminal redshift reached in our simulation, the rapid increase of the ionization fraction leads to a mostly ionized Universe by $z$=6. The increased ionizing flux is directly responsible for terminating Pop III star formation as it heats the gas which cannot self-shield in low density, low metallicity haloes. Due to computational constraints, we were not able to reach $z$=6 with this suite of simulations. However, it is plausible to predict that our P2P-enabled simulation SFRD would continue to decline until being terminated at $z \approx$6. We have completed lower resolutions runs to confirm that our P2P model does have the predicted impact on the global Pop III SFRD.

We note that all further analysis will be conducted on the simulation run with P2P enabled. It is also important when examining these results to recall that we are only considering metal enrichment from Pop III star formation.

#### 2.3.1.2 Metallicity

The primary legacy left by Pop III star formation, and the main focus of this study, are the metals which are imparted to the ISM/IGM by Pop III SNe. In Figure 2.7 we present a visualization of our simulation volume at $z$=15 (left) and $z$=7.5 (right) to illustrate the patchy nature of Pop III enrichment. In Figure 2.8,

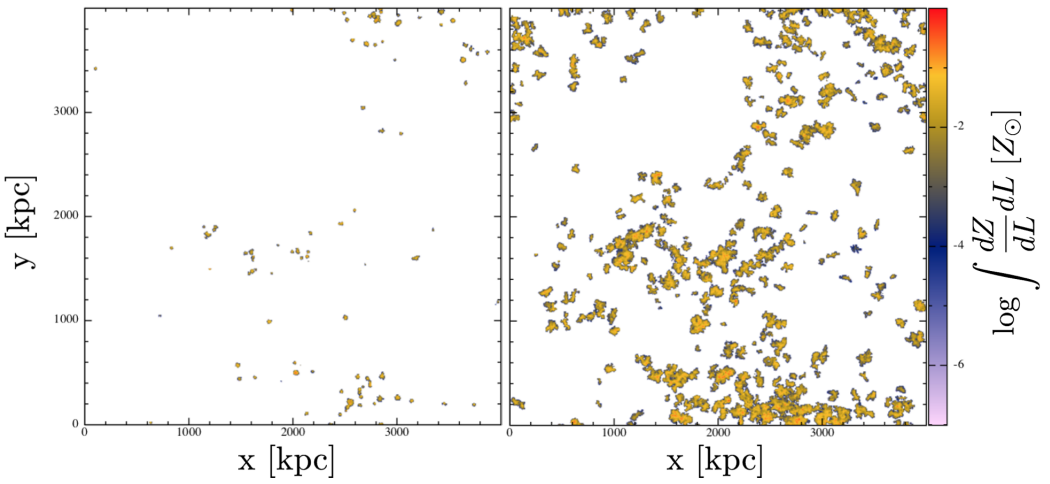


Figure 2.7: Metallicity projection plot for $z$=15 (left) and $z$=7.5 (right) for our N512L4_P2P run. The color bar represents the integrated metallicity along the line of sight through the z-axis of the computational volume. Visualizations generated using SPLASH (Price, 2007).

the solid blue line represents the evolution of the mean metallicity of all the gas particles in our simulation volume. As the total amount of baryonic matter in our simulation box is finite, the mean metallicity will continue to rise, as long as Pop III star formation continues. Furthermore, once Pop III star formation is terminated the mean metallicity will remain constant. Interestingly, this value is only approaching the critical metallicity required for the Pop III to Pop II transition, $Z_{\rm crit} = 10^{-4}\ Z_{\odot}$, by $z \sim 7$ (dashed gray line).

Simple extrapolation of our metallicity value at $z \geq 7.5$ leads to an average metallicity which is only slightly greater than $Z_{\rm crit}$ by $z = 6$. This result is in contrast to the assumptions made by previous generation large cosmological volume simulations (e.g. Jaacks et al., 2012a,b) in which Pop III stars are not explicitly

formed and a metallicity floor for all gas particles is implemented at $z > 15$ (typically the critical value of $Z \approx 10^{-4}\ Z_{\odot}$). The consequence of this approach is that Pop II stars could be allowed to form in regions which otherwise would be devoid of metals, thus potentially overproducing Pop II stars in $z \geq 6$ galaxies. We intend to further explore this conjecture in future work.

The fact that our mean metallicity does not exceed $Z_{\rm crit}$ prior to reionization suggests that Pop III star formation is not a globally self-terminating process, as previously argued by Yoshida et al. (2004). The results of the Yoshida et al. (2004) study is indicated by the gray dashed-dotted line in Figure 2.8, substantially higher than our enrichment history. The large difference is a direct consequence of the Pop III IMF assumed in that earlier work, which was chosen to be very top-heavy, considering only stars with $M_* = 100 - 300\ M_{\odot}$. The impact of this is that each SN event was considered to be a PISN, which has a much higher mass yield than other SN types (see Table 2.3). Therefore, the Yoshida et al. (2004) results can be viewed as an upper limit to the mean metal enrichment.

It should be noted that, in the context of this work, we consider the concept of global self-termination to refer to the ability of Pop III star formation to suppress future Pop III star formation throughout the simulation volume rather than only in a given host halo. For bound haloes we find that metal enrichment rapidly increases to above $Z_{\rm crit}$ shortly after Pop III star formation begins, as indicated by the solid cyan line in Figure 2.8. We find that within bound haloes there is a plateau metallicity value of $Z/Z_{\odot} \approx 10^{-3}$, consistent with previous AMR simulations from Wise et al. (2012).

The currently highest-redshift observation to constrain our modeling comes from Simcoe et al. (2012) in the form of a damped Lyman alpha (DLA) absorption system at $z \simeq 7$. This system has an estimated metallicity of $Z = 10^{-4}\ Z_{\odot}$, if residing in a bound proto-galactic halo, or $Z = 10^{-3}\ Z_{\odot}$, if part of the diffuse, unbound IGM. The mean metallicity from enriched, bound systems found in our simulation volume is nearly one dex higher than the observed estimate (cyan circle). However, the observed point does fall within our 95% confidence range, indicating that, while very rare, such systems do exist in our computational box. In Sec 2.3.3, we sample such a region to create a mock observation. Note that we define "bound" to be gas which resides within the virial radius of a dark matter halo which is consistent with Simcoe et al. (2012).

The Rafelski et al. (2014) observations at $z \simeq 4.7$ (purple range) contain systems with a range of metallicities ($10^{-1.4} \lesssim Z/Z_{\odot} \lesssim 10^{-2.8}$); all of which are higher than our mean value for bound systems. This is expected as these observations most likely contain enrichment from both Pop III and Pop II star formation. This provides a strong upper bound for Pop III only enrichment.

#### 2.3.1.3 Volume Filling Fraction

In Figure 2.9 we explore the redshift evolution of the fraction of our simulation volume which is enriched by Pop III star formation to at least the indicated values (i.e. volume filling fraction). At lower redshifts, $z \leq 20$, gas which is enriched to $Z > 10^{-2} - 10^{-3}\ Z_{\odot}$ can be considered to reside in star forming regions, while gas enriched to $Z < 10^{-3}\ Z_{\odot}$ is associated with the IGM. While not identi-

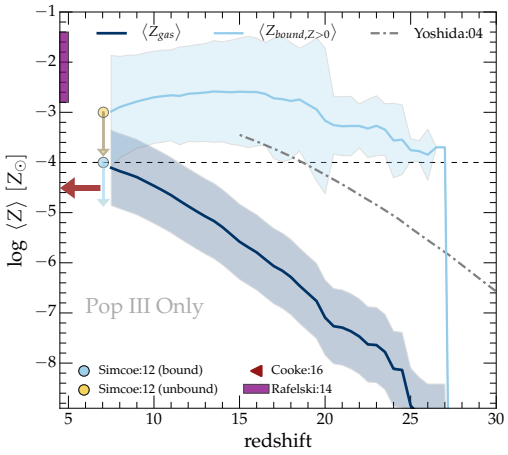


Figure 2.8: Redshift evolution of the mean metallicity for all gas particles in our simulation volume (solid blue line), and for haloes which have $Z > 0$ (cyan). The horizontal dashed gray line represents the critical metallicity ($Z_{\rm crit} = 10^{-4} Z_\odot$) for the Pop III to Pop II transition. We also reproduce the predicted metallicity evolution from Yoshida et al. (2004), where *all* Pop III stars were considered to end their lives as PISNe, thus imparting a maximum amount of metals back into their environment. Observations of high redshift DLA systems are indicated by the yellow/blue circles ($z = 7.04$; Simcoe et al., 2012), and the purple range ($z > 4.7$; Rafelski et al., 2014). The red arrow points to a lower redshift observation by Cooke et al. (2016). The tan circle is the estimate based on the assumption of an unbound medium, whereas the yellow point is for a bound structure. Both are considered upper limits.

cal, the blue line representing gas with $Z \geq 10^{-6}$ and the orange line representing gas enriched to $Z \geq 10^{-4}$ are nearly indistinguishable over the entire simulation run. Due to our mass and spatial resolutions we are unable to sufficiently resolve metallicities of $Z < 10^{-6}$. However, our results suggest that even minimal Pop III star formation activity quickly enriches regions to $Z \geq 10^{-6}$ $Z_{\odot}$. In contrast, the appearance of regions which are enriched to $Z \geq 10^{-2}$ $Z_{\odot}$ is delayed by $\sim$ 70 Myr from the start of our Pop III star formation (i.e. $z = 27 - 20$) due to the time required to build up metals in any one given star forming region. Additionally, an upper limit to the Pop III metallicity manifests itself as there is a large ($\sim$ 3 dex) drop between $Z \geq 10^{-2}$ $Z_{\odot}$ and $Z \geq 10^{-1}$ $Z_{\odot}$, with no gas enriched to $Z_{\odot}$.

The fraction of our volume which is enriched to $Z \geq 10^{-6}$ shows an exponential growth trend ($\log \mathcal{F}_V \propto z^{-0.20}$) from a value of $\sim 10^{-6}$ at $z$=27 to $\sim 10^{-2.7}$ at $z$=7.5. The approximately equivalent growth rate over all metallicities shown in Figure 2.9 can be directly attributed to the growth in the Pop III SFRD which demonstrates a similar growth trend (SFRD$\propto z^{-0.20}$) over the majority of the simulation run. Any deviations from this behavior in the volume fraction are likely the result of merger events.

Comparison of our Pop III volume filling fraction to previous numerical studies is difficult as the majority do not differentiate between Pop II and Pop III enrichment (e.g. Oppenheimer & Davé, 2006; Tornatore et al., 2007; Johnson et al., 2013; Pallottini et al., 2014) . However, just as with the observed SFRD (see Sec. 2.3.1.1), past numerical studies can be utilized to provide upper limits for the metal enrichment. Specifically, the purple dash-dotted line in Figure 2.9 represents

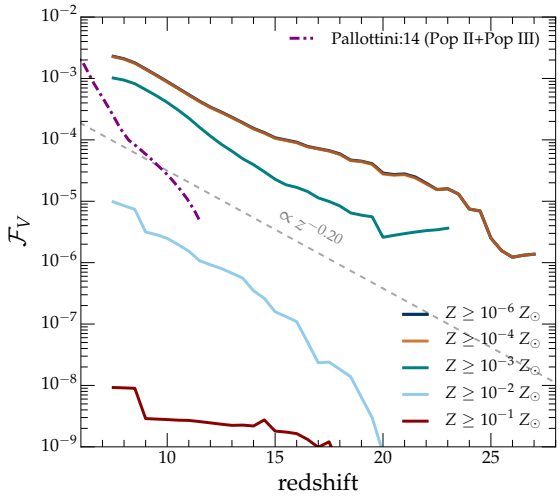


Figure 2.9: Volume filing fraction ($\mathcal{F}_V$) of our simulation box which is enriched to at least the values indicated. From top to bottom, the lines represent $\log Z/Z_\odot > -6, -4, -3, -2, -1$ (blue, orange, teal, cyan, red). The dark blue and orange lines essentially overlap with only minor variation, indicating that our enrichment floor of an individual region is $\sim 10^{-4} - 10^{-5}\ Z_\odot$. The gray dashed line indicates a growth rate of $\log \mathcal{F}_V \propto z^{-0.20}$. It should be noted that the gray line is not an exact fit to the data. The purple dash-dotted line represents an estimate for $\log Z/Z_\odot > -2$ from Pallottini et al. (2014), which includes metals from both Pop II and Pop III star formation.

results from Pallottini et al. (2014), who utilized AMR simulations to study early cosmic enrichment. It is clear that our result, for the same enrichment value of $Z \geq 10^{-2}\ Z_{\odot}$ (solid cyan line), is considerably lower, which is expected as we here include only Pop III enrichment.

### 2.3.2 Virialized Structures

By grouping gas particles associated with their host dark matter haloes, we can extract information regarding the evolution of metals within bound, virialized structures. In the top panel of Figure 2.10 we present the relation between dark matter halo mass and mean metallicity for three different redshifts ($z$=20, 15, 7.5). It is clearly seen that a strong relation between the mass of the halo and it's mean metallicity is established by $z \simeq 7.5$. This trend is expected as higher mass haloes experience higher star formation rates, and therefore more metal enrichment. Specifically, those haloes will continue forming Pop III stars through accretion of pristine gas, which is processed at a higher efficiency. It has indeed been shown by Greif et al. (2008) that higher mass haloes host Pop III star formation at increased efficiency due to their deeper potential wells, leading to a larger number of free electrons. The latter then catalyze enhanced production of $H_2$, followed by increased HD formation, resulting in more effective cooling. Thus, those haloes exhibit higher metallicities, as shown in Figure 2.10.

In our P3L model, star formation is only allowed for gas with $Z < Z_{\rm crit}$. However, it is clear from Figure 2.10 that bound systems are able to enrich well beyond the critical value. This can be attributed to the constant accretion of primordial

metal free gas onto the halo which, once cooled, can fuel new star formation. In conjunction, haloes also acquire metals through mergers with systems which have previously been enriched.

An interesting feature found when examining the halo mass to mean-metallicity relation is the heavy element "Pop III plateau" of $\langle Z \rangle \sim 10^{-2}\ Z_{\odot}$, beyond which there are only a few haloes at $z$=15 and none at $z$=7.5. This is supported by the results found in Section 2.3.1.3, where only a tiny fraction ($< 10^{-5}$) of any region in our simulation volume was enriched to $Z \geq 10^{-2}\ Z_{\odot}$ by $z$=7.5. These trends suggest that any bound halo with gas estimated to have $\langle Z \rangle > 10^{-2}\ Z_{\odot}$ would have to contain metals generated from Pop II star formation. Our "plateau" value of $\langle Z \rangle \sim 10^{-2}\ Z_{\odot}$ is very similar to that found in Wise et al. (2012), where $\log \langle Z \rangle = -2.1\ Z_{\odot}$, and reflects a natural balance point between metal production and dilution. It is also noteworthy that a metallicity floor emerges as we have zero bounds systems that are enriched to $Z < 10^{-7}\ Z_{\odot}$, although this may in part reflect our limited mass resolution (see the discussion in Jeon et al. (2017)).

A second interesting feature in Figure 2.10 is the "gap" at $M_h \approx 10^{7.5} M_{\odot}$, which appears in the top panel and in the histogram at the bottom of the same figure, resulting in a bi-modal distribution at $z$=7.5 (dark blue). It should be noted that there is no dearth of haloes at this mass, as can be seen in the total halo mass distribution (dark solid blue bar below $\log Z/Z_{\odot} = -7$). Rather, there are few haloes at this mass which are enriched. Therefore, it is more appropriate to characterize this deficit as a "metallicity gap".

The majority of the population with $M_h \lesssim 10^{7.5} M_{\odot}$ at $z$=7.5 is enriched

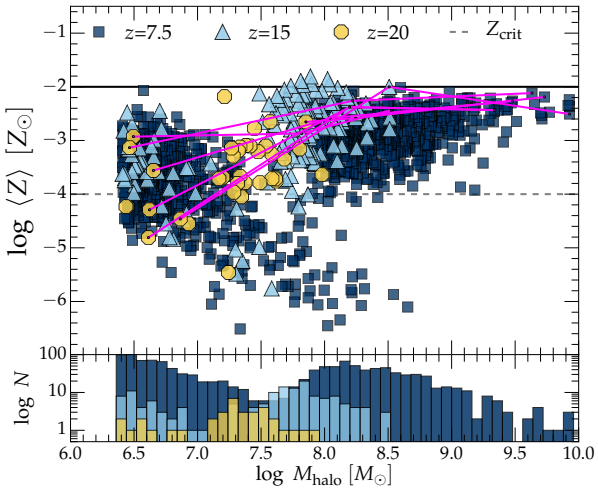


Figure 2.10: *Top:* Average halo metallicity as a function of dark mater halo mass for redshifts $z = 20, 15, 7.5$ (yellow octagons, cyan triangles, blue squares). We also display the evolutionary paths of select individual systems, indicated by the solid magenta lines. *Bottom:* Histogram of the enriched dark matter halo mass distribution for each redshift above.

by external processes, defined in this work to be any process other than in-situ star formation (i.e. accretion of enriched gas, star formation in nearby haloes or mergers). These external enrichment haloes make up $\sim 45\%$ of the entire enriched population at $z$=7.5 (blue squares with red border). At higher redshift, the $M_h \lesssim 10^{7.5} M_\odot$ haloes are a combination of 'in-situ' and externally enriched systems. Due to hierarchical structure formation and their proximity to star forming haloes, they quickly merge with the more massive systems, which can be clearly discerned in the evolutionary tracks in Figure 2.10, indicated by the magenta lines connecting progenitors to descendants. A similar effect was found in Jeon et al. (2017), who simulated the assembly of fossil dwarf galaxies in the Local Group.

### 2.3.3 Diffuse IGM

DLA systems are valuable probes of the CGM/IGM temperature, density and metal structure, as photons from bright background sources, such as AGN and GRB afterglows, are absorbed while propagating through these systems. Given that the temperature, density and metal content are intrinsic properties of the gas in our simulations, it is possible to generate mock observations to probe them. To accomplish this, we consider the radiative transfer equation, simplified for a purely absorptive to

$$I_\nu = I(0) e^{-\tau_\nu}, \tag{2.24}$$

valid for a static medium. Here, $I_\nu$ is the specific intensity, $I(0)$ the emission from the background source, and $\tau_\nu$ the optical depth along the line of sight (LOS) between the system and observer. For simplicity, we adopt a simple power-law, $f_\nu \propto \nu^{-1}$,

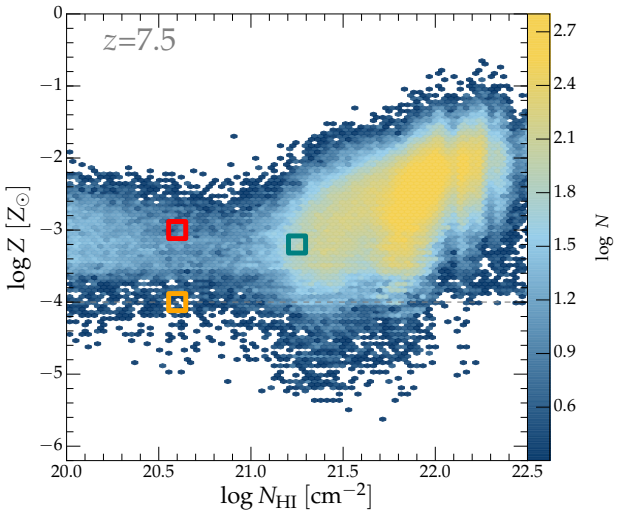


Figure 2.11: Gas particle metallicity as a function of each particles estimated column density at $z$ =7.5. The color scale indicates the number density of the gas particles in this phase space. It should also be noted that, due to the large particle count, only a representative subset (1/10) of particles are plotted here. We have verified that this sampling does not impact the underlying relation. The orange, red and teal squares correspond to regions which were sampled to create mock absorption-line spectra (see Figure 2.13).

representing a GRB afterglow as our background source spectrum, such that there are no intrinsic spectral features imprinted by the local environment. To normalize the afterglow emission, we adopt the source parameters employed in Wang et al. (2012). Specifically, the GRB is assumed to originate in a minihalo at $z \simeq 16.5$, observed at the reverse shock crossing time (see figure 10 in Wang et al., 2012).

The usual procedure for obtaining the optical depth from a simulation is to create a column along the LOS, and integrate $d\tau_\nu = \sigma_\nu n_X dl$. Here $\sigma_\nu$ is the frequency dependent cross-section, $n_X$ is the number density of a given species, and $dl$ is a differential length along the LOS. Establishing an appropriate column is somewhat arbitrary in the context of a cosmological volume simulation. We therefore employ an idealized local prescription, where we simplify our optical depth calculation to

$$\tau_\nu = \sigma_\nu n_X L_{\rm char} = \sigma_\nu N_X \, . \tag{2.25}$$

Here, we take $L_{\rm char}$ to be the local Jeans length of the gas particle (see Sec 2.2.3.1 for additional discussion regarding $L_{\rm char}$), and $N_X$ is the column density of the absorbing species. This prescription allows us to create synthetic absorption spectra by simply sampling the column density and metallicity from Figure 2.11.

Evidently, our approach is only valid if the cosmological redshift across our simulation box is negligible, $\Delta\lambda/\lambda_0 = L_{\rm phys} H(z)/c \ll 1$. At $z$=7.5, we find $\Delta\lambda/\lambda_0 \approx 1.5 \times 10^{-3}$. Therefore, even if two systems along a line of sight were separated by the entire box length, the $\Delta\lambda$ is so small that existing high-resolution spectrographs would be unable to resolve the line shift. Further, our method for estimating column density, using locally evaluated quantities, is clearly very approximate, and

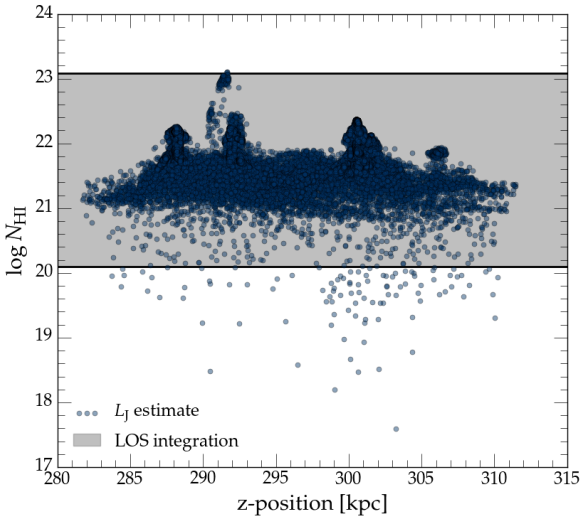


Figure 2.12: Comparison between column densities calculated for a single halo extracted from our simulation volume using LOS integration (gray horizontal span denotes the minimum and maximum range) and the approximation presented in Section 2.3.3, which utilizes the Jeans length for a given SPH particle (blue circles). The $z$ coordinate marks positions of individual SPH particles along the LOS.

Table 2.5: Elements considered in creating the absorption spectra in Figure 2.13, along with their metal abundance ($X_x = m_x/m_*$), rest-frame wavelength and oscillator strength. Metal yields were take from Heger & Woosley (2010) for the zero metallicity Type II case, and Heger & Woosley (2002) for the PISN case. Atomic transition data was obtained from Morton (2003).

| Element | $X_{x,\mathrm{TypeII}}$ $10^{-2}$ | $X_{x,\mathrm{PISNe}}$ $10^{-2}$ | State | $\lambda_{\mathrm{rest}}$ [Å] | $f_{\mathrm{osc}}$ |
|---|---|---|---|---|---|
| C | 1.08 | 4.92 | $C_{ii}$ | 1334.5 | 0.1278 |
| | | | $C_{iv}$ | 1548.2 | 0.1908 |
| | | | $C_{iv}$ | 1550.8 | 0.0952 |
| O | 8.80 | 3.51 | $O_{i}$ | 1302.2 | 0.0489 |
| Mg | 0.52 | 2.01 | $Mg_{ii}$ | 2796.4 | 0.6155 |
| Si | 0.750 | 0.225 | $Si_{,ii}$ | 1260.4 | 1.190 |
| | | | $Si_{ii}$ | 1304.4 | 0.094 |
| | | | $Si_{iv}$ | 1393.8 | 0.514 |
| | | | $Si_{iv}$ | 1402.8 | 0.2553 |
| Fe | 1.10 | 3.08 | $Fe_{ii}$ | 1608.5 | 0.058 |
| | | | $Fe_{ii}$ | 2344.2 | 0.114 |
| | | | $Fe_{ii}$ | 2382.8 | 0.300 |
| | | | $Fe_{ii}$ | 2586.7 | 0.069 |
| | | | $Fe_{ii}$ | 2600.2 | 0.239 |

therefore should not be considered a replacement for precise LOS determinations. In Figure 2.12, we present the results of a test in which we extract a single halo from our simulation volume and compare the column densities calculated using direct LOS integration, intersecting the system at different impact parameters, with the local, particle-by-particle estimates adopted in this work. This test confirms that our idealized method provides reasonable agreement over the range of densities studied here.

The final ingredient required to calculate the optical depth is the frequency dependent cross-section,

(2.26)

where $f_{\rm osc}$ is the oscillator strength, $H(u, x)$ the Voigt function, and $\Delta\nu_D$ the Doppler width. We refer the reader to Wang et al. (2012), and references therein, for details of the radiative transfer calculation, and the parameter choices in Equation 2.26. Data for the atomic transitions are taken from Morton (2003).

The abundance for each species is obtained by convolving estimates for the yields for zero-metallicity Type II and PISN events (Heger & Woosley, 2002, 2010), with the IMF employed in our simulations. By integrating our selected IMF (Equations 2.3 and 2.4) over the appropriate mass ranges for Type II and PISNe (see Section 2.2.1.3), we determine the mass in metals contributed by each event, which we then use to calculate a weighted mean of the metal yields for both event types from Table 2.5. The weights for each event are given by

$$w_{\rm TypeII} = \frac{Y_{\rm TypeII} m_{*,\rm TypeII}}{Y_{\rm TypeII} m_{*,\rm TypeII} + Y_{\rm PISN} m_{*,\rm PISN}} \approx 0.13, \tag{2.27}$$

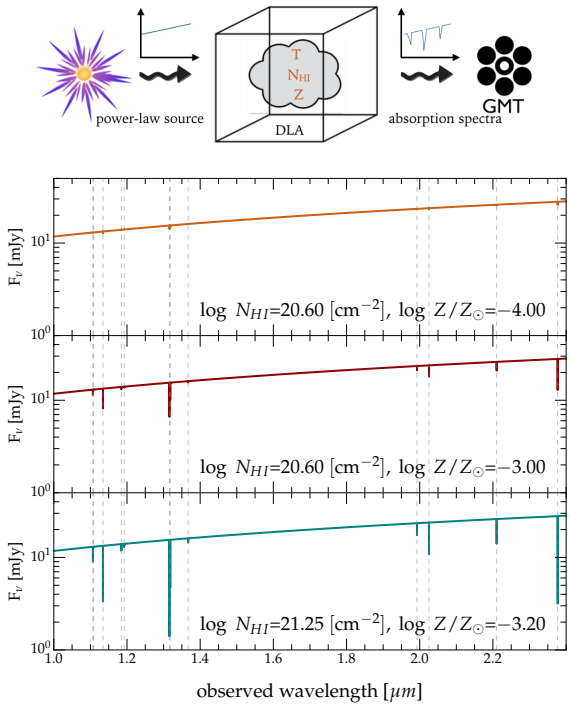


Figure 2.13: *Top:* Illustration of our scenario with a generic GRB power-law spectrum passing through an IGM absorption system with a unique set of physical properties $(T, N_{\rm HI}, Z)$, before reaching the observer. *Bottom:* A sample of three synthetic spectra, generated from our simulation volume. The top two are representative of the Simcoe et al. (2012) estimates, whereas the bottom is a randomly selected region from the parameter space in Figure 2.11. Temperatures of the three regions are very similar with $T \approx 10^{3.8}$ K, corresponding to a Doppler width of $b \approx 10\,{\rm km\,s^{-1}}$.

Table 2.6: Observed frame equivalent widths ($W$) for select ions calculated from the spectra presented in Figure 2.13. The subscripts 1, 2, 3 correspond to the spectra top to bottom. The final column $W_{\rm obs}$ contains the values presented in Simcoe et al. (2012) for their $z$=7.04 DLA (upper limits). Note the observed equivalent width have been adjusted to the observed frame rather than rest-frame which was presented in the original work. Direct qualitative comparisons should be made between $W_1$ and $W_{\rm obs}$.

| Ion | $\lambda_{\rm rest}$ [Å] | $W_1$ [Å] | $W_2$ [Å] | $W_3$ [Å] | $W_{\rm obs}$ [Å] |
|---|---|---|---|---|---|
| $O_i$ | 1302.2 | 0.009 | 0.084 | 0.218 | $\leq$ 0.354 |
| $C_{ii}$ | 1334.5 | 0.033 | 0.284 | 0.616 | $\leq$ 0.137 |
| $Si_{ii}$ | 1260.4 | 0.008 | 0.077 | 0.200 | $\leq$ 0.072 |
| $Fe_{ii}$ | 2586.7 | 0.009 | 0.091 | 0.245 | $\leq$ 0.306 |
| $C_{iv}$ | 1548.2 | 0.065 | 0.511 | 0.965 | $\leq$ 0.579 |
| $Mg_{ii}$ | 2796.4 | 0.141 | 1.051 | 1.889 | $\leq$ 0.555 |
| $Fe_{ii}$ | 2600.2 | 0.032 | 0.248 | 0.731 | $\leq$ 0.113 |

$$w_{\rm PISN} = \frac{Y_{\rm PISN} m_{*,\rm PISN}}{Y_{\rm TypeII} m_{*,\rm TypeII} + Y_{\rm PISN} m_{*,\rm PISN}} \approx 0.87. \tag{2.28}$$

The resulting abundance pattern is thus directly coupled to the assumed IMF. Our final column density for each absorber then is

$$N_X = N_{\rm HI} Z \left( w_{\rm TypeII} X_{x,\rm TypeII} \mathcal{R}_x + w_{\rm PISN} X_{x,\rm PISN} \mathcal{R}_x \right) . \tag{2.29}$$

The values for $Y_x$ and $X_x$ can be found in Table 2.3 and 2.5, respectively, and $\mathcal{R}_x$ is the mass ratio of the absorber and hydrogen ($m_x/m_{\rm H}$).

In Figure 2.13, we present select synthetic spectra, resulting from feature-less GRB afterglow emission which we pass through our simulated systems with properties similar to observed DLAs ($N_{\rm HI} \geq 10^{20}$ cm$^{-2}$). The first two spectra are take from regions which are similar in density and metallicity to the Simcoe

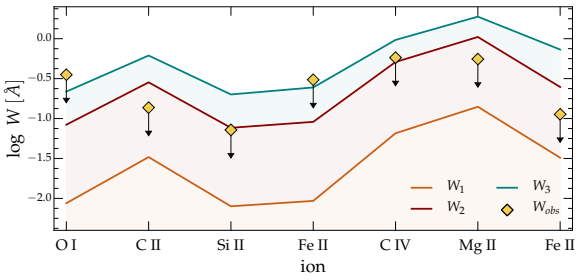


Figure 2.14: Observer-frame equivalent widths, calculated from the synthetic spectra presented in Figure 2.13 and Table 2.6, compared to the $1\sigma$ upper limits derived from observations at $z$=7.04 from Simcoe et al. (2012) (yellow diamonds).

et al. (2012) DLA estimates, and the final spectrum is randomly chosen from our parameter space in Figure 2.11. While we make direct comparisons of our simulated equivalent widths to those found in observations, we caution the reader that our limited resolution and idealized nature of our methodology allow for only a qualitative comparison.

In Table 2.6, we provide estimates for observer-frame equivalent widths,

$$W = (1+z)\int [1 - e^{-\tau(\lambda)}]\, d\lambda\,, \tag{2.30}$$

for select ions calculated from the spectra presented in Figure 2.13. The subscripts 1, 2, 3 correspond to the spectra from top to bottom. The final column, $W_{\rm obs}$, contains the values presented in Simcoe et al. (2012) for their $z$=7.04 DLA. We note that the observed values were shifted to the observed frame for direct comparison to $W_{\rm obs}$. We find that our equivalent widths $W_1$ and $W_2$, which have similar column density ($\log N_{\rm HI} = 20.6{\rm cm}^{-2}$) and metallicity ($\log Z/Z_\odot = -3, -4$) to the systems in Simcoe et al. (2012), are in qualitative agreement with their published results. This

agreement suggests that a Pop III only enriched region is a plausible explanation for the Simcoe et al. (2012) observation.

We caution that due to the inherent difficulties in the observational estimates, and the large uncertainty in our adopted model abundances, any comparison should be viewed as a proof of concept only. In future work we intend to revisit this subject with a more sophisticated Pop II star formation model enabled.

It is also worth noting that the volume filling fraction of systems with metallicities similar to Simcoe et al. (2012) ($Z/Z_{\odot} = 10^{-4} - 10^{-3}$) is $\mathcal{F}_V = 10^{-5} - 10^{-3}$, regardless of column density, suggesting that these systems are very rare in our simulation volume.

## 2.4 Summary and Conclusions

We develop a new sub-grid model for Pop III star formation (P3L) in high-resolution cosmological volume simulations. We utilize the P3L model to study the baseline metal enrichment of galaxies in the first billion years of cosmic history. We would like to remind the reader, when examining these results, that we are only considering metal enrichment from Pop III star formation. Therefore, what we present here is an idealized numerical experiment, providing an upper limit to the ability of Pop III to enrich the early Universe. The neglected supernova feedback from Pop II star formation is expected to decrease the overall enrichment from Pop III. Conversely, our simulations here establish the ceiling for Pop III metal enrichment, which can in turn constrain attempts to interpret the chemical abundance record in extremely metal-poor objects. In future work, we will revisit

our results with Pop II star formation and feedback self-consistently included. Our major conclusions are as follows:

- We find that our legacy Pop III model of star formation produces a Pop III SFRD which is consistent with both observations of Pop II dominated systems, and numerical studies at $z \gtrsim 7.5$. When the effects of the UV ionizing background are considered, the Pop III SFRD peaks at a value of $\sim 10^{-3}$ $M_{\odot}yr^{-1}Mpc^{-1}$ near $z \simeq 10$.

- The mean enrichment from Pop III star formation rises smoothly between $z \simeq 25 - 7$, but does not exceed the critical metallicity, $Z_{\rm crit} = 10^{-4}\ Z_{\odot}$, required for the Pop III to Pop II transition until $z \simeq 7$.

- The baseline average metal enrichment from Pop III star formation for bound, star forming systems (i.e. dark mater haloes) is $Z \sim 10^{-3}\ Z_{\odot}$. We also find that a maximum enrichment ("Pop III plateau") of $Z \simeq 10^{-2}\ Z_{\odot}$ emerges as star formation in haloes with $Z > Z_{\rm crit}$ must be fueled by the accretion of pristine gas creating a quasi equilibrium between mass growth and enrichment.

- At $z$=7.5, *all* dark matter haloes with $M_h \geq 10^9\ M_{\odot}$ contain metals from Pop III star formation. This fraction falls to 62% of haloes with $M_h \geq 10^8\ M_{\odot}$ and to 7% for $M_h \geq 10^7\ M_{\odot}$.

- Only a very small fraction ($\mathcal{F}_V \sim 10^{-2.8}$)of the simulation volume is enriched by Pop III star formation to values beyond $Z_{\rm crit}$. For enrichment levels of

$\log Z/Z_\odot \geq -3, -2, -1$, the respective volume filling fractions are $\mathcal{F}_V \sim 10^{-3}, 10^{-5}, 10^{-8}$ at $z$=7.5.

- While locally star forming haloes are quickly enriched to $Z > Z_{\rm crit}$, globally Pop III star formation is not a "self-terminating" process, and requires instead the influence of ionizing photons produced from Pop II star formation. This is in contrast to conclusions from previous work (Yoshida et al., 2004). The primary difference in our study is the adoption of an IMF which allows for less massive Pop III stars as opposed to only stars with $M_* \simeq 100 - 300\ M_\odot$ as in the Yoshida et al. (2004) work. Our less top heavy IMF reduces both the metal yield and radius of enrichment for each Pop III star formation event.

- Within the bound systems we find that a bimodal distribution of haloes emerges which is distinguishable by either being internally or externally enriched. The population of haloes which has been enriched by external processes (i.e. nearby halo star formation events, accretion of enriched gas, merger events) makes up approximately 45% of the $z = 7.5$ haloes. These low mass systems exhibit a metallicity floor of $Z \simeq 10^{-6.5}\ Z_\odot$, which is much lower than their more massive ($M_h \gtrsim 10^{7.5}\ M_\odot$), star-forming counterparts. By connecting progenitors and descendants, we find that the externally enriched systems found at $z$=20 quickly merge with the nearby star forming haloes.

- Using absorption spectra created from a sample of our simulated volume which contains the unique abundance pattern of exclusive Pop III enrichment, we find equivalent widths for selected ions in good agreement with $z$=7.04

DLA observations (Simcoe et al., 2012). This agreement lends support to the authors' conclusion that the region could have been enriched by stars with a Pop III-like IMF.

- We find that, at $z$=7.5, the critical neutral hydrogen column density below which metals from Pop III are no longer present is $N_{\rm HI,crit} \sim 10^{11}{\rm cm}^{-2}$.

Cosmic metal enrichment is a complex, multi-generational process, and it is intriguing to be able to directly probe the very first episodes of this long history. With ongoing simulations of high-$z$ star and galaxy formation, like the work presented here, we are constructing a heuristic net for discovery with the upcoming frontier telescopes, such as the *JWST* and the extremely-large telescopes on the ground (GMT, TMT, E-ELT).

## Acknowledgments

Support for Program number HST-AR-14569.001-A (PI Jaacks) was provided by NASA through a grant from the Space Telescope Science Institute, which is operated by the Association of Universities for Research in Astronomy, Incorporated, under NASA contract NAS5-26555. VB is supported by NSF grant AST-1413501. This work used the Extreme Science and Engineering Discovery Environment (XSEDE), which is supported by National Science Foundation grant number ACI-1053575, allocation number TG-AST120024.

# Chapter 3

# Dust extinction in the first galaxies[1]

## 3.1 Overview

One of the fundamental goals in the study of galaxy evolution is the quest to observe the first galaxies. With the launch of the *James Webb Space Telescope (JWST)* on the horizon, this goal may be attainable. However, challenging questions remain. *How will we know when we have found them, and what will be their observational signatures?* To begin, we must have a workable definition for what a "first galaxy" is. For the purpose of this work, where we straddle the line between theory and observations, we define a "first galaxy" to be the earliest observable object which is gravitationally bound to a dark matter halo, and which is undergoing, or has undergone, Population III (Pop III) and at least one episode of Population II (Pop II) star formation (Bromm & Yoshida, 2011). Since we are requiring Pop II stars to be present, we limit our analysis to dark matter halos with sufficient mass to promote efficient cooling via $H_i$ ($M_{\rm halo} \gtrsim 10^7\ M_\odot$).

Within this definition one would expect these galaxies to host young stellar populations and contain gas which is minimally enriched with metals from supernova

[1]This chapter has been published as Jaacks J., Finkelstein S. L., Bromm V., 2018a, MNRAS, 475, 3883. S. L. Finkelstein, and V. Bromm supervised the project.

(SN) events. Observationally, systems with the above characteristics would exhibit very blue, steep UV power-law spectral slopes ($f_\lambda \propto \lambda^\beta$), as young, hot stars dominate the spectra. Intrinsic UV stellar spectral slopes of $\beta_{\rm UV} \sim -3.0$ are predicted from stellar evolution models for young, very low metallicity ($Z_* \lesssim 10^{-3} Z_\odot$) stellar populations (Schaerer, 2003b). Any deviations from this intrinsic slope are typically attributed to physical properties of the interstellar medium (ISM) through which the photons propagate, such as metallicity, density, dust content, and ionization state.

Observations at intermediate redshifts ($z \sim 3$) have shown that $\beta_{\rm UV}$ is correlated with far-infrared (FIR) dust emission (e.g. Meurer et al., 1999; Reddy et al., 2012). These results indicate that UV photons are readily absorbed and scattered by dust grains which are in turn heated, re-radiating in the FIR. Intense efforts extend to higher redshifts ($z \geq 6$), as $\beta_{\rm UV}$ is a key parameter to model reionization. It can be directly measured from broadband photometry, and thus is accessible out to the highest redshifts currently reached ($z \sim 10$; Wilkins et al. 2016). Early results from Bouwens et al. (2010b) and Finkelstein et al. (2010) found evidence for $\beta_{\rm UV} \sim -3.0$ ($\pm$0.2–0.5), suggesting extremely metal-poor stellar populations and no dust extinction, albeit with no conclusive evidence for primordial star formation. However, more recent studies have benefited from larger sample sizes and improved bias corrections, finding $\langle \beta_{\rm UV} \rangle \sim -2.2$ to $-2.4$ ($\pm$ 0.30) for faint ($M_{UV} \sim -18$) galaxies at $z \simeq 7$, again indicative of little dust attenuation, but non-primordial stellar populations (McLure et al., 2011; Dunlop et al., 2012; Finkelstein et al., 2012b; Bouwens et al., 2014). These results imply that galaxies hosting primordial

star-formation must reside at even higher redshifts, and/or at fainter luminosities.

There have been a number of pioneering studies which have utilized sophisticated spectral synthesis and evolution codes to predict the photometric properties of the first galaxies (e.g. Schaerer, 2002; Zackrisson et al., 2013). While providing detailed predictions for the spectral energy distribution, given assumptions regarding key physical properties (such as halo mass, escape fraction, and age), these investigations lack the ab initio cosmological context that numerical simulations can provide. The latter enable to trace the realistic transport of heavy chemical elements in the evolving three-dimensional cosmic web, as is done here. There has also been a vigorous effort to leverage cosmological simulations in conjunction with spectral evolution codes to predict photometric "first galaxy" properties (e.g. Wilkins et al., 2016; Barrow et al., 2017; Zackrisson et al., 2017). However, these works focus on the properties of typical, already more evolved, high-redshift galaxies. Here, on the other hand, our focus is on the chemically most primitive galaxies, where the first Pop II clusters form out of material that has only been enriched by Pop III (Jaacks et al., 2018b). This allows us to establish a baseline beta slope, the extreme blue limit of $\beta$ that may be detectable with the *JWST*. Our goal for this work is to help guide interpretations of the next generation deep-field surveys, in particular in terms of how close to "first light" a given source is.

The paper is structured as follows. In Section 3.2 we describe our numerical methodology, and in Section 3.3 and 3.4 we present our results and conclusions.

## 3.2 Numerical methods

For this work, we utilize a customized version of the publicly available next generation hydrodynamics code GIZMO, which employs a Lagrangian meshless finite-mass (MFM) methodology for solving the equations of fluid dynamics (for details regarding simulations and sub-grid models, see Jaacks et al. 2018b). GIZMO offers improved numerical accuracy and efficiency by combining features of smoothed particle hydrodynamics (SPH) and adaptive mesh refinement (AMR) codes.

### 3.2.1 Simulations

Our simulation volume, designed to approximately replicate a single pointing with *JWST* at redshift $z \sim 10$, has a box size of $4h^{-1}$ Mpc and contains $512^3$ particles of both gas and dark matter. We adopt a $\Lambda$ cold dark matter ($\Lambda$CDM) cosmology, consistent with the recent *Planck* results: $\Omega_m = 0.315$, $\Omega_\Lambda = 0.685$, $\Omega_b = 0.047$, $\sigma_8 = 0.829$, and $H_0 = 100h\,\mathrm{km\ s^{-1}\ Mpc^{-1}} = 67.74\ \mathrm{km\ s^{-1}\ Mpc^{-1}}$ (Planck Collaboration et al., 2016). Our initial conditions are generated at $z = 250$, using the MUSIC initial conditions generator (Hahn & Abel, 2011).

The simulations employ our custom-built Pop III legacy (P3L) star formation sub-grid model which focuses on the long-term impact of Pop III on the surrounding medium. Specifically, our model is designed to track metals which enrich the early ISM through SN explosions. The P3L approach allows each Pop III star forming region to have a randomly selected population, drawn from a given initial mass function (IMF), here taken to be top heavy with a slope of $\alpha = -0.17$ and an

exponential cutoff below $M_* = 20\ M_\odot$ ( see Section 2.4 for detailed motivation). This random process endows each region with a unique metal enrichment, in terms of amount and spatial extent. We also include a Pop II proxy (P2P) sub-grid model to approximate the ionization and Lyman-Werner feedback from contemporaneous Pop II star formation, but neglect any additional metal enrichment from Pop II.

Dark matter haloes are identified with a post processing 3D friends-of-friends (FOF) algorithm, using a minimum particle number of 32 and a linking length of 0.15 times the inter-particle distance. Gas particles and their respective properties are then associated with each halo by searching within its virial radius. Grouping and data extraction are aided by the *yt* (Turk et al., 2011) and *Ceasar* (Thompson, 2014) software packages.

### 3.2.2 Interstellar extinction

Determining the dust extinction in the high-$z$ ISM is non-trivial, both observationally and theoretically. The primary difficulty lies in ascertaining the quantity and physical nature of the dust particles, including their size, composition, shape, and optical properties. These details are folded into an empirically determined extinction curve (e.g., Calzetti et al., 2000), where the optical depth is

$$\tau_\lambda = 0.921 k(\lambda) E(B-V). \tag{3.1}$$

The wavelength dependence of the Calzetti et al. attenuation curve is expressed as

$$k(\lambda) = \begin{cases} 2.659(-1.857 + 1.040/\lambda) + 4.05, \\ \text{for } 0.63\mu m \leq \lambda \leq 2.20\mu m \\ 2.659(-2.156 + 1.509/\lambda - 0.198/\lambda^2 + 0.011/\lambda^3) + 4.05, \\ \text{for } 0.12\mu m \leq \lambda \leq 63\mu m. \end{cases} \tag{3.2}$$

Assuming an intrinsic model spectrum, the overall $E(B-V)$ can then be determined by fitting to the observed broadband photometry of the system. The exact details regarding the physical properties of dust in the early ISM are highly uncertain. Therefore, we will assume for simplicity that dust from Pop III star formation is characterized by the Calzetti law. Solving the radiative transfer equation, simplified for pure absorption, we have

$$f_\lambda = f_\lambda(0) e^{-\tau_\lambda}. \tag{3.3}$$

Here, $f_\lambda(0)$ is the intrinsic flux representing the stellar population (see Section 3.2.3), and $\tau_\lambda$ is the total optical depth along the line of sight (LOS), given by Equ. 3.1.

From our simulations, we can determine the dust reddening for a given system with the normalized relation (Bohlin et al., 1978; Rachford et al., 2009)

$$E(B-V) \simeq \frac{N_{\rm HI}}{5.8 \times 10^{21} {\rm cm}^{-2}} \frac{Z}{Z_\odot} \frac{\zeta}{\zeta_\odot} \, . \tag{3.4}$$

We estimate the neutral hydrogen column via $N_{\rm HI} \simeq \rho_{\rm gas}/(\mu m_{\rm H}) L_{\rm char}$, where $L_{\rm char}$ is the characteristic length scale of the system. The metallicity ($Z$) is extracted directly from the enriched gas, and we set the metal-to-dust ratio to $\zeta/\zeta_\odot \equiv 1.0$, where $\zeta_\odot \approx 0.50$.

### 3.2.3 Stellar populations

In this work, we utilize Pop II stellar clusters as flashlights which illuminate the Pop III enriched ISM of our simulated galaxies. To represent a Pop II intrinsic simple stellar population (SSP), we adopt models from Schaerer (2003b), containing evolutionary tracks for very low metallicity ($Z_* \lesssim 10^{-2}\, Z_\odot$). This value is consistent

with the maximum Pop III enrichment found in Jaacks et al. (2018b), and represents the ISM conditions from which Pop II stars form. We consider young stellar populations with ages of 10 Myr and 50 Myr which have experienced a constant star formation history, with a Salpeter (1955) IMF over a mass range of $1-100\,M_{\odot}$. Note that we intentionally limit the age of our stellar populations in order to represent the extreme scenario studied here, where Pop II star formation is just beginning, and spectra exhibit their bluest shapes.

The resulting intrinsic spectra are shown by the solid black and gray lines in Figure 3.1, where the flux is normalized to a Pop II stellar mass of 1 $M_{\odot}$, which can be scaled to the total stellar mass of any galaxy. Since nebular continuum emission is a potential reddening factor, we show $\beta_{\rm UV}$ assuming Lyman continuum escape fractions of $f_{\rm esc}$ = 1 and 0.

## 3.3 Results

### 3.3.1 Mean halo extinction

We first explore the mean Pop III extinction for each halo identified in our simulations at $z$=7.5. The extinction value for each halo is calculated by assuming the total gas and metals are distributed homogeneously within the half mass radius ($R_{1/2}$) of the halo. These halo averaged properties are then employed to calculate the halo averaged Pop III extinction, using Equ. 3.4 and $L_{\rm char} = R_{1/2}$.

In Figure 3.2, we present the mean halo $E(B-V)$ as a function of halo mass with the mean metallicity indicated by the colour scale. There is a clear correlation between halo mass, extinction and the amount of metals found in the

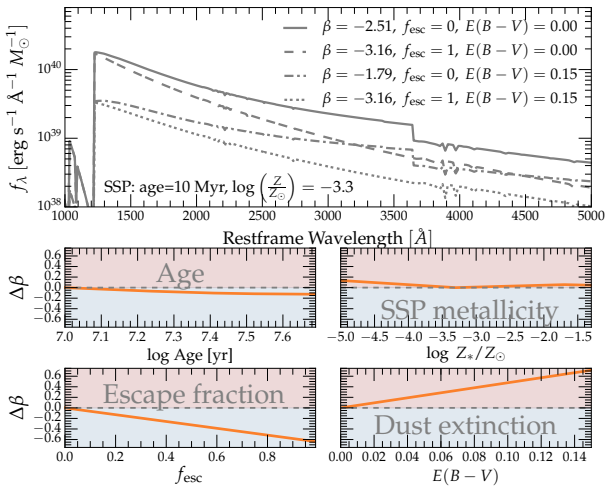


Figure 3.1: Parameter sensitivity of the UV spectral slope $\beta_{\rm UV}$. The series of gray lines represents an SSP with and age of 10 Myr and $\log(Z/Z_\odot) = -3.3$, with varying values of $f_{\rm esc}$ and E(B-V). $\beta_{\rm UV}$ are measured by performing a least-squares fit over a rest-frame wavelength range of 1200 – 2600 Å. The bottom panels show the impact of individual parameters (age, metallicity, $f_{\rm esc}$, and $E(B-V)$) on $\beta_{\rm UV}$ where $\Delta\beta \equiv \beta_{\rm SSP} - \beta_{\rm param}$. For each panel only the indicated variable is varied and all others are fixed. It should be noted that, while the limited age range considered here has little impact on $\Delta\beta$, stellar populations older than those studied here would be characterized by significantly redder values of $\beta$.

halo. This relation is due to the fact that higher mass haloes typically experience higher star formation rates, which will lead to more metals injected into the ISM and, consequently, more dust. The relationship is well described by a power-law $\langle E(B-V)\rangle \propto M_{\rm halo}^{0.80}$. The maximum Pop III extinction occurs in a halo with $\log(M/M_{\rm halo}) = 10.15$, which has a mean metallicity of $\log(Z/Z_{\odot}) = -2.12$, leading to $E(B-V)_{\rm max} = 3.3 \times 10^{-3}$ ($A_{\rm V,max} = 1.3 \times 10^{-2}$). On average, we find that haloes with $\log(M/M_{\rm halo}) \geq 8.0$ have $\langle E(B-V)\rangle \approx 2.1 \times 10^{-4}$, and those with $\log(M/M_{\rm halo}) \geq 9.0$ show $\langle E(B-V)\rangle \approx 8.7 \times 10^{-4}$. Averaged over the entire halo, Pop III metals thus have a negligible impact on the intrinsic $\beta_{\rm UV}$.

### 3.3.2 Column density

In the previous section, we averaged physical properties over the entire halo gas. The downside of this approach is that high density and high metallicity regions in the ISM can be diluted. To explore this possibility, we examine the properties of each gas particle, or resolution element, contained in our simulation volume. We are thus more accurately modeling the Pop III extinction experienced by a photon if it were to pass directly through a given gas cloud.

In Fig. 3.3, we show $E(B-V)$, calculated from Equ. 3.4, versus column density, with colour corresponding to gas metallicity, for each particle. Here, we use the local Jeans length, calculated for each gas particle, as the characteristic length scale ($L_{\rm char} = L_{\rm J}$). Since our simulations do not directly include Pop II star formation, we would tend to over-estimate the extinction in dense, metal-rich gas using the above methodology, as feedback from Pop II star formation would

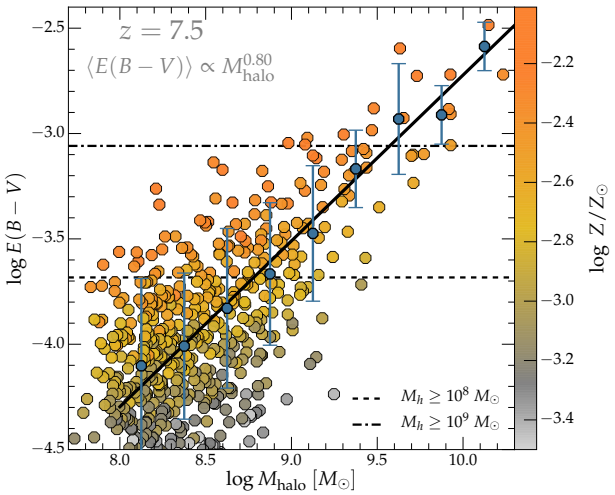


Figure 3.2: Dust reddening for haloes at $z$=7.5. Orange-gray symbols show the mean $E(B-V)$ as a function of halo mass. The color shading indicates the mean metallicity in solar units. The maximum value of $E(B-V)_{\rm max} = 3.3\times10^{-3}$ ($A_{\rm V,max} = 1.3\times10^{-2}$) is reached for $\log(M/M_{\rm halo}) = 10.15$, where $\log(Z/Z_\odot) = -2.12$. The black dashed and dash-dotted lines represent the mean extinction for haloes with $\log(M/M_{\rm halo}) \geq$ 8.0 and 9.0, respectively. The blue symbols represent mean $E(B-V)$ for a given halo mass range with $1\sigma$ error bars. A linear least-squares fit to the mean values is provided as the solid black line.

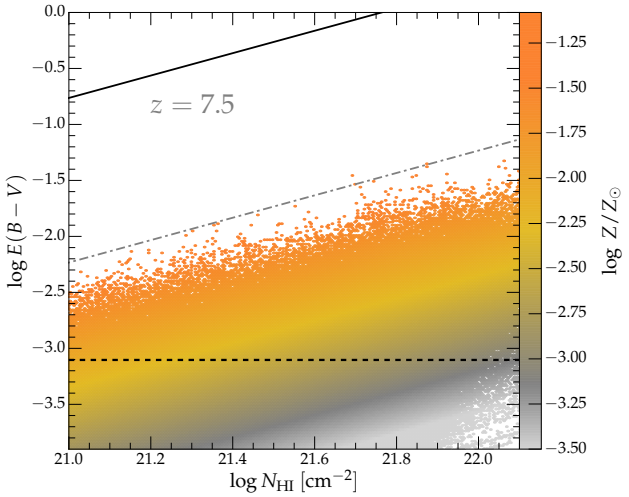


Figure 3.3: 2-D histogram of the $H_i$ column density ($N_{H_i}$) vs. the calculated $E(B-V)$ with hexagonal binning for gas bound to a dark matter halo. As in Fig. 3.2, color indicates gas metallicity, and $E(B-V)$ is calculated by taking the characteristic length to be the local Jeans length ($L_{char} = L_J$). The dashed black line represents the mean Pop III extinction ($\langle E(B-V)\rangle = 6.6 \times 10^{-4}$) for all non-zero metallicity halo gas particles. For reference, the black solid line represents the Milky Way normalized value (Equ. 3.4), and the gray dashed-dotted line is a scaled down version to guide the eye.

disrupt such clouds. To compensate, we exclude any gas particles which would qualify for Pop II star formation in a standard sub-grid model (i.e. $n > 100$ cm$^{-3}$ and $Z > 10^{-4}\ Z_\odot$). The metals contained in such particles are distributed to the surrounding ISM so as to conserve total metal mass. We find a maximum Pop III extinction of $E(B-V)_{max} = 0.03$ ($A_{V,max} = 0.13$), considerably higher than the estimate from Sec. 3.3.1. The average for all non-zero metallicity gas particles in Fig. 3.3 is $\langle E(B-V)\rangle \approx 6.6 \times 10^{-4}$.

### 3.3.3 Galaxy LOS

Finally, we examine individual LOS directions through the galaxy identified in Sec. 3.3.1 to exhibit the highest average Pop III extinction value. Here, we use a binning process to place each particle in a grid cell, after which we sum the gas and metal mass of each cell along the $z$-axis. The column density and subsequent extinction is then calculated for each LOS using Equ. 3.4, shown in Fig. 3.4 with colour representing the $E(B-V)$ due to Pop III enrichment. The gray pixels indicate the overall extent of the zero-metallicity gas. With this method we find a maximum of $E(B-V)_{\rm max} = 0.07$ ($A_{\rm V,max} = 0.28$), and a mean value of $\langle E(B-V)\rangle = 3.4\times10^{-4}$, only slightly higher than those found in Sec. 3.3.2. This is not unexpected as we are summing the extinction along a LOS through the most dense and metal rich region of the galaxy. However, this maximum value should be viewed as an extreme upper limit as it represents extinction experienced though the entire LOS ($\sim$ 2.4 kpc). A more likely scenario is that star forming regions would be embedded at different depths along the LOS and thus experience varying levels of extinction. A more realistic emerging spectrum would be composed of a composite of these spectra and likely present less attenuation.

### 3.3.4 Baseline Pop III spectral slope

We now employ a Monte Carlo sampling technique to produce representative model spectra, and derive spectral slopes, $\beta_{\rm UV,PopIII}$, for Pop III enriched galaxies. We randomly sample over a range of dark matter halo mass, SSP age and metallicity, $f_{\rm esc}$, and $E(B-V)$. Dust extinction is sampled from the relationship between halo

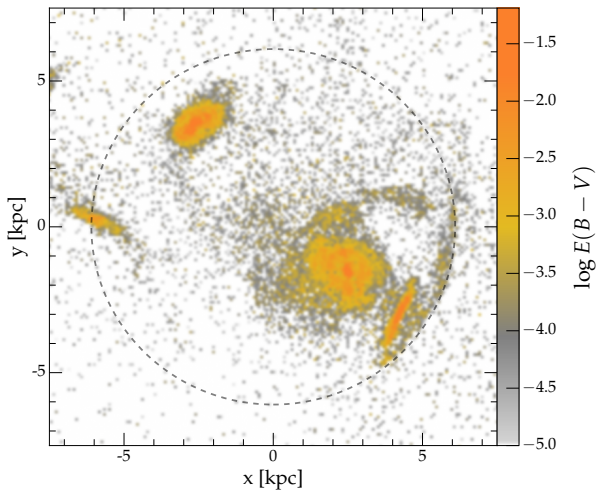


Figure 3.4: Projected $E(B-V)$, calculated for the halo with the highest simulated extinction level ($M_{\rm halo} \approx 10^{10}\ M_{\odot}$). Each pixel represents the sum along the z-axis. Along the most metal-rich, dense LOS we find $E(B-V)_{\rm max} = 0.07$ ($A_{\rm V,max} = 0.28$), and a mean value of $\langle E(B-V) \rangle = 3.4 \times 10^{-4}$. The dashed circle indicates the half mass radius ($R_{1/2}$) for this halo. Note that the gray pixel "noise" is an artifact of the binning process, but does represent the overall extent of zero-metallicity gas in the image.

Table 3.1: Parameter ranges for Monte Carlo sampling to calculate baseline $\beta_{\rm UV,PopIII}$, as presented in Fig. 3.5. For $f_{\rm esc}$, we adopt results from the FiBY simulations (Paardekooper et al., 2015), which provide escape fraction probability distributions as function of halo mass. Based on results in Finkelstein 2017 (in-prep), we apply a correction factor of $\sim 5$ to the Paardekooper et al. (2015) escape fractions in order to reconcile observations and re-ionization calculations. All parameters are drawn uniformly between lower and upper limits, unless otherwise constrained by an underlying distribution, as is the case for $f_{\rm esc}$ and $E(B-V)$.
1pt 6pt

| Parameter | Range | Source |
|---|---|---|
| DM halo mass | $10^8 - 10^{10}\ M_\odot$ | Simulation resolution |
| SSP age | 10 – 50 Myr | Observed estimate |
| SSP metallicity | $10^{-5} - 10^{-1}\ Z_\odot$ | Jaacks et al. (2018b) |
| $f_{\rm esc}$ | $0 - 1$ | Paardekooper et al. (2015) |
| $E(B-V)$ | $\propto M_h^{0.80}$ | This work (Figure 3.2) |

mass and metallicity provided in Figure 3.2, and $f_{\rm esc}$ is taken from results presented in Paardekooper et al. (2015), who use the FiBY simulations to derive distribution functions for $f_{\rm esc}$ as a function of halo mass. Halo mass, age and SSP metallicity are drawn from a uniform distribution. For each set of parameters, a model spectrum is created (Schaerer, 2003b), in turn providing the resulting UV spectral slope.In the case of age and intrinsic metallicity, we use linear interpolation between the two closest models. The full list of parameters, references and range of possible values can be found in Table 3.1.

In Figure 3.5, we present the results of our random sampling study. The most striking feature is that the median value of $\left\langle \beta_{\rm UV,PopIII} \right\rangle = -2.5 \pm 0.07$ appears to be roughly constant across all halo masses considered in this work with only a

slight dip at $M_{\rm halo} = 10^{8.5}\ M_{\odot}$. This can be understood by further examination of the primary contributors to $\Delta\beta$, $E(B-V)$ and $f_{\rm esc}$ (see bottom panels of Fig. 3.1). In the case of $E(B-V)$, there is a strong correlation of increasing Pop III extinction with increasing halo mass (Fig. 3.2). However, the amount of Pop III extinction is extremely low ($E(B-V) < 10^{-3}$), with negligible impact on the $\beta_{\rm UV,PopIII}$ slope, leaving $f_{\rm esc}$ as the primary factor. The mean $f_{\rm esc}$, calculated from the Paardekooper et al. (2015) probability distributions, are also roughly constant over our range of halo masses, with $\langle f_{\rm esc} \rangle = 0.14, 0.06, 0.15, 0.15$ for $\log M_{\rm halo}/M_{\odot} = 8.0, 8.5, 9.0, 10.0$, respectively. It is worth noting that our adopted values for $f_{\rm esc}$ are very consistent with those found in Wise et al. (2014) at the upper limit of their studied mass range ($M_{\rm halo}/M_{\odot} = 8.0, 8.5$). Finally, the near redshift independence of $f_{\rm esc}$ implies a $\beta_{\rm UV,PopIII}$ floor which is also largely redshift independent.

Over the same age range, our primary result of $\left\langle \beta_{\rm UV,PopIII} \right\rangle = -2.51 \pm 0.07$ is consistent with the study by Zackrisson et al. (2013), who assumed a fixed SSP metallicity and $f_{\rm esc}$ to determine $\beta$ as a function of age. The primary improvement here is that SSP metallicity and $E(B-V)$ are directly extracted from our simulation, as well as the utilization of detailed distribution functions for $f_{\rm esc}$ from Paardekooper et al. (2015). Our work is also differentiated by the fact that we focus on the most extreme, chemically primitive scenario, in and effort to predict the baseline $\beta$ value, whereas Zackrisson et al. (2013) explore a wide parameter space to offer predictions for many physical settings.

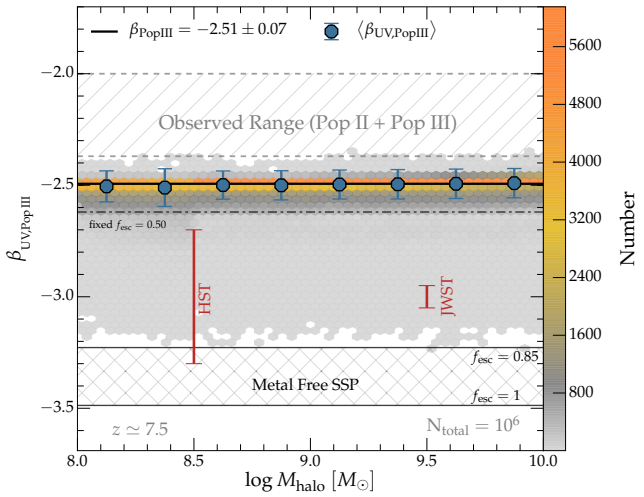


Figure 3.5: UV spectral slopes from Pop II SSPs reddened by Pop III dust, $\beta_{\rm UV,PopIII}$, calculated from the Monte Carlo sampling of the relevant parameter space (see Table 3.1). Blue symbols indicate median values with $1\sigma$ error bars, and the solid black line is a linear least-squares fit. The gray-orange shaded region represents the density of calculated $\beta_{\rm UV,PopIII}$ values. The observed range of Pop II + Pop III extinction at $z \sim 7$ and $M_{\rm UV} \sim -18.5$ is indicated by the region with diagonal lines (from Finkelstein et al. 2012b; Bouwens et al. 2014; Dunlop et al. 2013). The red error bars denote the approximate uncertainty on measuring $\beta$ at this magnitude with the *HST*, and the expected improvement with *JWST*.

## 3.4 Summary and Conclusions

Using cosmological volume simulations and a custom built sub-grid model for Pop III star formation, we examine the baseline dust extinction due to metals produced by Pop III in the first billion years of cosmic history. Our major conclusions are as follows:

- Dust extinction due to Pop III star formation is strongly correlated with halo mass when averaged over the system, expressed as $E(B-V) \propto M_{\rm halo}^{0.80}$ (Fig. 3.2). However, the overall extinction due to Pop III is very low ($E(B-V) < 10^{-3}$) and contributes little to changing the overall $\beta$ slope.

- When considering column densities of individual gas clouds which are bound to dark matter haloes, we find an average Pop III extinction of $\langle E(B-V)\rangle = 6.6 \times 10^{-4}$.

- Integrated lines-of-sight within a given halo can, in very limited cases, exhibit Pop III extinction values as high as $E(B-V)_{\rm max} = 0.07$ ($A_{\rm V,max} = 0.28$) along the most metal rich, dense LOS (Fig. 3.4).

- Statistical Monte Carlo studies of constrained parameters which control $\beta_{\rm UV,PopIII}$ (halo mass, age, metallicity, escape fraction, and dust extinction) suggest that $\left\langle \beta_{\rm UV,PopIII} \right\rangle = -2.51 \pm 0.07$ would be representative of extremely metal poor galaxies with $Z < 10^{-2} Z_{\odot}$.

In interpreting the results presented in Fig. 3.5, consider a scenario in which a future deep-field observation detects an object at $z \geq 7.5$ with a $\beta_{\rm UV} \sim -3.0$.

*What would this tell us?* Our analysis here suggests that such an extreme UV spectral slope would be indicative of being generated by a very young, Pop II star forming galaxy, which experiences minimal nebular emission and has been enriched by only Pop III-produced metals. Such systems would be excellent targets for deep ground-based spectroscopic follow-up observations with resources such as the Giant Magellan Telescope (GMT). Given current error bars for $\beta_{\rm UV}$ measurements ($\pm 0.3$ at $M = -18$, the limit of the Hubble Ultra Deep Field at $z > 7$), it would be challenging to uniquely identify a truly Pop III star forming galaxy, with estimated slopes of $\beta_{\rm UV} \lesssim -3.0$. Future *JWST* deep-field campaigns will have significantly reduced error bars at these same magnitudes ($\pm 0.05$), offering the exciting possibility to uniquely identify low-$Z$ stellar populations.

Our results indicate that the reddening experienced by $z \geq 7$ dwarf galaxies is almost entirely due to nebular emission. However, we here have considered only the baseline enrichment from Pop III star formation. Therefore, it is useful to provide a rough estimate of the amount of Pop II created metals which are missed in our Pop III only simulation. For this purpose, we assume a halo of $M_{\rm vir} \approx 10^{10}\ M_{\odot}$ with $Z_{\rm PopIII} \approx 10^{-2}\ Z_{\odot}$, the plateau Pop III enrichment found in Jaacks et al. (2018b). In such a halo, we have a baryonic mass of $M_{\rm B} \approx 10^{9}\ M_{\odot}$, which results in a total mass in metals of $M_{\rm Z,PopIII} \approx 10^{4}\ M_{\odot}$. To derive the Pop II metal enrichment, we use abundance matching arguments (Behroozi et al., 2013) to arrive at a corresponding stellar mass of $M_{*,\rm tot} \approx 10^{7}\ M_{\odot}$. For a standard IMF (e.g. Salpeter, 1955; Chabrier, 2003; Kroupa, 2001), there is approximately one core collapse SN (CCSN) for every $\sim 100 M_{\odot}$ ($\eta_{\rm CCSN} \sim 0.01$). If we further assume that a typical CCSN has a progenitor

mass of $M_* = 10\ M_\odot$ and a metal yield of $y_Z \sim 0.01$, we arrive at a total metal mass of $M_{\rm Z,PopII} \approx 10^4\ M_\odot$ (i.e. $M_Z \approx \eta_{\rm CCSN} M_{*,\rm tot} M_* y_Z$). This estimate, which is consistent with the more sophisticated analysis by Mancini et al. (2015), illustrates that $M_{\rm Z,PopIII} \approx M_{\rm Z,PopII}$. Thus, even with Pop II star formation included, high-$z$ dwarf galaxies are unlikely to experience a measurable degree of dust extinction, consistent with current observations. In future work, we will revisit this estimate with Pop II star formation self-consistently enabled in our simulations.

There are several caveats to this work relating to the uncertainty of several adopted models and parameters. In particular there is a high dependence upon the accuracy of the SSP models utilized (Schaerer, 2003b). If future advancements in stellar evolution and nucleosynthesis lead to more accurate modeling of extremely low-metallicity stellar populations, then the results here should be revisited. We here also adopt stellar evolutionary models which assume a constant star formation history. While it has been shown, both observationally and theoretically, that high-redshift galaxies exhibit a stochastic, rising star formation history (Papovich et al., 2011; Finlator et al., 2011; Jaacks et al., 2012b; Shimizu et al., 2014; Zackrisson et al., 2017), the low metallicity models utilized here pre-date these results.

We also adopt a fixed metal-to-dust ratio when calculating our extinction values. It has been demonstrated by Mattsson et al. (2014) that this value could be dependent on metallicity, such that higher $Z$ leads to a larger dust ratio. In the end, our choice for the metal-to-dust parameter has no impact on our results. Even if we doubled our adopted value so that 100% of the metals were converted into dust, the metallicity from Pop III star formation is too low ($\lesssim 10^{-3}$) to significantly

affect the reddening. It has also been suggested by Schneider et al. (2016) that the dust content in high-redshift systems may not solely depend on metallicity, as ISM density conditions may affect the efficiency of dust formation. Again, given the extremely low metallicities, the efficiency of dust creation will have no impact on the results reported here.

Our analysis agrees with previous studies which indicate that, in the absence of dust, Lyman continuum (LyC) radiation, re-processed into nebular continuum emission, is the dominant reddening factor for a given halo (e.g. Zackrisson et al., 2013, 2017; Wilkins et al., 2013; Barrow et al., 2017; Dunlop et al., 2012). In this work, we adopt the results presented in Paardekooper et al. (2015), who performed sophisticated radiative transfer calculations on $\sim 75,000$ simulated galaxies, taken from the FiBY simulations, to establish an escape fraction distribution for each halo mass studied. While the $f_{\rm esc}$ distribution is rather broad for each halo mass, our random draw of $10^6$ realizations exhibits a mean of $\langle f_{\rm esc} \rangle = 0.08 \pm 0.18$, when averaged over all halo masses. This implies that the majority of LyC photons are absorbed in the local ISM. Due to the strong dependence of our results on this parameter, and the uncertainties in ascertaining its physical nature, it is useful to consider the more extreme case of a fixed $f_{\rm esc} = 0.50$. For this scenario we find $\beta \approx -2.62$, which is indicated by the black dash-dotted line in Figure 3.5. A physical justification for such high escape fraction could be a star forming event which has, due to strong stellar feedback, evacuated the surrounding gas, thus facilitating the escape of LyC photons into the low-density intergalactic medium.

Finally, there is the uncertainty related to the Pop III IMF. In our simulations,

we stochastically sample each individual Pop III stellar population from a top-heavy IMF, which is essentially (logarithmically) flat within the range $8 \leq M/M_{\odot} \leq 140$. This IMF is representative of results from multiple high-resolution simulations which follow the collapse of a Pop III star forming region to very high density (e.g. Greif et al., 2011; Stacy & Bromm, 2013). While there are differences in the details of the predicted Pop III IMF across studies, the consensus view is that it is more top heavy compared to Pop II. Should future work indicate that the Pop III IMF is not as top heavy as currently predicted, such revision would be unlikely to impact our results, as the resulting overall metal production per stellar mass would remain low. This conclusion is supported by the results from Pallottini et al. (2014), indicating that the Pop III star formation rate density is largely unchanged, regardless of the assumed IMF. Testing our "blue limit predictions" with upcoming deep-field observations will provide an exciting view into the initial stages of cosmic chemical evolution.

## Acknowledgments

JJ would like to thank Daniel Schaerer for access to low metallicity and Pop III stellar evolution models. This work was supported by HST-AR-14569.001-A & HST-AR-15028.001-A (PI Jaacks), provided by NASA through a grant from the Space Telescope Science Institute, which is operated by the Association of Universities for Research in Astronomy, Inc., under NASA contract NAS5-26555. VB is supported by NSF grant AST-1413501. JJ and SLF acknowledge support from the NASA Astrophysics and Data Analysis Program award #NNX16AN47G issued

by JPL/Caltech. This work used the Extreme Science and Engineering Discovery Environment (XSEDE), which is supported by National Science Foundation grant number ACI-1548562, allocation number TG-AST120024.

# Chapter 4

# The legacy of star formation in the pre-reionization universe[1]

## 4.1 Introduction

The impending launch in $\sim$ 2020 of the *James Webb Space Telescope (JWST)* promises the capability to collect photons from a yet unexplored epoch of cosmic evolution, expanding our view to a time when the Universe was $<$ 400 Myr old. The goal of the work presented here is to elucidate the legacy left behind by star formation in the pre-reionization Universe, at redshifts $z \gtrsim 7$, with state of the art cosmological simulations. We are thus addressing the crucial period of cosmic dawn, when the simple initial conditions of the very early Universe give way to an ever increasing complexity of cosmological structure. This is a very timely endeavor, given the powerful array of next-generation observational facilities that are currently being deployed or planned.

For more than 25 years, the Hubble Space Telescope (*HST*) has been a cornerstone of modern high redshift ($z > 5$) astronomy. The 2009 installation of the near-infrared Wide Field Camera 3 (WFC3) instrument aboard *HST* opened up the $z > 7$ Universe with a myriad of new photometric targets (e.g. Oesch et al.,

[1]This chapter has been submitted to MNRAS as Jaacks J., Finkelstein S. L., Bromm V., 2018. S. L. Finkelstein, and V. Bromm supervised the project.

2009; Ouchi et al., 2009; Bouwens et al., 2010a; Finkelstein et al., 2010, 2012b; Yan et al., 2010; Trenti et al., 2011; Wilkins et al., 2011). Large survey programs, such as CANDELS, BoRG, HUDF09/12, GOODS, CLASH, and the Hubble Frontier Fields (HFF), have discovered galaxies with luminosities spanning ∼10 magnitudes, and transformed our understanding of how the Universe has evolved over its first billion years.

*JWST* will extend this dynamic range by $\sim 3$ magnitudes ($m_{\rm AB} \approx 32$ in a ∼200 hr blank field). Early release science programs, such as the Cosmic Evolution Early Release Science Survey(CEERS: Finkelstein et al., 2017), anticipate the detection of $\sim 50$ new $9 \leq z \leq 13$ galaxies in a 100 arcmin$^2$ field with up to 10 residing at $z > 11$. For context, there is currently only one spectroscopically confirmed galaxy at these redshifts from *HST* ($z = 11.1$; Oesch et al., 2016). Equipped with this new information, we will begin to address several key questions which have been raised over the past decades of *HST* observations, such as: Is there a "dearth" of galaxies at $z > 10$ as suggested by Oesch et al. (2018)? Does the UV luminosity function (UVLF) turn over, or maintain its power-law behaviour, at the faint-end? Will we directly detect the first generation of stars, the so-called Population III (Pop III)? If not, can we detect the legacy left behind by Pop III processes, such as supernova (SN) explosions, metal-enriched absorption systems, or star clusters? Where should we look for these signatures?

The past decade has seen a slew of pioneering numerical work which has provided quantitative predictions for the upcoming *JWST* mission (e.g. Tornatore et al., 2007; Maio et al., 2010; Salvaterra et al., 2011; Jaacks et al., 2012a; Wise

et al., 2012, 2014; Dayal et al., 2013; Johnson et al., 2013; Muratov et al., 2013; Genel et al., 2014; Pallottini et al., 2014; Feng et al., 2016; Ma et al., 2017). These studies have also begun to explore many of the fundamental questions mentioned above. For example, Wise et al. (2014) utilized the adaptive mesh refinement (AMR) code ENZO (The Enzo Collaboration et al., 2014), which is able to achieve excellent spatial resolution in select regions to study galaxy evolution at $z > 7$. More specifically, this work focused on the impact of dwarf galaxies in low-mass haloes, $6.5 \leq \log(M_{\rm halo}/M_{\odot}) \leq 8.5$, on the ionizing photon budget in the pre-reionization epoch. Wise et al. (2014) present evidence that, even though below $M_{\rm UV} \sim -12$ the UVLF flattens, dwarf galaxies contribute $\sim 30\%$ of the ionizing photons at $z$=6.

Work by Johnson et al. (2013) analyzed data from the First Billion Years (FiBY) simulation which utilized the smoothed particle hydrodynamics (SPH) code GADGET to focus on the evolution of the $z > 6$ Universe. This investigation finds that significant Pop III star formation continues down to at least $z \sim 6$, which, even though directly undetectable by *JWST*, gives hope for the possibility of observing a Pop III spawned pair instability supernova (PISN). They calculate that at $z$=10, there could be up to one PISN visible per deg$^2$ per year (see also Scannapieco et al., 2005). Using the AMR code RAMSES to explore cosmic metal enrichment within the first galaxies, Pallottini et al. (2014) also find evidence for substantial Pop III star formation, with star formation rate density (SFRD) $\sim 10^{-3}\ M_{\odot}\ {\rm yr}^{-1}\,{\rm Mpc}^{-3}$, down to $z$=6. Afterwards, Pop III is rapidly quenched. They estimate that Pop III constitutes $\sim 10\%$ of the total star formation at $z \sim 7$. These authors also find that the mean total metallicity in their simulation volume from both Pop III and Pop II,

$Z_{\rm Pop\ III} + Z_{\rm Pop\ II}$, does not cross the critical metallicity required for the Pop III/II transition ($Z_{\rm crit} = 10^{-4}\ Z_{\odot}$) until $z \sim 8.5$. The volume filling fraction of gas with $Z > Z_{\rm crit}$ is $\sim 10^{-3}$ at the same redshift, leaving a large reservoir of zero- or low-metallicity gas for ongoing Pop III star formation.

The rapid pace of discovery implies that early predictions are not directly applicable to interpret recent frontier observations. The latter, however, can provide critical guidance in developing and testing cutting-edge numerical experiments. A case in point is the discovery of the previously mentioned $z = 11.1$ galaxy (Oesch et al., 2016), identified by *HST* in the CANDELS/GOODS-N data, which to date provides our only direct constraints for the physical properties of $z \gtrsim 10$ galaxies. Specifically, this galaxy is $\sim 3$ times brighter than a typical $L_*$ galaxy at $z$=7, has an estimated stellar mass of $M_* = 10^9\ M_{\odot}$, and is forming stars at a rate of $\sim 25\ M_{\odot}\ {\rm yr}^{-1}$. This rapid rate of star formation presents a challenge for standard galaxy formation models. Livermore et al. (2017) use data from the HFF to address the early predictions from Jaacks et al. (2013) and Wise et al. (2014), claiming a turnover or flattening of the UVLF at $z \geq 6$. Studying ~170 lensed $z > 6$ galaxies, Livermore et al. (2017) find steep faint-end slopes of $\alpha_{\rm UV} < -2$, but no evidence for any deviation from the power-law form down to limiting magnitudes of $M_{\rm UV} \sim -12.5$ at $z \sim 6$, $M_{\rm UV} \sim -14.5$ at $z \sim 7$, and $M_{\rm UV} \sim -15$ at $z \sim 8$ (see also Atek et al., 2015; Yue et al., 2016). Conversely, considering Local Group descendants, Boylan-Kolchin et al. (2015) argue that a flattening of the UVLF around the limits set by Livermore et al. is required to match Milky Way satellite galaxy number counts and reionization constraints at the limits probed by observations (see

also Boylan-Kolchin et al., 2014). A similar lensing program with *JWST* should enable exploration down to absolute UV magnitudes of $M_{\rm UV} \sim -11$, thus promising to greatly enhance our understanding of the UVLF.

Most recently, results from the Experiment to Detect the Global EoR Signature (EDGES; Bowman et al., 2018) provide hints for the very onset of cosmic star formation. EDGES employs a low-frequency radio antenna, located in a radio quiet region of Western Australia, to detect a global absorption feature in the redshifted 21-cm hyperfine-structure signal of neutral hydrogen, seen against the cosmic microwave background (CMB). The signal is enabled by Lyman-$\alpha$ photons, produced in nebular emission around the first stars, interacting with primordial hydrogen. The detection of a signal centered at 78 MHz suggests ongoing star formation already at a time when the Universe was a mere 180 million years old. This tantalizing observation offers our earliest constraint on star formation to date, nicely complementing the lower-$z$ data around the epoch of reionization.

In this work, we introduce a newly developed Pop II star formation model in conjunction with our existing Pop III legacy model (Jaacks et al., 2018b), to study star formation and metal-enrichment in the pre-reionization Universe ($z \gtrsim 7$). This paper is organized as follows. In Section 4.2 we describe our numerical methodology, followed by the presentation of our results in Section 4.3. In Section 4.4, we discuss key predictions for the upcoming *JWST* mission, and compare our work with previous studies in Section 4.5. We end in Section 4.6 with our major conclusions.

Table 4.1: Simulation parameters used in this paper. The parameter $N_{\rm p}$ is the number of gas and dark matter particles; $m_{\rm DM}$ and $m_{\rm gas}$ are the particle masses of dark matter and gas; $\epsilon, h_{\rm sml}$ are the comoving gravitational softening length/hydrodynamical smoothing length (adaptive).

| Run | Box size (Mpc $h^{-1}$) | $N_{\rm p}$ (DM, Gas) | $m_{\rm DM}$ ($M_\odot$) | $m_{\rm gas}$ ($M_\odot$) | $\epsilon, h_{\rm sml}$ (kpc) | Pop III model | Pop II model |
|---|---|---|---|---|---|---|---|
| N512L4 | 4.0 | $2\times512^3$ | $4.31\times10^4$ | $9.64\times10^3$ | 0.45 | P3L | P2L |

## 4.2 Numerical Methodology

For this work, we utilize a highly customized version of the publicly available next generation hydrodynamics/N-body code GIZMO, which employs a Lagrangian meshless finite-mass (MFM) method for solving the fluid equations. GIZMO offers improved numerical accuracy and efficiency when compared to previous generations of smoothed particle hydrodynamics (SPH) and adaptive mesh refinement (AMR) codes (for a detailed method comparison, see Hopkins 2015). In this section, we will describe our choice of parameters for the simulation volume, as well as our customized sub-grid physics models, developed for this work.

Our simulation volume, designed to approximately replicate a single pointing with the *JWST* at redshift $z \sim 10$, has a (comoving) box size of $4h^{-1}$ Mpc, and contains $512^3$ particles in both gas and dark matter. We will refer to this simulation run as N512L4 throughout, and provide full details of the set-up in Table 4.1. Specifically, we adopt a $\Lambda$ cold dark matter ($\Lambda$CDM) cosmology, with parameters consistent with recent *Planck* results: $\Omega_m = 0.315$, $\Omega_\Lambda = 0.685$, $\Omega_b = 0.047$, $\sigma_8 = 0.829$, and $H_0 = 67.74$ km s$^{-1}$ Mpc$^{-1}$ (Planck Collaboration et al., 2016). Our initial conditions are generated at $z = 250$, using the MUSIC initial conditions

generator (Hahn & Abel, 2011).

Dark matter haloes are identified via a post processing 3D friends-of-friends (FOF) algorithm with a minimum particle requirement of 32 and a linking length of 0.15 times the inter-particle distance. Gas particles and their respective properties (mass, temperature, metallicity, density, position) are then associated with each dark matter halo by searching within its virial radius. Grouping and data extraction are aided by the *yt* (Turk et al., 2011) and *Caesar* (Thompson, 2014) software packages.

In the following subsections we will detail the custom sub-grid models which we have implemented into the public version of the GIZMO code base. This work includes new prescriptions for Pop II star formation and associated feedback, tracking metals created in Pop II and Pop III SN events independently, cooling via metal lines, and UV background heating. For details regarding previously implemented models, regarding Pop III star formation and feedback, primordial gas chemistry/cooling, Lyman-Werner (LW) photo-dissociation, and a stochastically sampled Pop III initial mass function (IMF), we refer the reader to Jaacks et al. (2018a,b).

### 4.2.1 Chemistry

Primordial chemical abundances are calculated and tracked for 12 species (H, $H^+$, $H^-$, $H_2$, $H_2{}^+$, He, $He^+$, $He^{2+}$, D, $D^+$ HD, $e^-$), using methods detailed in Bromm et al. (2002) and Johnson & Bromm (2006), in turn based on earlier work (Cen, 1992; Galli & Palla, 1998). As $H_2$ and hydrogen deuteride (HD) are the primary low-temperature coolants in primordial gas, it is critical to properly account for their formation and destruction. Therefore, we also include $H_2$ photo-dissociation,

as well as photo-detachment of $H^-$ and $H_2{}^+$, via an external LW background in our chemical network, together with a prescription for self-shielding. In principle, lithium hydride (LiH) is another molecular coolant in low-temperature primordial gas. However, Liu & Bromm (2018) have shown that it is unimportant in most environments, including those encountered in the assembly pathway of the first galaxies.

Heavy elements, which are the result of Pop III and Pop II star formation processes, are independently tracked in our simulation with passive metallicity scalar variables, and aggregated for each gas particle

$$Z_{\rm total} = Z_{\rm Pop\ II} + Z_{\rm Pop\ III}. \tag{4.1}$$

Individual elemental abundances are then assigned in a post-processing procedure, accounting for the yield differences between Pop II and Pop III SN explosions.

### 4.2.2 Cooling and heating

At each simulation time step, we evaluate the total cooling ($\Lambda$) and heating ($\Gamma$) rates for each particle in the simulation volume, to act as sink and source terms in the internal energy equation. In the following, we will describe the most important cooling and heating terms encountered in the formation of the first stars and galaxies.

#### 4.2.2.1 Cooling

In Figure 4.1, we present the rates for the primary low-temperature cooling channels included in our simulations. Primordial cooling ($\Lambda_{\rm pri}$), in the absence

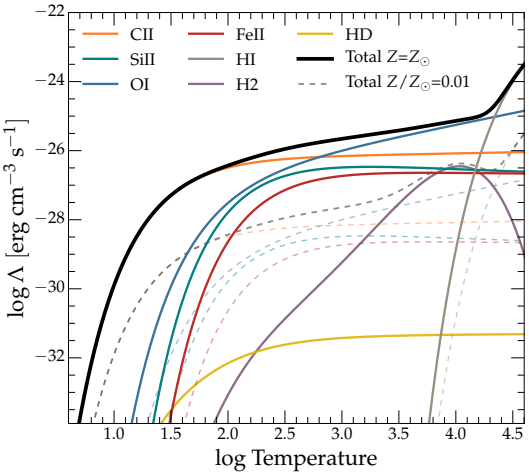


Figure 4.1: Primary low temperature ($T \lesssim 10^4$ K) cooling channels included in our simulations. Fine structure metal cooling from C II (orange), O I (blue), Si II (green), Fe II (red), following the detailed prescription presented in Maio et al. (2007). Molecular cooling with primordial contributions from $H_2$ (purple) and HD (yellow), as implemented in Galli & Palla (1998). Due to the large uncertainties in abundance patterns at high-$z$, we assume solar abundances according to Asplund et al. (2009), which scale with total metallicity. Solid lines represent $Z = Z_\odot$ and the dashed lines are calculated for $Z/Z_\odot = 0.01$. For both metallicities, the fractional abundances of $H_2$ and HD are set to $10^{-5}$ and $10^{-7}$, respectively, with an electron fraction of $10^{-3}$.

of metals, is dominated by $H_2$ and HD, whereas gas enriched by preceding star formation cools via fine-structure metal lines ($\Lambda_{\rm fine}$), dominated by C II, O I, Si II and Fe II. For simplicity, we assume that carbon, silicon, and iron are singly ionized by the soft UV (LW) background radiation field, and that oxygen is neutral due to its higher ionization potential (Bromm & Loeb, 2003b). Given the large uncertainties in abundance patterns at high-$z$, we adopt solar abundances according to Asplund et al. (2009), scaling with total metallicity. The solid lines represent rates in gas enriched to $Z = Z_{\odot}$, to provide a reference, and the dashed lines are calculated for $Z/Z_{\odot} = 0.01$, the typical metallicity in Pop II star forming clouds.

In our numerical implementation, cooling rates for C II and Si II are modeled as two-level systems utilizing

$$\Lambda_2 = n_2 A_{21} \Delta E_{21} \text{ erg s}^{-1}\text{cm}^{-3}, \tag{4.2}$$

where $n_2$ is the number density in the excited state, $A_{21}$ the Einstein coefficient for the spontaneous transition probability per unit time from levels $2 \rightarrow 1$, and $\Delta E_{21}$ the energy difference between the two levels. O I and Fe II are modeled as three-level systems with the contribution from each level summed

$$\Lambda_3 = \sum_{i \geq 2} \sum_{1 \leq j < i} n_i A_{ij} \Delta E_{ij} \text{ erg s}^{-1}\text{cm}^{-3}. \tag{4.3}$$

Our calculations follow closely details presented in Maio et al. (2007), who employ data for excitation rates and energy levels given in Hollenbach & McKee (1989) and Santoro & Shull (2006).

Our cooling channels for high temperature gas, $\Lambda_{\rm high}$, include atomic line cooling of H I and He II, collisional ionization and recombination cooling (H I, He I,

He II), as well as bremsstrahlung and inverse Compton cooling off the CMB (Cen, 1992; Greif et al., 2007). It is worth noting that, despite large abundances even at high redshift, we do not include CO molecular cooling. This is justified by the fact that cooling via rotational transitions of CO is largest at temperatures which are less than the redshift-dependent CMB floor, imposed in our simulations (see Omukai et al. 2010 for details regarding CO cooling).

#### 4.2.2.2 Heating

In addition to the LW background heating implemented in Jaacks et al. (2018b), we here include two new heating terms, due to an external ionizing UV background ($\Gamma_{\rm uvb}$) and to local photoelectric absorption ($\Gamma_{\rm pe}$).

We model the UV background (UVB) heating by including the term

$$\Gamma_{\rm uvb} = e^{-\tau}\zeta_{\rm ion}(z) n_{\rm HI} \langle\psi\rangle \, kT_c \text{ erg s}^{-1}\text{cm}^{-3}, \tag{4.4}$$

where $n_{\rm HI}$ is the number density of neutral hydrogen, and $\langle\psi\rangle \, kT_c$ the mean photon energy produced by a given stellar population. The color temperature is chosen to be consistent with a young stellar population dominated by O and B stars, $T_c = 20000$ K, corresponding to a mean value of $\langle\psi\rangle = 1.38$, obtained from Spitzer (1978). $\zeta_{\rm ion}(z)$ is the redshift dependent photo-ionization rate calculated in Faucher-Giguère et al. (2009a), and updated in 2011. For reference, $\zeta_{\rm ion}(z = 6) \approx 2.80 \times 10^{-13}$ s$^{-1}$. $\Gamma_{\rm uvb}$ is calculated at each time step and applied to all gas particles in the simulation volume.

Included in Equation 4.4 is the term $e^{-\tau}$, which allows us to take into account the ability for high density gas to self-shield against the UVB. Here, the effective

optical depth to ionizing photons is evaluated as

$$\tau \simeq \sigma_{\rm th} N_{\rm HI} \simeq \sigma_{\rm th} n_{\rm HI} L_{\rm char}, \tag{4.5}$$

where $\sigma_{\rm th} \simeq 6.3 \times 10^{-18}$ cm$^2$ is the hydrogen photo-ionization cross-section at the threshold (13.6 eV), $N_{\rm HI}$ the local neutral hydrogen column density, and $L_{\rm char}$ the characteristic size of the system. With this term, high-density star forming regions are able to shield against the effects of the UV background radiation. We note that it is standard numerical practice to estimate $L_{\rm char}$ using the hydrodynamical smoothing length of a gas particle (see Safranek-Shrader et al. 2012 for comparison of different methods to determine $L_{\rm char}$). However, very low-density gas particles in the IGM will have very large smoothing lengths, thus artificially boosting their shielding ability. Therefore, we fix $L_{\rm char} = 1$ kpc in order to avoid unphysically large IGM opacity.

To estimate the local photoelectric heating, $\Gamma_{\rm pe}$, due to stellar populations in our simulation volume, we consider each star particle as a simple stellar population, which we in turn regard as being spatially co-located. We thus model the combined emission from a stellar cluster as a point source, which is justified given that we do not resolve the size of a typical cluster. The volumetric photoelectric heating rate for each stellar population is then calculated as

$$\Gamma_{\rm pe}({\rm H} \rightarrow {\rm H}^+) = \alpha_B n_{\rm H}^2 \langle \psi \rangle \, kT_c \text{ erg s}^{-1}\text{cm}^{-3}, \tag{4.6}$$

where $\alpha_B = 2.59 \times 10^{-13}$ cm$^3$s$^{-1}$ is the case-B recombination rate coefficient, $n_{\rm H}$ the hydrogen number density, and $\langle \psi \rangle \, kT_c$ the mean photo-electron energy, released

in a typical interaction. This heating term is applied at each time step to particles which are found within the Strömgren radius of a Pop II star formation event, for the estimated lifetime of OB stars ($\sim$ 10 Myr). Note that the simulation timestep during this stage is $\sim 10^5$ yr, such that this effect is temporally well resolved. We will describe the approach to calculate the Strömgren radius, $R_{\rm Stromgren}$, in Section 4.2.5.

### 4.2.3 Pop III legacy star formation

Our Pop III "Legacy" (P3L) star formation model allows us to essentially "paint" fully formed SN blast waves onto our simulation boxes, centered on Pop III star forming regions, with physical properties calibrated to high-resolution simulations (e.g., Greif et al., 2007; Ritter et al., 2012), and to well-known analytic solutions (Sedov, 1959; Taylor, 1950). Each star formation event has a stellar population, which is randomly drawn from a given IMF, here taken to be approximately flat with a low-mass turn over at $\sim 5 M_{\odot}$. Our adopted IMF is consistent with results from high-resolution Pop III star formation simulations (e.g. Greif et al., 2011; Stacy & Bromm, 2013). This allows each star forming event to exhibit a unique feedback signature, in terms of explosion energy and nucleosynthetic yield, because stars with different masses end their lives differently, as type II SN, black hole, or pair-instability SN. The feedback bubble radius, metallicity, thermal energy, and ionization are directly calculated for each individual stellar population. Thereafter, the enriched gas is advected with the local hydrodynamical flow. This approach enables our star formation model to have both time and spatial dependence, and to independently trace the Pop III and Pop II origins of the aggregate metallicity. Full

Table 4.2: Key SSP characteristics. Stellar mass ($M_*$), total number of stars ($N_*$), total number of OB stars ($N_{\rm O+B}$), number of Type II SNe ($N_{\rm SNe}$), total mass of Type II SN progenitor stars ($M_{*,\rm SNe}$), and energy injected per SN ($E_{\rm SN}$). The values below have been calculated over a mass range of $0.08 - 100\ M_\odot$ for a Chabrier (2003) IMF.

| $\eta_*$ | $M_*$ $[M_\odot]$ | $N_*$ | $N_{\rm O+B}$ | $N_{\rm SNe}$ | $M_{*,\rm SNe}$ $[M_\odot]$ | $E_{\rm SN}$ [erg] |
|---|---|---|---|---|---|---|
| 0.10 | 964 | 1323 | 44 | 11 | 160 | $10^{51}$ |

details of the P3L model can be found in Jaacks et al. (2018b).

### 4.2.4 Pop II star formation

#### 4.2.4.1 Formation criteria

Pop II star formation is triggered when a preset threshold density, $n_{\rm th} = 100\ {\rm cm}^{-3}$, is reached for a gas particle with $T \leq 10^3$ K and $Z/Z_\odot > 10^{-5}$. The latter represents the critical metallicity, required to transition from Pop III star formation to Pop II (e.g. Safranek-Shrader et al., 2010; Schneider et al., 2012). This density is adopted due to the mass/spatial resolution limitations of our simulation volumes, which are only able to resolve pre-stellar clump scale objects, and not the individual star forming cores contained within. However, $n_{\rm th}$ is physically representative of densities which are observed in local star forming regions (e.g. Bergin & Tafalla, 2007; McKee & Ostriker, 2007), and sufficient to ensure that the cooling processes modeled here are efficient. Therefore, we are able to identify regions with the physical conditions necessary for runaway gravitational collapse.

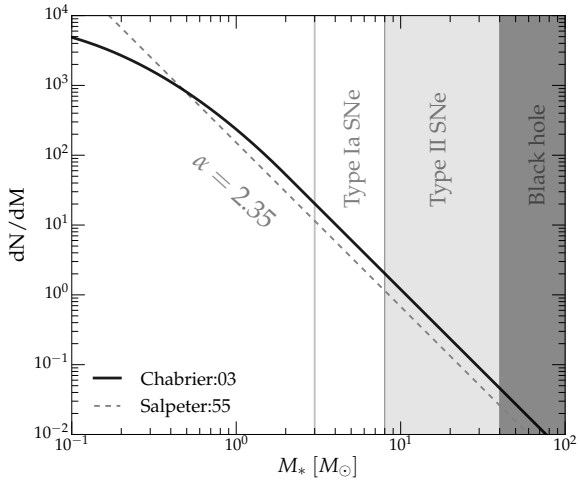


Figure 4.2: The Chabrier (2003) IMF adopted in this work, normalized to the total mass of our SSP. With the shaded regions, we indicate mass ranges associated with different stellar fates, i.e. type Ia SNe, type II SNe, direct-collapse black holes (Heger & Woosley, 2002). For comparison, we show a Salpeter (1955) IMF, normalized to the same total stellar mass (dashed line).

#### 4.2.4.2 Stellar population

Once a star formation event is triggered, a star particle is created with a stellar mass of $\eta_* \times m_{\rm gas} = 964 M_\odot$, where $\eta_* = 0.10$ is the star formation efficiency on the proto-stellar clump scale. In our prescription, the total stellar mass of a single formation event is fixed and has no local environmental dependency, e.g. on cloud mass or density. This precludes the formation of large star clusters. However, in a given halo, multiple dense clumps can arise that are not spatially co-located. Therefore, any given halo will be able to spawn a number of independent clusters. Once a gas particle qualifies for star formation, it exists as a point mass with gravitational interactions only, and will not be able to form any future stars.

We treat each star particle as a simple stellar population (SSP) with an IMF, which is taken to be Chabrier (2003)

$$\xi(m) = \frac{dn}{d\log m} \propto \begin{cases} m_0^{-x} \exp\left[-\frac{(\log m - \log m_c)^2}{2\sigma^2}\right], & m \leq m_0 \\ m^{-x}, & m > m_0 \end{cases} \tag{4.7}$$

with a slope of $x = 1.35$, $m_c = 0.18$, $m_0 = 2.0$ (both in units of solar mass), and $\sigma = 0.579$, over a mass range of $0.08 - 100\ M_\odot$ (Chabrier et al., 2014). For $m > m_0$, the Chabrier (2003) IMF is identical to the Salpeter (1955) one. The exponential cutoff at $m < m_0$ results in a stellar population, which is slightly less bottom heavy. In Figure 4.2, we show both the Chabrier (2003) and Salpeter (1955) IMF for comparison, whereas in Table 4.2, we present the relative number of stars for each evolutionary fate. The occurrence of each feedback event will determine the total energy and metal enrichment, returned to the surrounding medium.

### 4.2.5 Pop II legacy feedback

As with our P3L model, our primary concern is the metal enrichment legacy, resulting from Pop II star formation. Stellar feedback processes, such as the production of ionizing photons and metals, play a critical role in the regulation of ongoing star formation. Previous generations of numerical simulations have shown that without stellar feedback, the Pop II star formation rate density is unphysically large (e.g. Springel & Hernquist, 2003). Therefore, we include a multi-component stellar feedback prescription, where we consider both photo-electric heating from young stellar populations, as well as the thermal energy input and metal enrichment from Type II SNe. Due to the average delay time of $\sim$ 1 Gyr between progenitor formation to SN explosion (Maoz et al., 2012), we here do not consider Type Ia SNe, as we are only concerned with redshifts $z > 6$.

#### 4.2.5.1 Thermal energy input

As discussed in Section 4.2.2.2, $\Gamma_{\rm pe}$ is folded into our total heating term, $\Gamma_{\rm tot}$, and is applied to each gas particle which falls within the Strömgren radius associated with the stellar population

$$R_{\rm Stromgren} = \left( \frac{3 \dot{Q}_{\rm ion} N_{*,\rm O+B}}{4 \pi n_{\rm H_I}^2 \alpha_B} \right)^{1/3} \approx 240 \text{ pc}. \tag{4.8}$$

Here $\dot{Q}_{\rm ion} \approx 10^{49}$ s$^{-1}$ is the average number of ionizing photons produced per second and per OB star, $n_{\rm HI} = 1.0$ cm$^{-3}$ the neutral hydrogen number density in the interstellar medium (ISM) of a typical host halo, and $N_{*,\rm O+B}$ the number of OB stars producing ionizing photons. $\Gamma_{\rm pe}$ is applied to each particle initially found within

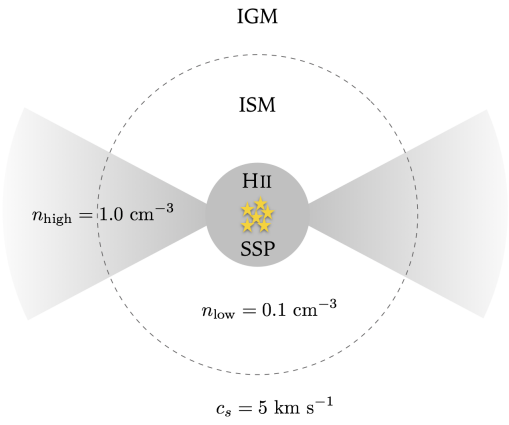


Figure 4.3: Conceptual illustration of a typical star forming region in our Pop II star formation model (not to scale). We indicate representative physical properties, assumed in each region for the post starburst, pre-SN phase.

$R_{\rm Stromgren}$, for the duration of the OB stars lifetime of $\sim$ 10 Myr.

#### 4.2.5.2 Metal enrichment

Once the photo-electric heating phase has ended, our feedback model "detonates" a cumulative Type II SN event, centered on the star particle, with a total energy of $E_{\rm tot,Pop\ II} = N_{\rm SNe} \times E_{\rm SN}$, where we assume instantaneous explosion of all contributing stars for simplicity (see Table 4.2 for values). The total SN energy is then used as input for an expanding shell calculation, similar to what was done for Pop III in Jaacks et al. (2018b). The result in each case is an expression for the final radius of a spherical shell, where the SN blast wave stops expanding. For this work, we modify our model assumptions slightly, to better reflect the physical environments in which Pop II stars form, such as higher mass host haloes and larger

central gas densities. More specifically, we take the surrounding ISM to be at a density of $n = 1.0$ cm$^{-3}$, as opposed to the previously adopted $n = 0.1$ cm$^{-3}$. Using this prescription, we find that $r_{\rm shell,high} \propto E^{0.35}_{\rm tot,Pop\ II} \approx 900$ pc. Further, due to the inhomogeneity of star forming clumps and the propensity for shells to seek out low density expansion channels (voids), we also calculate the shell radius for propagation through a low-density ISM region, where $n = 0.1$ cm$^{-3}$, resulting in $r_{\rm shell,low} \propto E^{0.38}_{\rm tot,Pop\ II} \approx 1.2$ kpc. In Figure 4.3, we illustrate the physical assumptions in our Pop II star formation model (not to scale). For the final enrichment radius, we adopt the approximate mean of the above values, $\bar{r}_{\rm shell} = 1.0$ kpc. Our parameters are consistent with recent high-resolution simulations of Pop II star forming galaxies at high redshifts (see fig. 8 in Jeon et al. 2015).

Metals are then equally distributed to each of the gas particles which are identified to be within $\bar{r}_{\rm shell}$, in accordance with $M_Z = M_{*,\rm SNe} \times y_Z \approx 16.0\ M_\odot$, for an effective Pop II SN yield of $y_Z = 0.10$ (Nomoto et al., 2013). The metals are subsequently allowed to simply advect with the local cosmic flow, as a component of the original gas particle. The total metallicity of each gas particle is continuously updated as the aggregate of the contribution of metals from Pop III and Pop II enrichment.

In addition, we also include a thermal component which heats the gas contained within $\bar{r}_{\rm final}$ to $T_i \approx T_{\rm IGM,Hot} \approx 10^4$ K at the end of the OB stars lifetime. This is done to approximate the thermal impact of the expanding shell at the time when it has reached its final, stalling radius. It should be noted that we do not impart energy in the form of a momentum kick to particles, as our resolution does not allow

us to properly follow the internal dynamics of the expanding shell. Our sub-grid prescriptions for both Pop III and Pop II are intended to reflect the long-term impact on the ISM and IGM, specifically the metal enrichment and boost in ionization, based on results from sophisticated, high-resolution ab initio simulations, which are able to self consistently follow the expansion of the radiation I-front, and the expanding SN blast wave through the ISM and into the IGM (e.g. Greif et al., 2007; Ritter et al., 2012; Jeon et al., 2014, 2015).

## 4.3 Results

### 4.3.1 Global properties

#### 4.3.1.1 Star formation rate density

As this work heavily depends on the star formation routines (P2L & P3L), we first examine the star formation rate density (SFRD), produced over cosmic time in our simulation. In Figure 4.4, we present the SFRD evolution for both Pop III and Pop II, covering the entire simulation volume (solid blue and orange lines, respectively). We witness the onset of Pop III star formation occurring at $z \sim 26$ (cosmic age $\sim$ 120 Myr), followed promptly by a burst of Pop II star formation at $z \sim 24$ (cosmic age $\sim$ 135 Myr). The delay time of $\sim$ 15 Myr between the initial Pop III activity and the subsequent round of Pop II star formation is consistent with results from ultra-high resolution simulations, where the recovery timescale for second-generation star formation is estimated Jeon et al. (2014). Pop II and Pop III stars form at a fairly comparable rate until $z \sim 15$, whereas afterwards Pop II star formation dominates by more than an order of magnitude over the remainder of

our simulation run.

It is interesting to note that the Pop III SFRD, when Pop II star formation is self-consistently included, deviates only minimally from our previous Pop III-only simulations in Jaacks et al. (2018b). This result suggests that Pop III star formation is largely decoupled from the effects of Pop II star formation and feedback, likely due to the sequence, where Pop III locally always precedes Pop II, and the biased environment of formation. In a way, Pop III acts as a 'pathfinder' for all subsequent star formation, and as long as there is available primordial gas at high density, the initial Pop III star formation will follow this near-universal path. We examine this question further in Section 4.3.4.

In the top panel, we compare our simulation results to observational estimates for the $z = 6 - 10$ SFRD, which is derived by integrating the observed UVLF and applying a conversion from luminosity to stellar mass density (e.g. Kennicutt, 1998; Madau & Dickinson, 2014). For direct comparison, we include observational constraints for the $z \lesssim 10$ Pop II SFRD (circles, diamonds; Finkelstein, 2016). The data points are derived from a "consensus" UVLF, which combines frontier observations from various published studies at $z \gtrsim 5$ (see Fig. 4.4 for references). Specifically, the circles are obtained by integrating the UVLF down to an observational limit of $M_{\rm UV} \sim -17$, whereas the diamonds are integrated down to a theoretical limit of $M_{\rm UV} \sim -13$. The latter aims to account for systems beyond current telescope capabilities. We find excellent agreement, within factors of $< 2$, at $z \lesssim 10$ with the empirically estimated total SFRD.

At redshifts $z = 10 - 15$, our results are consistent with extrapolations for the

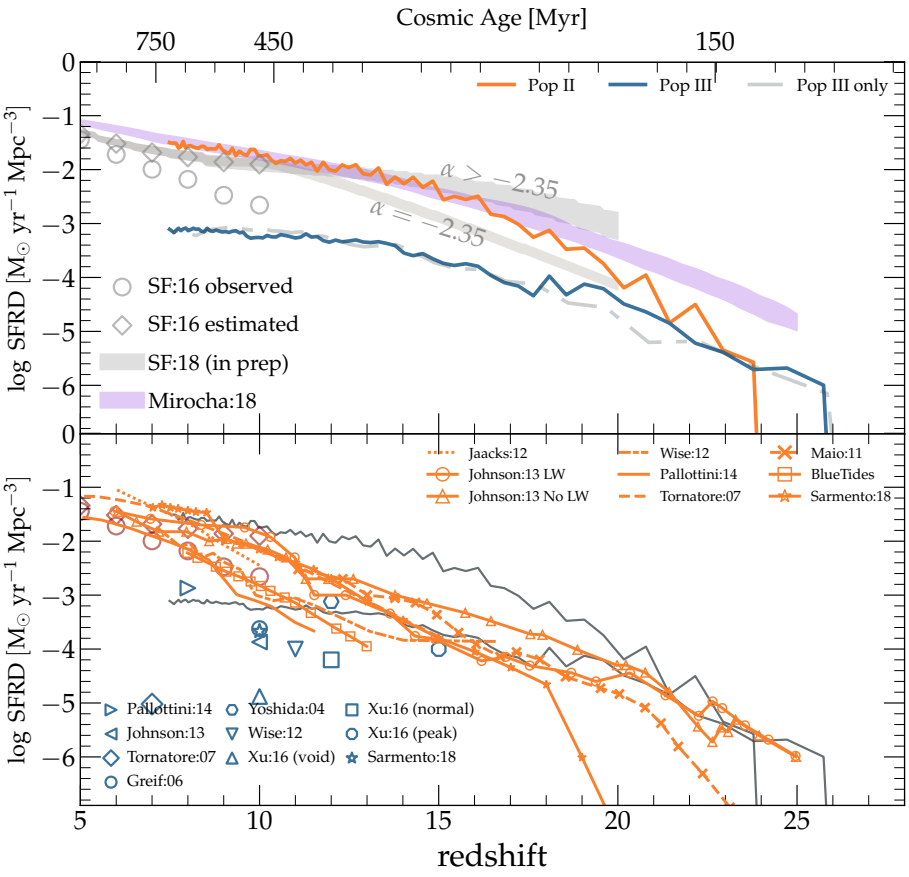


Figure 4.4: *Top:* Star formation rate density as a function of redshift, or cosmic age, for Pop II (solid orange) and Pop III (solid blue). For comparison, we reproduce the SFRD from our previous Pop III-only work (Jaacks et al., 2018b), where we modeled the radiative feedback from Pop II in an approximate way (gray dashed line). We also show observations for the Pop II SFRD, derived from the reference UVLF (diamonds, circles) discussed in Finkelstein (2016), which combines frontier observations at $z \geq 5$ from published studies (e.g. McLure et al., 2009, 2013; Oesch et al., 2013, 2014; Bowler et al., 2014; Schmidt et al., 2014; Bouwens et al., 2015, 2016; Finkelstein et al., 2015; McLeod et al., 2015). Furthermore, we include the recent model estimate from Mirocha & Furlanetto (2018), based on the 21cm absorption feature detected by EDGES (Bowman et al., 2018). *Bottom:* Comparison between this work, shown in dark gray solid lines, with previous numerical studies.

total SFRD, when the faint-end UVLF power-law slope is allowed to evolve to values steeper than $\alpha_{\rm UV} = -2.35$ at $z \gtrsim 9$. At even higher redshifts, our results are similarly consistent with the empirically-based models of Finkelstein et al. (2018, in prep.), which apply physically motivated star formation cut-offs to explore reionization scenarios with low UV escape fractions. Specifically, they explore scenarios where the slope continues to evolve at $z > 10$, and one where it remains fixed to its $z = 10$ value towards higher redshifts. At $z = 10 - 15$, our results are consistent with the evolving faint-end slope extrapolation, falling to slightly lower values beyond that, between the evolving and fixed faint-end slope empirical constraints. While considering an evolving UVLF is supported both by numerical works (Trenti et al., 2010; Jaacks et al., 2012a) and observations (Bouwens et al., 2012; Finkelstein et al., 2015), the true nature of the faint end of the UVLF at $z \gtrsim 10$ is highly uncertain. Therefore, we view the observation-based estimates as upper and lower bounds for the $z \gtrsim 10$ SFRD, with our model prediction ranging in between. We explore this further in Section 4.3.1.4, where we discuss our simulated UVLF.

Currently, direct observations of the $z > 10$ SFRD are lacking, until the next generation of ground- and space-based telescopes. Therefore, we must turn to previous numerical simulations to provide additional validation for our Legacy star formation approach. We have shown in Jaacks et al. (2018b) that our P3L model produces results which are consistent with a wide range of previous numerical estimates for the Pop III SFRD (e.g. Yoshida et al., 2004; Greif & Bromm, 2006; Tornatore et al., 2007; Wise et al., 2012; Johnson et al., 2013; Pallottini et al., 2014; Xu et al., 2016a). Results from these previous studies are shown as the blue symbols

in the bottom panel of Figure 4.4. Also shown in the bottom panel of Figure 4.4 is a direct comparison between our prediction for the Pop II SFRD (solid gray line) and those produced by other numerical experiments (various orange lines; Greif & Bromm, 2006; Tornatore et al., 2007; Maio et al., 2010; Jaacks et al., 2012a; Wise et al., 2012; Johnson et al., 2013; Pallottini et al., 2014; Feng et al., 2016).

We find that, while our simulations agree very well with the direct observations and observation-based estimates at $z = 6 - 10$, we deviate from most of the presented numerical works at $z \gtrsim 10$ by approximately an order of magnitude. We discuss the possible causes for this discrepancy in Section 4.5.1. A notable exception to the this trend are the results presented in Mirocha & Furlanetto (2018), who take a semi-analytical approach to galaxy evolution in order to determine if the observed galaxy population can account for the 21-cm EDGES observations. The purple shaded region in the top panel of Figure 4.4 represents the SFRD recovered from their model, with a star formation efficiency (SFE) calibrated to produce the observed $\sim 78$ MHz EDGES signal. Our simulated Pop II SFRD agrees very well with the Mirocha & Furlanetto (2018) model out to $z \sim 20$, where we begin to see a deviation to lower values. This may be due to the resolution limits in our simulation volume. We should caution that the EDGES results (Bowman et al., 2018), while extremely exciting, need to be confirmed by other instruments and subjected to further cross-checks in the future. Any conclusions must, therefore, be considered as preliminary.

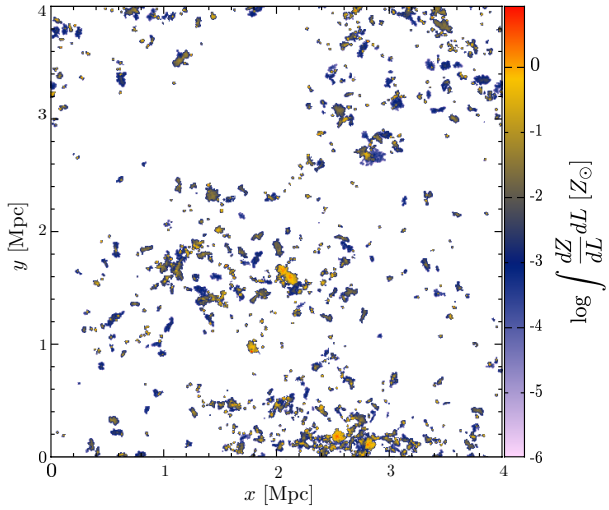


Figure 4.5: Metal-enrichment legacy in the early IGM. Shown is the total metallicity (Pop II+Pop III) at $z = 8$ for the entire simulation volume, in projection by integrating along the $z$-axis. All plots with projected metallicity, presented in this work, are rendered using SPLASH (Price, 2007). As can be seen, on the scale of the general IGM, a substantial fraction of the volume remains chemically pristine at the epoch of reionization.

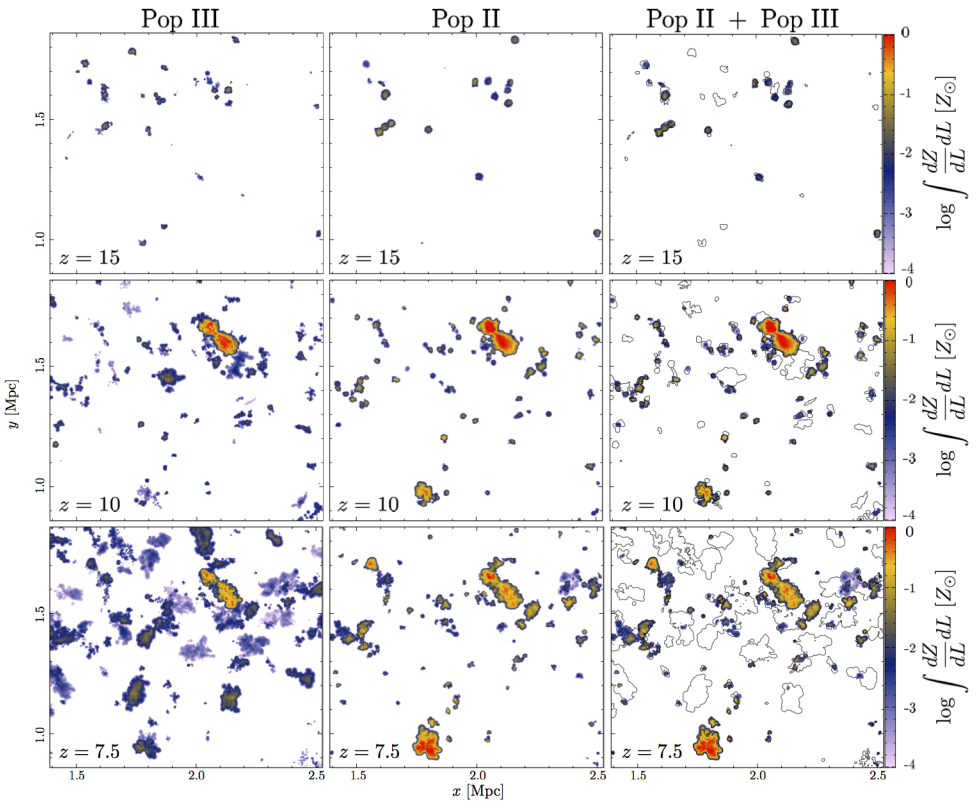


Figure 4.6: Metallicity projection plots for a subsection of the simulation volume for Pop III (left column), Pop II (center column), and Pop II+Pop III (right column), shown at $z = 15, 10, 7.5$ (top, center, bottom). In the right column, $Z_{\text{Pop II}}$ is shown by the color gradient, while $Z_{\text{Pop III}}$ is represented by a simple contour line. In this rendering, we are able to illustrate the regions, which are only enriched by Pop III metals, clearly distinguishing them from those, where both Pop II and Pop III contribute to the enrichment. The 'pathfinder' nature of Pop III enrichment is evident, as it sets the stage for the subsequent Pop II contribution.

#### 4.3.1.2 Multi-component enrichment

The primary legacy left behind by the formation and death of Pop III and second-generation Pop II stars is the enrichment with heavy chemical elements, which they impart to their environment. In Figure 4.5, we present the total metallicity, integrated along the $z$-axis for our entire simulation volume at $z = 7.5$. This rendition gives a qualitative understanding of the extent of metal enrichment, and the fraction of the cosmic volume impacted. In Section 4.3.2.2, we will quantify the volume filling fraction over cosmic time, thus providing a detailed analysis. However, it is clearly evident that towards the end of reionization, a substantial fraction of the IGM volume remains primordial, devoid of any metals. Those chemically pristine regions may provide 'relics' of the end of the cosmic dark ages, to be probed with extremely deep absorption spectroscopy in the local Universe.

In Figure 4.6, we present the same projected metallicity along the $z$-axis, but now for only a sub-section of our simulation volume at $z$=15, 10, 7.5 (top, bottom, middle rows, respectively). Furthermore, we separate the contributions from Pop III and Pop II metals into separate columns (left and center). Finally, in the right-most column, we combine the Pop II and Pop III metal enrichment, such that the latter is shown with the single black contour lines, and the former with the color gradient patches. With this presentation, we are able to qualitatively show both the increase in metallicity with cosmic time, and the independent contributions from each component to the total cosmic metallicity. Evidently, in this region of our simulation volume, there remain large regions, enriched by Pop III only at $z$=7.5. This result is consistent with the fact that the Pop III SFRD is still high at $z$=7.5, and

has yet to be terminated. This also suggests that Pop III star formation is continuing to occur in pristine haloes at these redshifts.

#### 4.3.1.3 Stellar mass function

Further cross-checks on our star formation routines can be obtained by comparing our simulated galaxy stellar mass function (SMF), the number density of star forming objects within a given stellar mass bin, to observations. In Figure 4.7, we compare our $z$=8, 10, 15 SMFs to the observed one at $z$=8, found in Song et al. (2016). We construct the SMF by grouping star particles into galaxies, using a simple FOF algorithm and evolving the mass of each stellar population contained within, in accordance with its age and IMF. We find excellent agreement with both the normalization and slope of the observed SMF for $M_* > 10^7\ M_\odot$. On the low-mass end, at $M_* < 10^5\ M_\odot$, our simulated SMF is flattening and deviates from the empirical extrapolation, shown by the dashed black line. Conspicuously, the flattening seen in our simulated SMF occurs at a galaxy stellar mass, which corresponds to a dark matter halo mass of $M_{\rm halo} \sim 10^8\ M_\odot$ at $z$=8. This is the mass scale where the transition between molecular dominated to atomic dominated cooling occurs (marked by the gray shaded region in Fig. 4.7). We discuss this interesting feature further in Section 4.5.2 below.

The simulated SMF exhibits significant evolution with increasing redshift, as the normalization decreases (orange circles compared to red diamonds). Because we do not capture the full range of masses in our meso-scale simulation box, it is unclear whether the SMF shape also evolves. In future work, we intend to increase

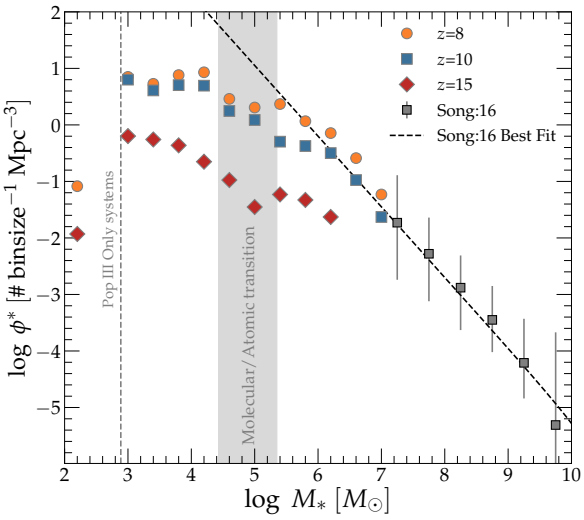


Figure 4.7: Simulated galaxy stellar mass functions (SMF), shown for $z = 8, 10, 15$ (orange circles, blue squares and red diamonds, respectively). The gray squares represent the observed SMF from Song et al. (2016). We find excellent agreement with observations at $M_* \gtrsim 10^5\ M_\odot$. However, for lower stellar masses we find a deviation (flattening) from the observed slope. This flattening coincides with the transition from molecular to atomic cooling haloes, at dark matter halo masses of $M_{\rm atomic} \approx 10^8\ ((1+z)/10)^{-3/2}\ M_\odot$ (vertical gray shaded region).

the volume of our simulation in order to reproduce larger-mass systems, at which time we will be able to better quantify the evolution of both the normalization and the low-mass slope. It should be noted that here, all galaxy stellar masses are calculated as the sum of Pop II and Pop III stars, taking into account the age and IMF of each star particle. For simplicity, the mass of stars which have evolved off the main sequence is no longer considered in the total mass of either component.

#### 4.3.1.4 UV Luminosity function

The final validation of our star formation model comes from the observed UV luminosity function (UVLF; the number of star forming objects within a given absolute magnitude bin per unit volume). While the SMF is straight forward to obtain from our simulations, it is more difficult to ascertain observationally. Conversely, the UVLF is closer to a direct observable, though it requires additional steps and assumptions to derive from simulations. We here discuss these assumptions, and compare our simulated UVLF to observations.

Producing a spectrum for a simulated star particle requires models for simple stellar populations (SSPs), over a range of stellar metallicities and age. For our Pop II SSP, we adopt the Schaerer (2002) low metallicity models, which have total stellar metallicities of $\log Z = -7.0, -5.0, -3.4, -3.0, -2.4, -2.1, -1.8$, ages in the range $10^4$ to $5\times10^7$ yr, and assume constant star formation histories. For each star particle, we interpolate between the nearest two metallicities and ages. The total spectrum for each galaxy is then taken to be the sum of the individual spectra from each contributing star particle. To estimate the nebular emission, we employ a fixed value for the escape fraction of $f_{\rm esc} = 0.10$ for all galaxies. This approximation is justified, given how incomplete our understanding of this key quantity still is.

A slightly different approach is taken for the construction of our Pop III spectra. To represent an individual Pop III star we assume a simple blackbody curve, which has been shown to be a good approximation for a primordial star in Bromm et al. (2001c). Our P3L star formation routine gives us a unique, randomly drawn stellar population for which each individual component mass is known. For

Table 4.3: Physical properties of high mass Pop III stars used to produce the blackbody spectra in our Pop III SSP (Schaerer, 2002).

| Type | Mass $[M_\odot]$ | T [K] | Radius $[R_\odot]$ | Lifetime [Myr] |
|---|---|---|---|---|
| PISN | 145 | 95720 | 4.80 | 1 |
| High | 90 | 93860 | 3.91 | 3 |
| Mid | 24 | 70800 | 1.85 | 10 |
| Low | 6 | 35000 | 1.10 | 50 |

simplicity we break down each Pop III star particle into four mass categories: PISN, High, Mid, Low. Each category is then assigned a temperature, radius and lifetime for which the blackbody spectrum and corresponding stellar luminosity is calculated. In Table 4.3, we summarize the values assumed for those physical properties in each mass category. Similar to the Pop II procedure, the total Pop III spectrum is composed of each contributing star. These spectra are then added to the Pop II component, thus synthesizing the combined spectrum for a given galaxy. Galaxy totals as well as the individual component spectra are then processed through a generic, top-hat filter, centered at 1500 Å with a total width of 100 Å to calculate the absolute UV magnitude. We here neglect any dust extinction, such that $E(B-V) = 0$, as both observations (McLure et al., 2011; Dunlop et al., 2012; Finkelstein et al., 2012b; Bouwens et al., 2014) and simulations (e.g. Wilkins et al., 2016; Barrow et al., 2017; Zackrisson et al., 2017; Jaacks et al., 2018a) suggest that, on average, low-mass galaxies at high-$z$ contain insufficient dust to significantly redden their spectra.

In Figure 4.8, we present the results of the above procedure in the form of

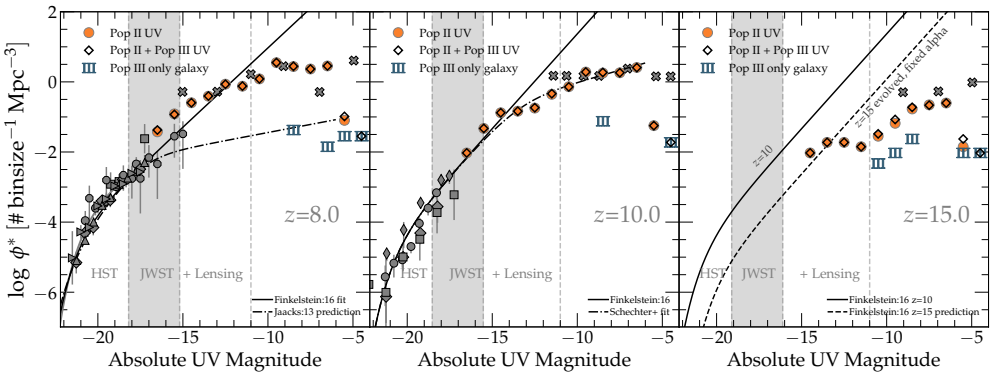


Figure 4.8: UV luminosity functions (UVLFs) for $z$=8, 10, 15 (left, center, right, respectively). In each panel, we show the UV luminosity produced by Pop II stars (orange circles) along with the UV luminosity produced by Pop II + Pop III stars (black diamonds). Sources with exclusively Pop III-generated UV luminosity are shown by the blue "III" symbols. The solid black line in each panel is the Schechter function fit (Schechter, 1976) from the 'reference' luminosity function found in Finkelstein (2016). We show excellent agreement with a wide range of observations at $z$=8 (e.g. Bouwens et al., 2011, 2014; McLure et al., 2013; Schenker et al., 2013; Schmidt et al., 2014; Atek et al., 2015; Finkelstein et al., 2015), and at $z$=10 (Oesch et al., 2013, 2018; Bouwens et al., 2015; McLeod et al., 2016). Currently, there are no direct observations for $z$=15. However we include a prediction for the $z$=15 UVLF by evolving the Schechter fit parameters ($M^*$, $\phi^*$), according to Finkelstein (2016) with a constant faint-end slope of $\alpha_{\rm UV} = -2.35$. We also include numerical studies from Wise et al. (2014) (gray 'x') and Jaacks et al. (2013) (dash-dotted black line). Throughout, the absolute UV magnitude was calculated with $E(B-V) = 0.0$. In each panel, we show the approximate absolute UV magnitude limits for *HST* and *JWST*, assuming limiting AB magnitudes of $m_{\rm AB,lim} \approx 29$ and 32, respectively.

the UVLF at $z = 8, 10, 15$ (left, center, right). In each panel, we show the UV luminosity produced by Pop II stars (orange circles), along with that produced by Pop II + Pop III stars (open black diamonds). Sources with exclusively Pop III UV luminosity are marked by the blue "III" symbols. The solid black line in each panel is the Schechter function fit (Schechter, 1976), for the 'reference' luminosity function from Finkelstein (2016). At $z = 8, 10$, we show good agreement with the faint end ($M_{\rm UV} \sim -17$) of the observationally inferred UVLF (see Fig. 4.8 for references to select observations), and excellent agreement with numerical work from Wise et al. (2014) at the extreme faint end ($M_{\rm UV} > -15$). Currently, there is no observational estimate for the $z = 15$ UVLF. Therefore, we reproduce the Schechter fit to the $z = 10$ observations to illustrate the relative evolution. We also include a prediction for the $z$=15 UVLF by evolving the Schechter fit parameters ($M^*$, $\phi^*$) according to Finkelstein (2016), with a fixed faint-end slope of $\alpha_{\rm UV} = -2.35$. While the agreement with our simulation results is encouraging, there remains much uncertainty regarding the evolution of the Schechter fit parameters. Future direct observations with *JWST* will allow for much better constraints at $z \gtrsim 10$.

An important aspect of this work is that we differentiate between the Pop II and Pop III contributions to the total galaxy spectra. This enables us to assess the separate contributions to the total galaxy luminosity. In each panel of Figure 4.8, we can see that Pop III only makes a minor contribution to the total UV luminosity (compare the black diamonds to the colored symbols), as the UVLF remains largely unchanged from the Pop II-only case. This finding resonates with the SFRD results (see Sec. 4.3.1.1), where Pop II dominates by more than a factor of 10 over Pop III

at these redshifts. We further quantify the relative contributions in Section 4.3.3 below.

We note a significant drop in the number density of galaxies with $M_{\rm UV} \gtrsim -10$, which approximately corresponds to $M_* \approx 10^4\ M_\odot$ and $M_{\rm halo} \approx 10^6\ M_\odot$. This deficit is in contrast to results found in Wise et al. (2014), who use adaptive mesh refinement (AMR; The Enzo Collaboration et al., 2014) simulations to study highly-resolved first galaxies, finding flat number densities down to lower magnitudes. This contrast is possibly the result of our dark matter halo mass resolution limit of $M_{\rm halo} \approx 10^6\ M_\odot$. However, our Pop III/II SSP masses ($M_{*,\rm III} \approx 500\ M_\odot$, $M_{*,\rm II} \approx 1000\ M_\odot$) are quite representative of typical, single star forming regions. Therefore, we can predict the magnitude where the UVLF is physically truncated, by calculating the UV magnitude for a single PopIII/II SSP, resulting in $M_{\rm UV,min,III} \sim -4.5$ and $M_{\rm UV,min,II} \sim -5.0$. Note that our Pop III SSP is made up of randomly drawn components. Therefore, it is possible that a given SSP could reach even lower luminosities in rare cases. We are also assuming a zero-age SSP for both Pop III and Pop II for the purpose of this idealized calculation.

Recently, there has been much discussion in the literature regarding a possible turnover, or flattening, in the UVLF (e.g. Jaacks et al., 2013; Wise et al., 2014; O'Shea et al., 2015; Livermore et al., 2017). In the left panel of Figure 4.8, we include the prediction from Jaacks et al. (2013), who adopt a broken power-law functional form for the faint-end of the UVLF. In the equivalent luminosity form,

this can be written as

$$\Phi(L) = \phi^* \left(\frac{L}{L^*}\right)^{\alpha_{\rm UV}} \exp\left(-\frac{L}{L^*}\right) \left[1 + \left(\frac{L}{L_{\rm turn}}\right)^{\beta_{\rm UV}}\right]^{-1}. \quad (4.9)$$

Here, $L_{\rm turn}$ constrains the turnover luminosity, and $\beta_{\rm UV}$ the subsequent flattening. When converted to its UV magnitude formulation, one has

$$\Phi(M) = 0.4 \ln 10 \phi^* 10^{0.4(M_{\rm UV}-M)(1+\alpha_{\rm UV})} \exp\left(-10^{0.4(M_{\rm UV}-M)}\right) \times \left[1 + 10^{(M_{\rm UV,turn}-M)\beta_{\rm UV}}\right]^{-1}. \quad (4.10)$$

However, based on the recent observation by Livermore et al. (2017), it appears that the Jaacks et al. (2013) prediction fails to properly represent either the observed data, or the simulation results presented here (see dash-dotted line in $z$=8 panel). This is likely due to a resolution in the earlier study which was insufficient to accurately model star formation in low mass molecular cooling haloes. In the center panel of Figure 4.8, we provide a fit to the combined data set (i.e. observations and this work), using Equation 4.10. We find that when we fix the standard Schechter parameters to the $z$=10 values found in Finkelstein (2016, $\log \phi^* = -4.13$, $M_{\rm UV} = -20.25$, $\alpha_{\rm UV} = -2.35$), the turnover seen in our simulated data can be constrained by $M_{\rm UV,turn} = -13.4 \pm 1.1$ and $\beta_{\rm UV} = -1.0 \pm 0.2$. We provide an extended discussion on this topic in Section 4.5.2.

### 4.3.2 Cosmic enrichment evolution

Above, we have explored the global properties of the galaxies and haloes found in our simulation volume. We now focus on how these properties evolve

over cosmic time. In particular, we will investigate the transition from a Pop III dominated Universe to one dominated by Pop II star formation. By investigating this transition, we lay the foundation for discussions regarding the overall legacy of Pop III star formation in the cosmological context, and the probability of observing the signature of the first stars (see Sec. 4.4).

#### 4.3.2.1 Mean metallicity

In Figure 4.9, we present the mean metallicity evolution for both enriched, bound systems (dark matter haloes) and all gas in our simulation volume. As seen in our previous work which focused only on enrichment via Pop III star formation (Jaacks et al., 2018b), bound systems (solid orange line) immediately jump above the critical metallicity line ($Z_{\rm crit} = 10^{-4}\ Z_{\odot}$) at the onset of star formation ($z \sim 26$). The total metallicity ($Z_{\rm Pop\ II} + Z_{\rm Pop\ III}$) for bound systems then rises slowly to a plateau value of $\log \left\langle Z_{\rm bound,total}/Z_{\odot} \right\rangle \approx -2.5$. This plateau suggests that a near-equilibrium between accretion of metal free gas and ongoing star formation has been established early on.

The mean total metallicity for all gas particles in our simulation volume (solid blue line) rises from an initial value of $\log \left\langle Z_{\rm all,total}/Z_{\odot} \right\rangle \approx -8$ at $z \sim 26$ to a value of $\log \left\langle Z_{\rm all,total}/Z_{\odot} \right\rangle \approx -3.5$ at $z = 8$. The mean metallicity in our simulation volume does not cross $Z_{\rm crit}$ until $z \sim 11$. This corresponds to the slight 'flattening', seen in the Pop III SFRD at $z \lesssim 13$ as the available reservoir of high-density, Pop III star forming gas is depleted. It is interesting to note that, while depleted, there remain substantial pockets of low-metallicity or metal-free gas to sustain ongoing

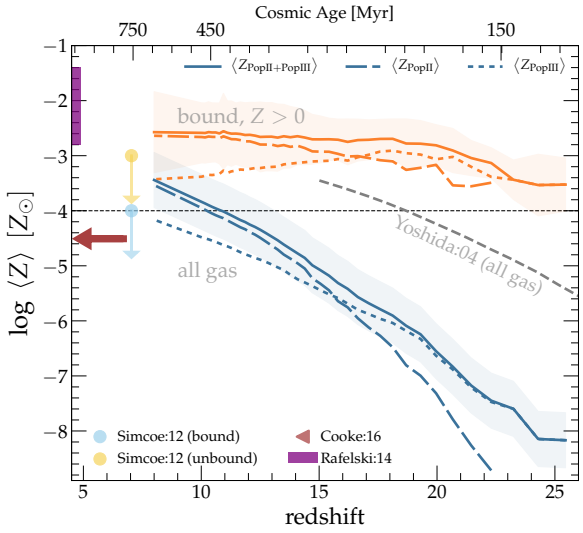


Figure 4.9: Mean metallicity evolution calculated for enriched, bound star forming regions (orange) and the entire simulation volume (blue). The dashed and dotted lines represent metals produced by Pop II and Pop III events, respectively, and the solid lines denote the total metallicity (i.e. Pop II + Pop III). We also present the predicted metallicity evolution from Yoshida et al. (2004), where *all* Pop III stars were considered to end their lives as PISN, thus imparting a maximum amount of metals back into their environment. Observations of high redshift DLA systems are indicated by the yellow/blue circles ($z = 7.04$; Simcoe et al., 2012), and the purple range ($z > 4.7$; Rafelski et al., 2014). The yellow circle is the estimate based on the assumption of an unbound medium, whereas the blue point is for a bound structure. Both are considered upper limits. The red arrow points to a lower redshift observation by Cooke et al. (2016).

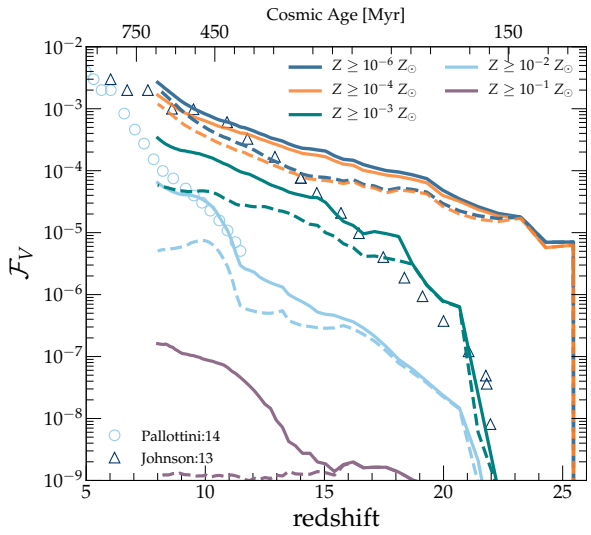


Figure 4.10: Metal volume filling fraction for both Pop II (solid lines), and Pop III (dashed lines) produced metals, shown for metallicity thresholds varying between $10^{-6} \leq Z/Z_\odot \leq 10^{-1}$. We also reproduce results from Pallottini et al. (2014) via the cyan open circles, which can be directly compared to the solid cyan line from our work. The blue open triangles shows results from Johnson et al. (2013) for the volume filling fraction of all metals.

Pop III star formation over the entire redshift range studied here. This suggests that, globally, Pop III star formation is not terminated by solely metal enrichment processes, in contrast to earlier predictions, such as in Yoshida et al. (2004).

#### 4.3.2.2 Metal volume filling fraction

To better quantify the spatial extent of both Pop II and Pop III metal enrichment, we in Figure 4.10 present volume filling fractions, $\mathcal{F}_V$, for a range of metallicity thresholds ($10^{-6} \leq Z/Z_\odot \leq 10^{-1}$), as a function of redshift. As expected, we see a trend of increasing metallicity for both Pop III (dashed lines) and

Pop II (solid lines) produced metals, with Pop II enrichment delayed by comparison. We also discern the same trend as in Figure 4.9 with Pop II enrichment catching up and surpassing Pop III between $z \approx 15 - 20$, depending on the threshold value. Evidently, the cosmic buildup of metallicity with higher thresholds is delayed until later redshifts. For example, there is no volume element with $Z > 10^{-1}\ Z_{\odot}$ until $z \approx 19$, whereas regions of the simulation are enriched beyond $Z > 10^{-6}\ Z_{\odot}$ immediately upon the onset of star formation at $z \approx 26$ . By the end of our simulation, at $z$=7.5, we find $\mathcal{F}_V \approx 10^{-3}$ for $Z \geq 10^{-6}\ Z_{\odot}$. This compares very favorably to results from Johnson et al. (2013), who find a similar value for all enrichment in their simulation volume. We deviate from these results at $z \gtrsim 15$ due to our higher SFRD at these redshifts. We find that only $\sim 10^{-4}$ of the simulation volume is enriched to beyond the critical metallicity for the Pop III to Pop II transition, $Z_{\rm crit} = 10^{-4}\ Z_{\odot}$ by $z = 7.5$, suggesting that there remains a large fraction of gas which has not been enriched by either population. This gas is potential fuel for ongoing Pop III star formation events. Our results are also consistent with Pallottini et al. (2014) for a threshold value of $Z \geq 10^{-2}\ Z_{\odot}$.

### 4.3.3 Pop III/II transition

We now wish to understand in more detail the relative contributions of Pop III and Pop II to star formation and key feedback processes, and in particular the epoch when the latter begins to dominate. For this purpose, we define the ratio

$$\mathcal{R}_{\rm III} \equiv \frac{\text{Pop III}}{\text{Pop III + Pop II}}. \tag{4.11}$$

In Figure 4.11, we show $\mathcal{R}_{\rm III}$ for three different star formation tracers: the SFRD, metals (bound, all), and ionizing emissivity. To guide the eye, we add the horizontal line, denoting the $\mathcal{R}_{\rm III} = 0.50$ value. From Figures 4.9 and 4.11, it can be seen that Pop III metal enrichment dominates at $z \gtrsim 17$ for bound systems (dashed line), and $z \gtrsim 15$ for all gas (solid line), after which Pop II takes over. By $z \approx 8$, only 15% (bound systems) and 20% (all gas) of the metals originated from Pop III sources. We also see that bound systems cross the $\mathcal{R}_{\rm III} = 0.50$ line earlier than the remainder of the volume. This is the case, because bound systems will be enriched first, as the hosts for star formation.

In Figures 4.4 and 4.11 it is apparent that Pop II star formation quickly follows the first burst of Pop III star formation (within $\sim$ 15 Myr). While the two star formation modes initially contribute at a similar level, by $z \sim 20$ Pop II clearly dominates (dotted line). More specifically, by $z = 7.5$, Pop III contributes $\sim$ 5% to the total SFRD, which is consistent with numerical results from Pallottini et al. (2014), who find a ratio of 8% at $z \sim 7$. However, since Pop III stars are, on average, more massive and thus hotter, they produce an order of magnitude more ionizing photons per stellar baryon (Bromm et al., 2001c). This is reflected in Pop III stars still contributing $\sim$ 20% of the ionizing photon budget at $z = 7.5$, which is overall consistent with previous studies, finding contributions of $\sim$ 10% (e.g. Ricotti & Ostriker, 2004; Greif & Bromm, 2006; Wise et al., 2012; Paardekooper et al., 2013). Again, our slightly higher value can be attributed to the slightly larger Pop III SFRD, predicted here.

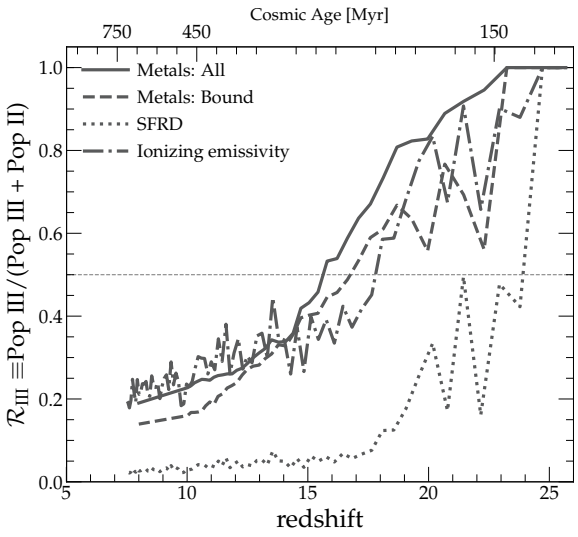


Figure 4.11: Ratio ($\mathcal{R}_{\rm III}$) of metals, SFRD and ionizing emissivity, contributed by Pop III to the total. The horizontal line represents the fiducial break-even level, $\mathcal{R}_{\rm III} = 50\%$. In terms of metal enrichment, it is evident that in bound star-forming structures (i.e. haloes), Pop III is overtaken by Pop II earlier ($z \sim 17$) than for gas in the diffuse IGM ($z \sim 15$). We also see that Pop II star formation quickly dominates over Pop III ($z \sim 20$). However, due to the more efficient ionizing photon production, Pop III star formation still contributes $\mathcal{R}_{\rm III} = 20\%$ to the total at $z \sim 7.5$.

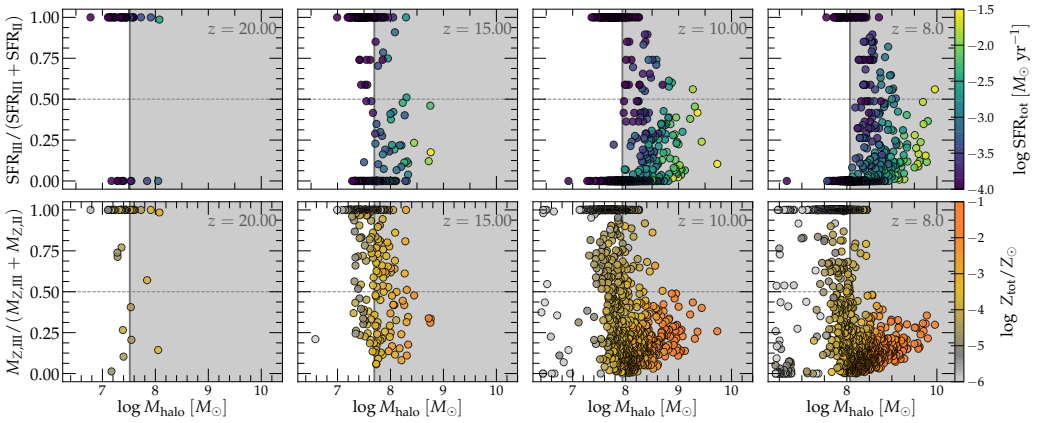


Figure 4.12: *Top row:* Ratio of Pop III SFR to total SFR (Pop II+Pop III), as a function of dark matter halo mass for $z = 20, 15, 10, 8$. The colors in each panel represents the total SFR for each dark matter halo. Pop II/III SFRs are determined by summing the stellar mass which has formed within the previous 50/10 Myr. The shorter Pop III time-average reflects the shorter lifetime of Pop III SSPs. *Bottom row:* Ratio of Pop III metal mass ($M_{Z,III}$) to total metal mass ($M_{Z,III}$ + $M_{Z,II}$), as a function of dark matter halo mass for the same redshifts as above. Now, the colors in each panel represent total metallicity ($Z_{tot}/Z_{\odot}$) in solar units for each dark matter halo. The gray shaded area in each panel represents the halo masses which are massive enough to enable atomic hydrogen cooling.

### 4.3.4 Where does Pop III occur?

Above, we have demonstrated that Pop III star formation, on average, is quickly dominated by Pop II (see Figs. 4.4 and 4.11). However, it is clear from Figure 4.4 that Pop III star formation has not been completely terminated by $z \sim 7.5$. This leads to the question: Is the ongoing Pop III star formation occurring in isolated, primordial haloes or pristine regions of Pop II dominated haloes? To answer this

question, we examine the ratio of star formation rates (SFRs), defined as

$$\mathcal{R}_{\rm SFR,III} \equiv \frac{\rm SFR_{III}}{\rm SFR_{III} + SFR_{II}}. \tag{4.12}$$

In the top row of Figure 4.12, we present the $\mathcal{R}_{\rm SFR,III}$ as a function of dark matter halo mass at $z = 20, 15, 10, 7.5$. We calculate the SFR by including stars formed within the past 50 Myr for Pop II, and 10 Myr for Pop III. Furthermore, the color bar represents the total SFR for each halo. The intuition here is that haloes which are experiencing Pop III-only star formation have $\mathcal{R}_{\rm SFR,III} = 1.0$, whereas haloes which are experiencing solely Pop II star formation will have $\mathcal{R}_{\rm SFR,III} = 0.0$. At early times, $z \sim 20$, low-mass haloes, $M_{\rm halo} \lesssim 10^{7.5}\ M_{\odot}$, are Pop III dominated, with only a few systems experiencing Pop II star formation. With increasing age of the Universe (left to right), we record a larger number of systems which become Pop II dominated. The Pop III/II transition is highly correlated with the transition in mass between molecular cooling and atomic cooling haloes (indicated by the gray shaded area). This in turn is consistent with the current star-formation paradigm, where Pop III stars form in low-mass minihaloes, thus planting the seed for subsequent Pop II stars.

Interestingly, the highest mass haloes in each panel exhibit $\mathcal{R}_{\rm SFR,III} < 1.0$, which indicates that both modes of star formation are ongoing. This is likely the result of pristine, neutral gas being accreted to within the virial radius of a halo that already contains Pop II stars, without experiencing significant mixing and shock heating. The survival of any pockets of in-falling primordial gas depends on the detailed physics of turbulence-driven mixing of heavy elements (e.g. Smith

et al., 2015; Sluder et al., 2016; Jeon et al., 2017; Sarmento et al., 2018). Those fine-grained hydrodynamical mixing processes are not resolved here, such that we may overestimate the occurrence of Pop III star formation inside the more massive host haloes. However, on the scale of a pre-stellar clump, which is resolved here, diffusion and mixing of metals may be too slow to penetrate deep enough into the clump to prevent Pop III star formation there (e.g. Cen & Riquelme, 2008). Clearly, this needs to be addressed further with future higher-resolution simulations.

This so-called cold-mode accretion (Birnboim & Dekel, 2003; Kereš et al., 2005; Dekel & Birnboim, 2006) then provides the fuel for ongoing Pop III star formation. Thus, there is a prominent class of haloes with a mixed star formation mode. We do, however, wish to assess the fraction of haloes, with $\mathrm{SFR_{III}} > 0.0$, which have experienced no Pop II star formation, defined as

$$\mathcal{F}_{\mathrm{III}} \equiv \frac{N(\mathcal{R}_{\mathrm{SFR,III}} = 1.0)}{N(\mathcal{R}_{\mathrm{SFR,III}} > 0.0)}. \tag{4.13}$$

This quantity can be interpreted as the fraction of isolated haloes, hosting Pop III-only, among all Pop III-forming haloes. As can be seen in Figure 4.13, there is a clear trend of lower $\mathcal{F}_{\mathrm{III}}$ with decreasing redshift. When our simulation ends at $z \simeq 7.5$, $\sim 20\%$ of Pop III star formation is occurring in isolated, Pop III-only, haloes, with ratios of 34%, 63%, and 96% at $z = 10, 15, 20$, respectively.

It is interesting to note that in the top panel of Figure 4.12, we see Pop II star formation occurring in dark matter haloes which are below the atomic cooling limit, indicating that these star forming regions are cooling via channels other than collisional excitation of atomic H I and He I. Cooling in haloes with $M_{\mathrm{halo}} < M_{\mathrm{atomic}}$

($T_{\rm vir} < 10^4$ K) must then be dominated by fine-structure transitions in metal enriched gas, in agreement with the results in Wise et al. (2014).

The bottom row of Figure 4.12 shows the ratio of mass in Pop III-generated metals to total metal-enriched mass, $\mathcal{R}_{\rm Z,III} \equiv {\rm M_{Z,III}}/({\rm M_{Z,III}} + {\rm M_{Z,II}})$, as a function of halo mass, where the color bar indicates the total metallicity of each halo. Here, the trend is very similar to the SFR one, which is expected since metals are the direct result of star formation events. By inspecting the color bar, we can also discern a clear trend of increasing metallicity with increasing halo mass, with the highest mass halo, $M_{\rm halo} \approx 10^{10}\ M_\odot$, containing $Z_{\rm tot} \approx 10^{-1}\ Z_\odot$. We also notice that at or near the molecular/atomic cooling mass, haloes are enriched to beyond the critical Pop III/II metallicity ($Z_{\rm crit} = 10^{-4}\ Z_\odot$).

In Figure 4.13, the orange line corresponds to the fraction of haloes which contain only Pop III-generated metals, compared to all enriched haloes. We calculate this quantity again with Equation 4.13, but now using metallicity instead of SFR. The offset between the blue and orange lines in Figure 4.13 is due to the fact that Pop III metals persist, whereas the Pop III SFR is temporary. Thus, a Pop II dominated halo will always contain Pop III metals, but may not experience ongoing Pop III star formation. Therefore, the denominator of Equation 4.13 will typically be larger in the case of metals, leading to a lower ratio.

## 4.4 Frontier observations

We find that, at each redshift studied, there are galaxies which exclusively consist of Pop III stars (see blue "III" symbols in Fig. 4.8). However, detecting

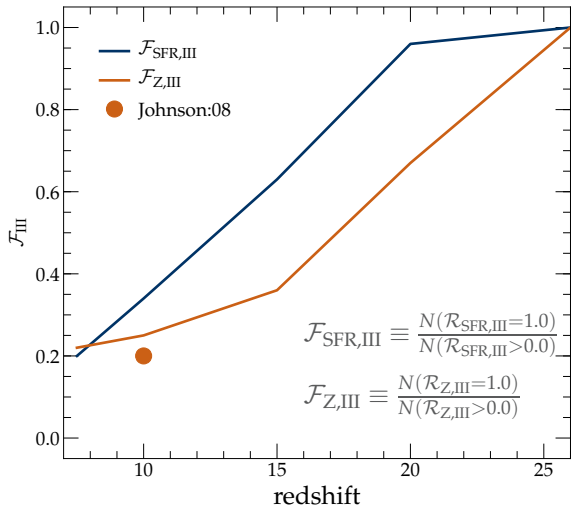


Figure 4.13: Fraction of Pop III-only systems. We show the fraction of Pop III star forming haloes which have yet to experience Pop II star formation, as a function of redshift (blue line). This is effectively the fraction of isolated haloes hosting Pop III, as opposed to mixed-population ones. Similarly, we show the fraction of haloes which only contain Pop III-generated metals, compared to all enriched systems (orange line). Both curves are extracted from the data presented in Fig. 4.12. We include an estimate at $z \sim 10$, provided in the numerical work by Johnson et al. (2008) via the orange circle.

these 'pure' Pop III galaxies is beyond the capabilities of *JWST*, even when lensing is utilized, allowing us to reach $M_{\rm UV} \lesssim -11$). It is thus unlikely that upcoming surveys will be able to directly detect such Pop III-only, or Pop III-dominated, galaxies. There are, however, several empirical avenues to indirectly probe these systems, among them are absorption studies of the diffuse IGM, and searches for transient events at high-$z$, such as SNe and gamma-ray bursts (GRBs).

### 4.4.1 Probing the IGM metallicity

The search for systems which have been enriched only with Pop III metals has intensified in recent years. Prime examples are the vigorously debated luminous CR7 Lyman-$\alpha$ source, which was initially thought to exhibit ultra-low metallicity (Sobral et al., 2015), and the Simcoe et al. (2012) damped Lyman-$\alpha$ (DLA) system. It is useful to utilize our simulations to examine the metal enrichment as a function of environment, to determine the observability of ultra-low or zero metallicity systems at $z \gtrsim 7$.

In Figure 4.14, we show the total gas metallicity as a function of number density, for all gas particles in our simulation volume. The color represents the ratio of Pop III metals contained in each hexagonal pixel. We also artificially place gas with zero metallicity at $\log Z/Z_{\odot} = -6$, and indicate particle frequency with shades from black (highest) to white (lowest). As one would expect, the region above our star formation threshold of $n_{\rm th} = 100$ cm$^{-3}$, and above $Z_{\rm crit}$ (dashed line), shows a mix of Pop II + Pop III metal enrichment, with higher metallicities being dominated by Pop II metals. Conversely, below $Z_{\rm crit}$, Pop III metals dominate. It is also clear

that Pop III metals permeate throughout all of the regions indicated (IGM, halo, star forming). This renders identifying regions where observations could look for systems that are exclusively enriched by Pop III particularly challenging, as Pop III metals from these systems span the entire range presented here.

It is also useful to identify regions which have experienced zero enrichment (primordial gas). In Section 4.3.2.2, we found that only $\sim 10^{-3}$ of our simulation volume has been enriched by $z = 7.5$. As indicated by the black-gray shaded region in Figure 4.14, the vast majority of the primordial gas is contained in the low-density IGM ($n < 10^{-2}$ cm$^{-3}$), with a mean density of $\log \langle n_{\rm pri} \rangle \simeq -3.2$ cm$^{-3}$ (cyan diamond in Fig. 4.14). While primordial gas exists over the entire dynamic range of our simulated volume, it will be difficult to detect when contained within dark matter haloes, as most lines-of-sight will also contain metal-enriched gas. Therefore, the best opportunity to detect primordial gas with absorption spectroscopy may be at the interface between the diffuse IGM and filamentary structures of the cosmic web. Future observations with the upcoming suite of extremely large, 30-40m class telescopes on the ground may be able to push existing limits on the Lyman-$\alpha$ forest into the regime of the chemically pristine IGM. Note that the number density of each particle is directly tied to the hydrodynamical smoothing length of the particle. While GIZMO incorporates an adaptive hydrodynamical smoothing length, it imposes a maximum of 0.45 kpc (comoving), which is why we have a buildup of gas at $n \approx 10^{-4}$ cm$^{-3}$.

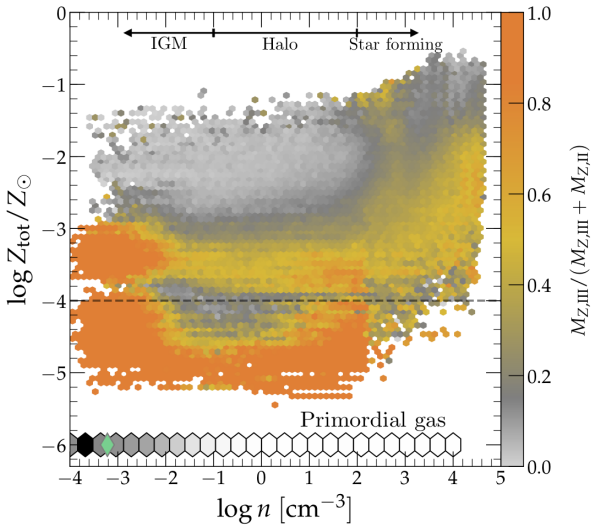


Figure 4.14: Metallicity as a function of number density for each gas particle in our simulation volume. The color bar represents the mass fraction of Pop III metals contained in each particle. The dashed horizontal line indicates the critical metallicity for the Pop III to Pop II transition ($Z_{\rm crit} = 10^{-4}\ Z_\odot$). The approximate delineations between regions within our volume (IGM, halo, and star forming) are indicated at the top of the figure. In order to include gas which has yet to be enriched by either Pop II or Pop III metals we artificially place this gas at $\log Z/Z_\odot = -6$, where the black to gray shading indicates particle frequency, with black being the highest. The cyan diamond indicates the median number density of the primordial gas ($\log n \simeq -3.2$ cm$^{-3}$).

### 4.4.2 Transient event rate

Transient events, such as SNe and GRBs, may be our best mechanism to probe low-density gas at $z \gtrsim 10$, as they act as background flashlights to illuminate foreground systems (Wang et al., 2012). Therefore, estimating the production rate for these events may prove useful for future deep-field surveys. To first order, the rates for PISNe and the less-extreme core-collapse SNe (CCSNe) can be calculated by leveraging our Pop II/III SFRDs, together with information about their respective IMFs, as (e.g. Hummel et al., 2012)

$$\begin{aligned} \frac{dN}{dt_{\rm obs} dz d\Omega} &= \zeta_{\rm IMF} \frac{dN_*}{dt_{\rm obs} dV} \frac{dV}{dz d\Omega} \\ &= \zeta_{\rm IMF} \frac{1}{(1+z)} \frac{dN_*}{dt_{\rm em} dV} r^2 \frac{dr}{dz}. \end{aligned} \tag{4.14}$$

Here, $dN_*/dt_{\rm em}dV$ is the star formation rate per comoving volume element (SFRD), $\zeta_{\rm IMF}$ accounts for the fraction of the IMF which falls within the appropriate mass range for each transient, and $r = r(z)$ is the comoving distance to redshift $z$. The result is the number of events per unit time per unit redshift per solid angle.

In the top panel of Figure 4.15, we present the results for Pop III CCSN/PISN events (blue lines), and for Pop II CCSNe (orange line), where the rate has been converted from per solid angle to per 10 arcmin$^2$. The conversion is done to represent a *JWST* NIRCam pointing field of view. Our results imply that a future *JWST* survey, such as the 100 arcmin$^2$ CEERS program (Finkelstein et al., 2017), can expect event rates of $\sim 1$ yr$^{-1}$ for Pop III CCSNe and $\sim 0.1$ yr$^{-1}$ for Pop III PISNe, though multi-epoch follow-up would be needed to confirm any detection. These results are roughly consistent with previous studies (e.g. Wise & Abel, 2005;

Wiersma et al., 2009; Hummel et al., 2012). Differences are directly related to the underlying SFRDs, assumed in each study.

To estimate the GRB rate, we carry out a similar procedure as above, with the exception that $\zeta_{\rm IMF}$ is replaced with $\zeta_{\rm GRB}$, the GRB formation efficiency per unit mass, $\zeta_{\rm GRB} = 2\times10^{-9}$. Furthermore, we now integrate over the entire sky ($4\pi$), thus removing the solid angle dependence, accounting for the fact that GRB detectors are not limited to observing a single patch of sky. From our Pop II/III SFRDs, we estimate that a 'perfect', all-sky instrument would find $\sim 0.1$ GRBs originating from Pop III per year.

## 4.5 Discussion of key topics

### 4.5.1 Comparison with previous studies

In Section 4.3.1.1, we made a detailed comparison between our simulated Pop II SFRD and that from previous numerical works (see bottom panel of Fig. 4.4). It is evident that our simulation is producing far more stars ($\sim$ 10 times in some cases) at $z \gtrsim 10$. All numerical simulations include sophisticated models for star formation, cooling and feedback, with complex dependencies on one another. Therefore, a single simple cause for the deviation between our $z > 10$ Pop II SFRD and previous numerical predictions may not exist. In light of this, we discuss several scenarios which could contribute to the discrepancy.

*Scenario #1:* Our star formation routines (P3L, P2L) are simply producing too many stars. This could be the case if our star formation efficiencies are too high ($\eta_{*,\rm III} = 0.05$, $\eta_{*,\rm II} = 0.10$). For the case of Pop II, direct observational estimates

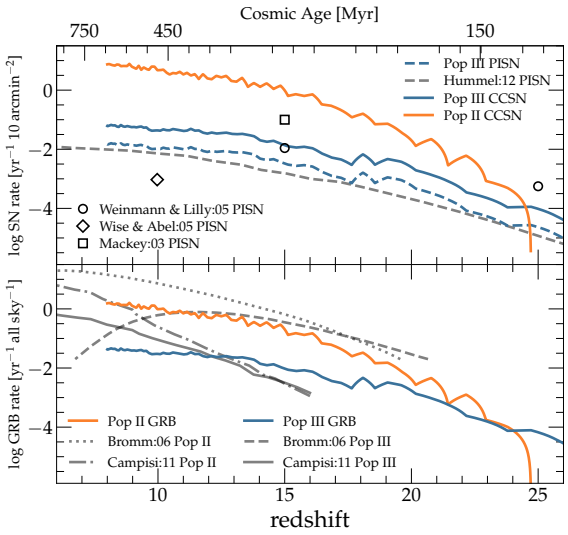


Figure 4.15: Rate of transient events for both Pop II (orange lines) and Pop III (blue lines). *Top:* SN rates, both for CCSNe and PISNe. Note that we employ units of events per year per 10 arcmin$^2$, the approximate field of view of a *JWST* pointing. For comparison to our PISN rate, we include estimates from Mackey et al. (2003); Weinmann & Lilly (2005); Wise & Abel (2005); and Hummel et al. (2012). *Bottom:* All-sky GRB rates per year. We here assume an ideal instrument with 'perfect' sensitivity. For reference, we reproduce GRB rate estimates from Bromm & Loeb (2006); Campisi et al. (2011). As can be seen, Pop III GRBs are rare, and would require multi-year survey campaigns.

of these values at $z > 6$ are currently not available, and thus we must rely on observations of local analogs for our simulated star forming regions. The most appropriate of which would be giant molecular cloud (GMC) scale objects, with masses in the range $10^3 \lesssim M/M_\odot \lesssim 10^5$. GMCs have estimated star formation efficiencies in the range $\eta_{*,\mathrm{II}} \approx 0.03 - 0.24$ (e.g. Kennicutt, 1998; Krumholz & Tan, 2007; Evans et al., 2009; Murray, 2011), placing our value of $\eta_{*,\mathrm{II}} = 0.10$ well within the observed range.

Potential overproduction of stars via our P3L model could indirectly lead to a corresponding overestimate for Pop II stars, due to an unphysically rapid metal enrichment of the primordial ISM. Admittedly, the Pop III star formation efficiency is far more uncertain, as there are no direct observations or local analogs. Therefore, we rely on high-resolution, ab initio simulations of metal-free star forming regions to determine the mass of a single Pop III stellar group, $M_{*,\mathrm{III}} \approx 500 M_\odot$, which is then distributed according to the IMF (e.g. Greif et al., 2011; Hirano et al., 2014; Stacy et al., 2016). Our efficiency factor of $\eta_{*,\mathrm{III}} = 0.05$ is a consequence of this numerical calibration.

Our simulation could also overproduce stars if the stellar feedback prescription is too weak. Such feedback has long been recognized as a primary mechanism through which galaxies regulate their star formation (e.g. White & Rees, 1978; Dekel & Silk, 1986; White & Frenk, 1991; Hopkins et al., 2012; Somerville & Davé, 2015). As the star formation life cycle progresses, the surrounding ISM receives large amounts of energy via stellar winds, radiation and SN shock fronts, removing entirely, or at least partially, gas which otherwise could have collapsed

to form stars. Our P2L and P3L models are focused on the long-term legacy, left behind by early star formation, and they lack sufficient resolution to directly model feedback processes, such as radiation pressure, or expanding SN shock fronts. However, our legacy models replicate key physical aspects of those processes, in that gas is heated, ionized, and the resulting overpressure moves gas from high-density star forming clouds to low-density ISM/IGM regions.

While we feel justified in the adaptation of the physical parameters via observation and high resolution numerical experiments, the primary support for our models derives from the agreement with observations of $z \gtrsim 6$ galaxies, in particular regarding the total predicted SFRD (Fig. 4.4), SMF (Fig. 4.7) and UVLF (Fig. 4.8). Were our simulations dramatically overproducing stars, we would expect to see a strong departure from extrapolations of these robust observations. It is also worth noting that our work is consistent with the $z > 6$ SFRD derived from GRB detections (see Robertson & Ellis, 2012; Wang, 2013).

*Scenario #2:* Simulation resolution dictates the dynamic range which can be produced within a given volume. For example, large cosmological volumes with box sizes $\sim 100h^{-1}$ Mpc, will contain objects at the massive/bright end of the SMF/UVLF, whereas volumes with sizes in the $10 - 50h^{-1}$ Mpc range will reproduce the low mass/faint-end of those functions. The volume chosen for this work, with length $4h^{-1}$ Mpc, is specifically chosen to replicate a *JWST* deep-field pointing, with sufficient resolution elements to allow for pre-stellar clumps to be resolved. As a consequence, we are exploring the extreme low mass/faint-end of the SMF/UVLF, which is beyond the capabilities of *HST*. With this in mind, we should

not be surprised if our SFRD did not match with simulations designed to reproduce a different dynamic range in halo mass or designed to study a different epoch in cosmic evolution.

The situation is different for the FiBY simulation, analyzed in Johnson et al. (2013), which has the same $4h^{-1}$ Mpc box size, with more resolution elements ($684^3$), giving it slightly better mass and spatial resolution. Consequently, we are exploring a similar dynamic mass range. Yet, we are producing significantly more Pop II stars over the redshift range $z = 10 - 20$. We suspect that a stronger, 'local' Lyman-Werner flux in the FiBY simulation could be the reason for the lower SFRD, via enhanced photo-dissociation of the low-temperature molecular coolants, $H_2$ and HD. We intend to explore this further in future work.

*Scenario #3:* Outdated empirical calibration. With the addition of the WFC3 instrument on *HST*, the past decade has seen a dramatic increase in the number of $z \gtrsim 6$ sources detected (e.g. Bouwens et al., 2010a, 2011; Finkelstein et al., 2010, 2012a). The utilization of gravitational lensing in the Hubble Frontier Fields (HFF) program has extended our sample to even higher numbers of galaxies with increasingly lower luminosities (e.g. Atek et al., 2015; Ishigaki et al., 2015; Livermore et al., 2017). The net result of these cutting-edge observations has been the steady increase in both the estimate for the steepness of the UVLF faint-end slope, $\alpha_{\rm UV}$ =-1.7 to $\alpha_{\rm UV} \approx -2.0$ at $z$=6 (e.g. Bouwens et al., 2006, 2017; Finkelstein, 2016; Livermore et al., 2017), and for the total cosmic SFRD. The flip-side to this progress is that it makes for a moving target for numerical experiments, which rely on these observations to calibrate the parameters in sub-grid models. The tendency

to 'tune' model parameters to reproduce observations can ultimately lead to under- or over-prediction of star formation activity, if the observed estimates are revised.

### 4.5.2 To turn over or not to turn over

Additional factors to consider, when integrating an observed UVLF to produce a luminosity density or SFRD, are the limits of integration, and any deviation from the faint-end power-law slope, such as a turnover or flattening. Basic physical considerations suggest that the faint-end of the UVLF cannot continue indefinitely towards ever fainter objects. At some point, it must turn over, or truncate. The existence and properties of this turnover have been the subject of a vigorous debate (e.g. Trenti et al., 2012; Jaacks et al., 2013; Boylan-Kolchin et al., 2015; Livermore et al., 2017). Previous numerical studies have predicted a turnover/flattening for $M_{\rm UV} \gtrsim -17$ at $z > 6$ (Jaacks et al., 2013; Wise et al., 2014; O'Shea et al., 2015). Observations of local dwarf galaxies suggest that a constant faint-end slope at $z \simeq 7$ of $\alpha_{\rm UV} = -2.0$, beyond $M_{\rm UV} \approx -13$, would result in $\sim 100$ times the number of dwarf galaxies than currently observed (Boylan-Kolchin et al., 2015). However, HFF observations from Livermore et al. (2017) find no evidence for the faint-end slope deviating from the power-law predictions, at $z = 6, 7, 8$, respectively, within the limiting magnitudes of $M_{\rm UV} = -12.5, -13.5, -15$ (other analyses of this data agree that no turnover is present at $M_{\rm UV} < -15$; Atek et al., 2015; Yue et al., 2016; Bouwens et al., 2017).

In this work, we again find evidence for a flattening of the SMF and UVLF at $z = 8, 10, 15$ with $M_{\rm UV,turn} \approx -12, -13.5, -14$, respectively. These results are in

excellent agreement with those presented in Wise et al. (2014), and with results in Boylan-Kolchin et al. (2015), who suggest that a flattening for $M_{\rm UV} \approx -13$ at $z$=7, with a subsequent slope of $\beta_{\rm UV} = -1.2$, is required to account for observations of local dwarfs. The UVLF turnover point, found here, lies just beyond the limiting magnitudes of Livermore et al. (2017). This suggests that *JWST*, in conjunction with a lensing program similar to the HFF, could rule out or validate this key result. Furthermore, we find that this flattening corresponds well with the mass transition between atomic and molecular cooling haloes (see gray shaded region in the SMF, Fig. 4.7). This result resonates with the idea that atomic cooling haloes support higher star formation efficiencies, due to their increased number of cooling channels (atomic, molecular and metals; Bromm et al., 2001a; Bromm & Loeb, 2003a; Santoro & Shull, 2006; Maio et al., 2010; Omukai et al., 2010), and their ability to cool even in the presence of strong external radiation fields (ionizing UV, soft LW; Maio et al., 2007; Wise & Abel, 2007; Safranek-Shrader et al., 2010). Therefore, we suggest that the star formation efficiency differential between atomic and molecular cooling haloes is the root cause of the flattening seen in this work.

In the presence of strong UV background radiation, the accretion of IGM gas onto atomic cooling haloes can be suppressed, as any IGM gas heated to above the viral temperature of the halo will not accrete, resulting in lower star formation rates. Previous simulations have explored this Jeans-filtering process, and shown that it can take effect at halo masses above the atomic cooling limit, $M_{\rm halo} \lesssim 10^9 - 10 M_\odot$ (e.g. Iliev et al., 2007; Mesinger & Dijkstra, 2008; Okamoto et al., 2008), and has been suggested as a possible origin for a turnover in the UVLF. To explore this possibility,

we consider the relationship between stellar mass and halo mass (SMHM). In Figure 4.16, we show the SMHM relation for $z = 8, 10, 15$, along with vertical lines denoting the atomic cooling mass for each redshift. If our simulated haloes were experiencing significant photo-suppression from UV background photons, we would expect to see a deviation in the slope of this relation at some mass above the atomic cooling limit. To the contrary, such deviation is not seen, although there is significant scatter for masses larger than the atomic cooling threshold. However, this is expected as in our simulation volume the UV background flux is still ramping up at $z$=8, with only $< 50\%$ of the IGM ionized. Future work, continuing these simulations to lower redshift, can better assess the impact of photo-suppression on the turnover of the luminosity function at $z \lesssim 8$. It is worth noting that the absence of photo-suppression at these redshifts and halo masses is consistent with recent semi-analytic results presented in Yung et al. (2018).

A possible turnover in the UVLF would be reflected in estimates of the cosmic SFRD. To illustrate this effect, in Figure 4.17 we present the results from a numerical exercise, where we compare the SFRD at $z \simeq 10$, derived from a UVLF both with and without a turnover, employing the conversion from luminosity to stellar mass density in Madau & Dickinson (2014). The top panel shows the SFRD, derived with Schechter-fit parameters found in Finkelstein (2016), compared with values derived from the Schechter+ formulation (see Equ. 4.9; Jaacks et al., 2013). Note that we fix the standard UVLF Schechter parameters, in an effort to isolate the impact of including a broken power-law faint end ($\log \phi^* = -4.13$, $M_{\rm UV} = -20.25$, $\alpha_{\rm UV} = -2.35$). From this exercise, it is clear that, depending on the

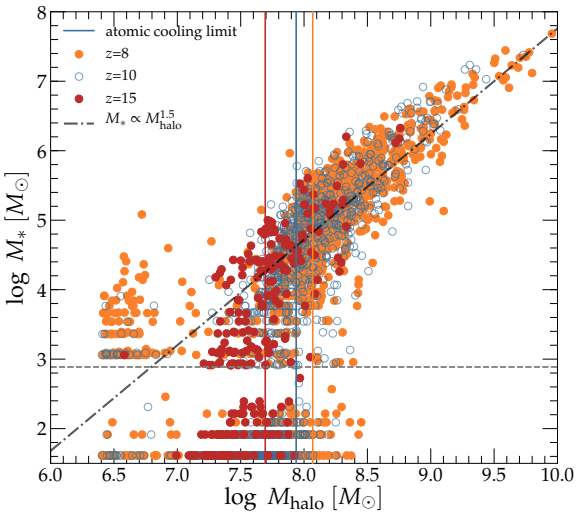


Figure 4.16: Stellar mass to halo mass (SMHM) relation for $z = 8, 10, 15$. The vertical lines correspond to the atomic cooling halo mass for each redshift. Below the atomic cooling limit, we see a deviation from the $M_* \propto M_{\rm halo}^{1.5}$ power law, indicating a lower star formation efficiency in molecular cooling haloes. Note that the power law provides a fit to the $z = 8$ data, for $M_{\rm halo} \geq 10^8\ M_\odot$.

integration limiting magnitude, a single power-law UVLF fit can result in a factor of $> 10$ difference in the estimated SFRD, if one integrates to the luminosity of a single O star. However, at a limiting magnitude of -13, assumed by most observational analyses, the difference is only $\sim 10\%$.

It is interesting to note that, while our cosmic SFRD agrees very well with the estimates provided by Mirocha & Furlanetto (2018), we arrive at this agreement with very different conclusions regarding the faint-end slope of the UVLF. In contrast to our predicted UVLF flattening, their models require a steepening of the UVLF to be consistent with the EDGES measurements. Future observations of the $z$>10 faint-end slope should help to differentiate between the diverging model predictions.

As was the case with results presented in Jaacks et al. (2013), numerical resolution could play a role in identifying a possible UVLF turnover. To address this concern, we consider the study of Wise et al. (2014), who find very similar results to ours. They use the grid-based AMR code ENZO, which is able to add additional levels of grid refinement to areas which require higher spatial resolution, such as regions of star formation. In the highest resolution zones, they achieve a $\sim$ 1 (comoving) pc grid size, and a dark matter particle mass of 1840 $M_{\odot}$. This represents a much higher resolution than the work presented here (see Table 4.1), yet we are finding extremely consistent results (see Fig. 4.8). Therefore, we do not believe that the presences of a turnover in the UVLF is a consequence of insufficient numerical resolution. It is also worth noting that the numerical methodologies used in Jaacks et al. (2013), Wise et al. (2014), and here (i.e. GADGET, ENZO, and GIZMO), represent independent code development and verification streams. This

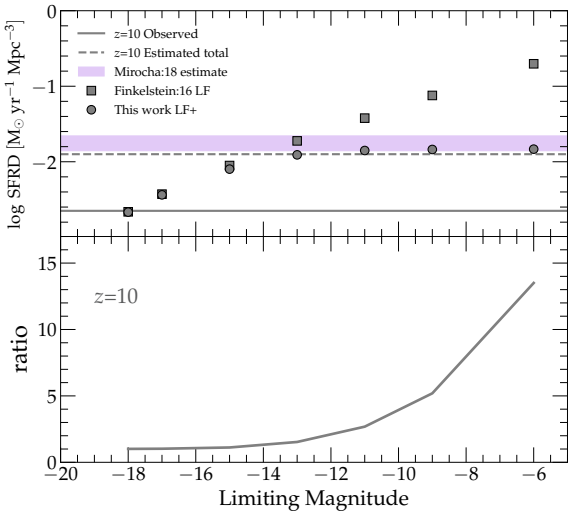


Figure 4.17: Global impact of UVLF turnover. *Top:* Cosmic SFRD, derived by integrating the Finkelstein (2016) $z = 10$ UVLF to a range of limiting magnitudes (gray squares). For comparison, we show the same integration, using a functional form which includes a turnover in the faint-end power law (gray circles; Jaacks et al., 2013). We also reproduce the $z = 10$ estimate, derived from the EDGES constraint (purple shaded region; Mirocha & Furlanetto, 2018). *Bottom:* Boost factor for SFRD in the absence of a turnover. Depending on the integration limiting magnitude, a single power-law UVLF fit, without a turnover, can result in a factor of $> 10$ larger SFRD.

provides additional confidence in the physical robustness of the turnover result.

### 4.5.3 Termination of Pop III

A robust prediction from this work, as well as others (e.g. Johnson et al., 2013; Pallottini et al., 2014; Xu et al., 2016b; Sarmento et al., 2018), is that Pop III star formation continues at a significant rate ($\sim 10^{-3}\ M_{\odot}\mathrm{yr}^{-1}\ \mathrm{Mpc}^{-3}$) at $z \lesssim 8$. While we do not extend our simulation to low enough redshifts to witness its termination, we know that it must end, based on the absence of metal-free star formation in local observations. There are three main mechanisms for terminating Pop III star formation: (1) photo-dissociation of $H_2$/HD by LW radiation, (2) metal enrichment of all high-density gas to $Z > Z_{\mathrm{crit}}$, and (3) photo-ionization of primordial gas. Even though we do not directly simulate the Pop III termination here, we can place constraints on this process with lessons learned in this work.

Lyman-Werner (LW) photons, with energies in the range 11.2 to 13.6 eV, are able to destroy $H_2$/HD via photo-dissociation. With the primary coolants thus destroyed, minihaloes will be unable to cool, collapse and form Pop III stars. As detailed in Jaacks et al. (2018b), we include a model for a global LW radiation background, tied directly to our simulated Pop III/II SFRDs. We also include a mechanism by which gas can self-shield at sufficient densities from the effects of an external LW radiation field (Draine & Bertoldi, 1996). While we notice that the LW background flux does act to suppress low-density gas from cooling, at high densities the self-shielding factor allows for Pop III star formation to continue. This is consistent with high-resolution simulations which find that star formation can

indeed continue in the presence of strong external radiation fields (Maio et al., 2007; Safranek-Shrader et al., 2010).

According to our model, Pop III stars can only form in gas with a metallicity below $Z/Z_{\odot} = 10^{-4} = Z_{\rm crit}$. Once this critical metallicity is reached for all gas in the simulation volume, Pop III star formation will be terminated. However, from Figure 4.10 it is evident that, at $z$=7.5, only a small fraction of the gas in the simulation volume is enriched to beyond $Z_{\rm crit}$ ($\lesssim 10^{-3}$). This indicates that there is still a large reservoir of low-metallicity gas available to fuel ongoing Pop III star formation, consistent with previous studies (e.g. Johnson et al., 2013; Muratov et al., 2013; Pallottini et al., 2014).

A strong UV background (UVB) can also photo-ionize and heat pristine gas, thereby suppressing star formation. As detailed in Section 4.2.2.2, we implement a model for a global UVB with photo-ionization rates adopted from Faucher-Giguère et al. (2009b). The ionization history implicit in this model assumes that the ionization fraction steeply increases, starting at $z \sim 10$, with the Universe being substantially ionized by $z$=6. Therefore, at $z$=7.5, when our simulation ends, the reionization process has only just begun. High-density gas is allowed to self-shield from the UVB, leaving a substantial amount of star-forming gas untouched. We have run low-resolution simulations to below $z \sim 6$, not shown here, to verify that the UVB does indeed suppress Pop III star formation, once reionization is substantially complete.

Based on the high Pop III SFRD found in this work, extending down to $z \lesssim 8$, we suggest that the primary contributor to the termination of Pop III is ultimately

the ionizing UVB, which has yet to ramp up fully in our simulation. However, all three processes discussed above will likely play a role. We plan to quantify their relative contributions in future work.

## 4.6 Summary and conclusions

Building upon our sub-grid model for Pop III legacy star formation (P3L) presented in Jaacks et al. (2018b), we implement a similar Pop II legacy star formation module (P2L) for use in meso-scale cosmological volume simulations. With these star formation models, we study the metal-enrichment and evolution of galaxies in the first billion years of cosmic history by quantifying the individual Pop III and Pop II contributions. We analyze our simulation to make testable predictions for the upcoming *JWST* mission. Our major conclusions are as follows:

- We find that our Pop III peak SFRD$\sim 10^{-3}\ M_{\odot}\mathrm{yr}^{-1}$ is largely unchanged with the addition of Pop II feedback physics, when compared to results in Jaacks et al. (2018b), where metal-enrichment from Pop II was not included. This suggests that continued Pop III star formation is robust even in the presence of ongoing Pop II star formation.

- Our P2L star formation model provides excellent agreement (< factor of 2) with empirical constraints for the total cosmic SFRD at $z = 7.5 - 10$. At $z \gtrsim 10$, we find that our prediction falls within the upper and lower limits of the observation-based estimates (see top panel of Fig. 4.4).

- We find that the Pop II SFRD quickly dominates Pop III by $z \approx 20$. At $z = 7.5$, Pop III stars only contribute $\sim 5\%$ to the total cosmic SFRD. However, their high efficiency of producing ionizing photons allows them to contribute $\sim 20\%$ to the total ionizing emissivity at $z = 7.5$.

- The number densities of our simulated galaxy populations show good agreement with both the observed stellar mass function (SMF), and the UV luminosity function (UVLF) at $z = 8$ and 10. Towards higher redshifts, at $z = 15$, our results are consistent with observations, when extrapolating the faint-end of the observed UVLF with a fixed slope of $\alpha_{\rm UV} = -2.35$.

- Both our simulated SMF and UVLF show strong evidence of deviation from the low mass/faint-end power-law slope. This flattening occurs at $M_{\rm UV,turn} \approx -12, -13.5, -14$, for $z = 8, 10, 15$, respectively, and is strongly correlated with the mass transition between atomic cooling and molecular cooling haloes ($M_* \approx 10^5\ M_\odot$).

- We find that $\lesssim 10^{-3}$ of our simulation volume is enriched beyond $Z_{\rm crit}$ by $z$=7.5, leaving a large reservoir of pristine gas available to fuel ongoing Pop III star formation. Furthermore, $\sim 20\%$ of Pop III star formation at $z$=7.5 is occurring in isolated dark matter haloes which have experienced no Pop II star formation events.

  We are at a remarkable time in the history of astronomy, when we are just about to extend our empirical horizon to the epoch of cosmic dawn, when star and galaxy formation first began. Upcoming observations with frontier

facilities, such as the *JWST* and the suite of extremely large ground-based telescopes, will reveal the crucial transition from initial cosmic simplicity to the proliferating complexity that ensued afterwards. To facilitate this grand observational program, numerical simulations are vital to provide predictions for the underlying model of ΛCDM cosmology. Our simulation presented here is a part of this endeavor, bringing into clearer focus the long-term legacy of cosmic star formation in the early Universe.

There are a number of key lessons. On the one hand, star formation is able to establish pervasive radiation fields early on, in the form of soft (LW) UV radiation prior to reionization. Metal-enrichment from the first stellar generations, on the other hand, leaves behind a dual imprint. Locally, in the highly biased regions of the cosmic web, where star and galaxy formation is taking place, a significant 'bedrock' level of metal enrichment ($\sim 1\%$ solar) is put in place. The sources seen by *JWST* in upcoming deep-field campaigns should thus all already be Pop II systems, with Pop III remaining largely hidden from view. This is an important test of the underlying bottom-up, hierarchical model of structure formation. Globally, in the low-density voids of the early IGM, most of the cosmic volume remains pristine. It is again an important challenge to test this prediction, with next-generation spectroscopic surveys of the diffuse IGM. Overall, we are getting closer to answering one of the fundamental questions in science: What are our cosmic origins, and how did it all begin?

## Acknowledgements

This work was supported by HST-AR-14569.001-A & HST-AR-15028.001 (PI Jaacks), provided by NASA through a grant from the Space Telescope Science Institute, which is operated by the Association of Universities for Research in Astronomy, Inc., under NASA contract NAS5-26555. VB is supported by NSF grant AST-1413501. JJ and SLF acknowledge support from the NASA Astrophysics and Data Analysis Program award #NNX16AN47G issued by JPL/Caltech. This work used the Extreme Science and Engineering Discovery Environment (XSEDE), which is supported by National Science Foundation grant number ACI-1548562, allocation number TG-AST120024. The authors acknowledge the Texas Advanced Computing Center (TACC) at The University of Texas at Austin for providing HPC resources that have contributed to the research results reported within this paper.

# Chapter 5

# Outlook

With this work we have developed a powerful tool for the exploration of the fundamental physical processes which govern the formation of the first stars and galaxies and the subsequent enrichment of the interstellar medium with heavy elements from supernova explosions of first and second generation stars.

In **Chapter 2** we utilize the hydrodynamic and N-body code GIZMO coupled with our newly developed sub-grid Population III Legacy model (P3L), designed specifically for cosmological volume simulations, to study the baseline metal enrichment from Pop III star formation at $z > 7$. In this idealized numerical experiment, we only consider Pop III star formation. We find that our model Pop III star formation rate density (SFRD), which peaks at $\sim 10^{-3}$ $M_{\odot}yr^{-1}Mpc^{-1}$ near $z \sim 10$, agrees well with previous numerical studies and is consistent with the observed estimates for Pop II SFRDs. The mean Pop III metallicity rises smoothly from $z = 25 - 7$, but does not reach the critical metallicity value, $Z_{\rm crit} = 10^{-4}$ $Z_{\odot}$, required for the Pop III to Pop II star formation mode transition until $z \simeq 7$. This suggests that, while individual halos can suppress in-situ Pop III star formation, the external enrichment is insufficient to globally terminate Pop III star formation. The maximum enrichment from Pop III star formation in star forming dark matter

halos is $Z \sim 10^{-2}\ Z_{\odot}$, whereas the minimum found in externally enriched haloes is $Z \gtrsim 10^{-7}\ Z_{\odot}$. Finally, mock observations of our simulated IGM enriched with Pop III metals produce equivalent widths similar to observations of an extremely metal poor damped Lyman alpha (DLA) system at $z = 7.04$, which is thought to be enriched by Pop III star formation only.

In **Chapter 3** we examine the baseline dust extinction in the first galaxies due to Pop III metal enrichment in the first billion years of cosmic history using our newly developed P3L star formation model. We find that while the most enriched, high-density lines of sight in primordial galaxies can experience a measurable amount of extinction from Pop III dust ($E(B-V)_{\rm max} = 0.07,\ A_{\rm V,max} \approx 0.28$), the average extinction is very low with $\langle E(B-V)\rangle \lesssim 10^{-3}$. We derive a power-law relationship between dark matter halo mass and extinction of $E(B-V) \propto M_{\rm halo}^{0.80}$. Performing a Monte Carlo parameter study, we establish the baseline reddening of the UV spectra of dwarf galaxies at high redshift due to Pop III enrichment only. With this method, we find $\langle\beta_{\rm UV}\rangle - 2.51 \pm 0.07$, which is both nearly halo mass and redshift independent.

In **Chapter 5** We utilize the hydrodynamic and N-body code GIZMO, coupled with newly developed sub-grid Legacy models for Population III (Pop III) and Population II (Pop II), specifically designed for meso-scale cosmological volume simulations, to study the legacy of star formation in the pre-reionization Universe. We find that the Pop II star formation rate density (SFRD), produced in our simulation ($\sim 10^{-2}\ M_{\odot}{\rm yr}^{-1}\,{\rm Mpc}^{-3}$ at $z \simeq 10$), matches the total SFRD inferred from observations within a factor of $< 2$ at $7 \lesssim z \lesssim 10$. The Pop III SFRD, on the other hand, reaches a plateau at $\sim 10^{-3}\ M_{\odot}{\rm yr}^{-1}\,{\rm Mpc}^{-3}$ by $z \approx 10$, and remains largely

unaffected by the presence of Pop II feedback. At $z$=7.5, $\sim$ 20% of Pop III star formation occurs in dark matter haloes which are isolated, and have never experienced any Pop II star formation (i.e. primordial haloes). We predict that Pop III-only galaxies exist at magnitudes $M_{\rm UV} \gtrsim -11$, beyond the limits for direct detection with the *James Webb Space Telescope (JWST)*. We assess that our stellar mass function (SMF) and UV luminosity function (UVLF) agree well with the observed low mass/faint-end behaviour at $z = 8$ and 10. However, beyond the current limiting magnitudes, we find that both our SMF and UVLF demonstrate a deviation/turnover from the expected power-law slope ($M_{\rm UV,turn} = -13.4 \pm 1.1$ at $z$=10). Our measured turnover implies that observational studies which integrate their observed luminosity functions by extrapolating the observed faint-end slope beyond their detection limit may overestimate the true SFRD by a factor of 2(10) when integrating to $M_{\rm UV} = -12$ ($-8$) at $z \sim 10$. Our turnover correlates well with the transition from dark matter haloes dominated by molecular cooling to those dominated by atomic cooling, for a mass $M_{\rm halo} \approx 10^8 M_\odot$ at $z \simeq 10$. This confirms previous results which indicate that star formation is more efficient in atomic cooling haloes, due to additional cooling channels and the ability to cool in the presence of strong external radiation fields.

Advancements in the field of galaxy evolution in the first billion years of cosmic evolution are about accelerate. The next generation of space and ground based telescopes are on the horizon and we are about to get a glimpse into a unexplored epoch of our Universe. On its own the *James Webb Space Telescope* (*JWST*), now scheduled to launch in $\sim$ 2020, will extend our current magnitude limit by more than 2 magnitudes. With a boost from gravitational lensing *JWST*

could reach UV magnitudes which are 5-6 magnitudes fainter than current surveys. This incredible increase in depth will allow for the identification of low mass, faint galaxies which were previously undetectable by *HST*, and begin to test the results of this work.

The Giant Magellan Telescope (GMT), which is currently under construction in the Atacama desert of Chile, will see first light in $\sim$ 2024. This 24.5 meter facility will be the a part of the next generation of large ground based telescopes. One of the primary science missions for the GMT is to find and constrain properties of galaxies during the epoch of reionization. The much larger mirror of the GMT will allow for higher light gathering power than the 6.5 meter *JWST* mirror and its spectrograph will be higher resolution with the ability to simultaneously collect light from more targets. However, the GMT will have to contend with atmospheric effects that all ground based telescopes encounter which will mitigate some of these advantages. Even so, GMT will become a valuable tool for future constraints on galaxy evolution and first star formation.

*WFIRST*, the Wide Field InfraRed Survey Telescope is a *HST* sized space based telescope which is scheduled for launch in the mid-2020's. While the primary mirror is a mere 2.4 meters, *WFIRST* will have a a field of view (FOV) which is 100 times greater than *HST*. This huge increase in FOV will allow observers to image more of the Universe in less time. It is estimated that the primary instrument on *WFIRST* will image approximately 1 billion galaxies during it's six year mission. Given the low event rate of Pop III transients, the wide field of view provided by *WFIRST* may give us our best opportunity for observing indirect signatures of Pop III

stars.

The work presented in this dissertation consumed $\sim$ 3 million CPU hours. Therefore, I would be remiss if I did not briefly look at future technologies which have the potential to propel the field of computational astrophysics forward. In this field, research groups rely on merit based allocations of computing time on super computers which are typically NSF funded centers such as the Texas Advanced Computing Center (TACC) used for this work. These publicly funded resources provide peta-scale computing power to researchers in many disciplines (astrophysics, genetics, geophysics, particle physics, etc.) from around the country and the world. Future advancements in the processor speed, and size of computing clusters will certainly reduce the consumption of resources and increase productivity. However, to take full advantage of new computing architecture, advancements much also be made in the programing methods utilized as current generations of hydrodynamical codes do not scale infinitely with infinite processors. The fields of computer science and computational astrophysics will need to overlap in order to make the next leap forward which will allow for larger, higher resolution and more physics rich emulations of our Universe.

# Bibliography

Abel, T., Anninos, P., Zhang, Y., & Norman, M. L. 1997, , 2, 181

Agarwal, B., Johnson, J. L., Khochfar, S., Pellegrini, E., Rydberg, C.-E., Klessen, R. S., & Oesch, P. 2017, MNRAS, 469, 231

Agarwal, B., Johnson, J. L., Zackrisson, E., Labbe, I., van den Bosch, F. C., Natarajan, P., & Khochfar, S. 2016, MNRAS, 460, 4003

Agarwal, B. & Khochfar, S. 2015, MNRAS, 446, 160

Ahn, K. & Shapiro, P. R. 2007, MNRAS, 375, 881

Asplund, M., Grevesse, N., Sauval, A. J., & Scott, P. 2009, ARA&A, 47, 481

Atek, H., Richard, J., Jauzac, M., Kneib, J.-P., Natarajan, P., Limousin, M., Schaerer, D., Jullo, E., Ebeling, H., Egami, E., & Clement, B. 2015, ApJ, 814, 69

Barrow, K. S. S., Wise, J. H., Norman, M. L., O'Shea, B. W., & Xu, H. 2017, MNRAS, 469, 4863

Behroozi, P. S., Marchesini, D., Wechsler, R. H., Muzzin, A., Papovich, C., & Stefanon, M. 2013, ApJL, 777, L10

Bergin, E. A. & Tafalla, M. 2007, ARA&A, 45, 339

Birnboim, Y. & Dekel, A. 2003, MNRAS, 345, 349

Bohlin, R. C., Savage, B. D., & Drake, J. F. 1978, ApJ, 224, 132

Bouwens, R. J., Bradley, L., Zitrin, A., Coe, D., Franx, M., Zheng, W., Smit, R., & Host, O. 2014, ApJ, 795, 126

Bouwens, R. J., Illingworth, G. D., Blakeslee, J. P., & Franx, M. 2006, ApJ, 653, 53

Bouwens, R. J., Illingworth, G. D., Oesch, P. A., Labbé, I., Trenti, M., van Dokkum, P., Franx, M., Stiavelli, M., Carollo, C. M., Magee, D., & Gonzalez, V. 2011, ApJ, 737, 90

Bouwens, R. J., Illingworth, G. D., Oesch, P. A., Stiavelli, M., van Dokkum, P., Trenti, M., Magee, D., Labbé, I., et al. 2010a, ApJL, 709, L133

Bouwens, R. J., Illingworth, G. D., Oesch, P. A., Trenti, M., Labbé, I., Bradley, L., Carollo, M., & van Dokkum, P. G. 2015, ApJ, 803, 34

Bouwens, R. J., Illingworth, G. D., Oesch, P. A., Trenti, M., Labbe, I., Franx, M., Stiavelli, M., & Carollo, C. M. 2012, ApJL, 752, L5

Bouwens, R. J., Illingworth, G. D., Oesch, P. A., Trenti, M., Stiavelli, M., Carollo, C. M., Franx, M., van Dokkum, P. G., Labbé, I., & Magee, D. 2010b, ApJL, 708, L69

Bouwens, R. J., Oesch, P. A., Illingworth, G. D., Ellis, R. S., & Stefanon, M. 2017, ApJ, 843, 129

Bouwens, R. J., Oesch, P. A., Labbé, I., Illingworth, G. D., Fazio, G. G., Coe, D., Holwerda, B., & Smit, R. 2016, ApJ, 830, 67

Bowler, R. A. A., Dunlop, J. S., McLure, R. J., Rogers, A. B., McCracken, H. J., Milvang-Jensen, B., Furusawa, H., & Fynbo, J. P. U. 2014, MNRAS, 440, 2810

Bowler, R. A. A., McLure, R. J., Dunlop, J. S., McLeod, D. J., Stanway, E. R., Eldridge, J. J., & Jarvis, M. J. 2017, MNRAS, 469, 448

Bowman, J. D., Rogers, A. E. E., Monsalve, R. A., Mozdzen, T. J., & Mahesh, N. 2018, Nature, 555, 67

Boylan-Kolchin, M., Bullock, J. S., & Garrison-Kimmel, S. 2014, MNRAS, 443, L44

Boylan-Kolchin, M., Weisz, D. R., Johnson, B. D., Bullock, J. S., Conroy, C., & Fitts, A. 2015, MNRAS, 453, 1503

Bromm, V., Coppi, P. S., & Larson, R. B. 2002, ApJ, 564, 23

Bromm, V., Ferrara, A., Coppi, P. S., & Larson, R. B. 2001a, MNRAS, 328, 969

Bromm, V., Kudritzki, R. P., & Loeb, A. 2001b, ApJ, 552, 464

—. 2001c, ApJ, 552, 464

Bromm, V. & Loeb, A. 2003a, ApJ, 596, 34

—. 2003b, Nature, 425, 812

—. 2006, ApJ, 642, 382

Bromm, V. & Yoshida, N. 2011, ARA&A, 49, 373

Cai, Z., Fan, X., Jiang, L., Bian, F., McGreer, I., Davé, R., Egami, E., Zabludoff, A., Yang, Y., & Oh, S. P. 2011, ApJL, 736, L28

Calzetti, D., Armus, L., Bohlin, R. C., Kinney, A. L., Koornneef, J., & Storchi-Bergmann, T. 2000, ApJ, 533, 682

Campisi, M. A., Maio, U., Salvaterra, R., & Ciardi, B. 2011, MNRAS, 416, 2760

Carr, B. J., Bond, J. R., & Arnett, W. D. 1984, ApJ, 277, 445

Cassata, P., Le Fèvre, O., Charlot, S., Contini, T., Cucciati, O., Garilli, B., Zamorani, G., Adami, C., Bardelli, S., Le Brun, V., Lemaux, B., Maccagni, D., Pollo, A., Pozzetti, L., Tresse, L., Vergani, D., Zanichelli, A., & Zucca, E. 2013, A&A, 556, A68

Cen, R. 1992, ApJS, 78, 341

Cen, R. & Riquelme, M. A. 2008, ApJ, 674, 644

Chabrier, G. 2003, PASP, 115, 763

Chabrier, G., Hennebelle, P., & Charlot, S. 2014, ApJ, 796, 75

Cooke, R. J., Pettini, M., Nollett, K. M., & Jorgenson, R. 2016, ApJ, 830, 148

Dayal, P., Dunlop, J. S., Maio, U., & Ciardi, B. 2013, MNRAS, 434, 1486

Dekel, A. & Birnboim, Y. 2006, MNRAS, 368, 2

Dekel, A. & Silk, J. 1986, ApJ, 303, 39

Draine, B. T. 2011, Physics of the Interstellar and Intergalactic Medium by Bruce T. Draine. Princeton University Press, Princeton, NJ

Draine, B. T. & Bertoldi, F. 1996, ApJ, 468, 269

Dunlop, J. S., McLure, R. J., Robertson, B. E., Ellis, R. S., Stark, D. P., Cirasuolo, M., & de Ravel, L. 2012, MNRAS, 420, 901

Dunlop, J. S., Rogers, A. B., McLure, R. J., Ellis, R. S., Robertson, B. E., Koekemoer, A., Dayal, P., Curtis-Lake, E., Wild, V., Charlot, S., Bowler, R. A. A., Schenker, M. A., Ouchi, M., Ono, Y., Cirasuolo, M., Furlanetto, S. R., Stark, D. P., Targett, T. A., & Schneider, E. 2013, MNRAS, 432, 3520

Evans, II, N. J., Dunham, M. M., Jørgensen, J. K., Enoch, M. L., Merín, B., van Dishoeck, E. F., Alcalá, J. M., Myers, P. C., Stapelfeldt, K. R., Huard, T. L., Allen, L. E., Harvey, P. M., van Kempen, T., Blake, G. A., Koerner, D. W., Mundy, L. G., Padgett, D. L., & Sargent, A. I. 2009, ApJS, 181, 321

Faucher-Giguère, C.-A., Lidz, A., Zaldarriaga, M., & Hernquist, L. 2009a, ApJ, 703, 1416

—. 2009b, ApJ, 703, 1416

Feng, Y., Di-Matteo, T., Croft, R. A., Bird, S., Battaglia, N., & Wilkins, S. 2016, MNRAS, 455, 2778

Finkelstein, S., Dickinson, M., Ferguson, H., Grazian, A., Grogin, N., Kartaltepe, J., Kewley, L., Kocevski, D., Koekemoer, A., Lotz, J., Papovich, C., Pentericci, L.,

Perez-Gonzalez, P., Pirzkal, N., Ravindranath, S., Somerville, R., Trump, J., & Wilkins, S. 2017, The Cosmic Evolution Early Release Science (CEERS) Survey, JWST Proposal ID 1345. Cycle 0 Early Release Science

Finkelstein, S. L. 2016, PASA, 33, e037

Finkelstein, S. L., Papovich, C., Giavalisco, M., Reddy, N. A., Ferguson, H. C., Koekemoer, A. M., & Dickinson, M. 2010, ApJ, 719, 1250

Finkelstein, S. L., Papovich, C., Ryan, R. E., Pawlik, A. H., Dickinson, M., Ferguson, H. C., Finlator, K., & Koekemoer, A. M. 2012a, ApJ, 758, 93

Finkelstein, S. L., Papovich, C., Salmon, B., Finlator, K., Dickinson, M., Ferguson, H. C., Giavalisco, M., Koekemoer, A. M., Reddy, N. A., Bassett, R., Conselice, C. J., Dunlop, J. S., Faber, S. M., Grogin, N. A., Hathi, N. P., Kocevski, D. D., Lai, K., Lee, K.-S., McLure, R. J., Mobasher, B., & Newman, J. A. 2012b, ApJ, 756, 164

Finkelstein, S. L., Ryan, Jr., R. E., Papovich, C., Dickinson, M., Song, M., Somerville, R. S., Ferguson, H. C., & Salmon, B. 2015, ApJ, 810, 71

Finlator, K., Oppenheimer, B. D., & Davé, R. 2011, MNRAS, 410, 1703

Fraser, M., Casey, A. R., Gilmore, G., Heger, A., & Chan, C. 2017, MNRAS, 468, 418

Galli, D. & Palla, F. 1998, A&A, 335, 403

Genel, S., Vogelsberger, M., Springel, V., Sijacki, D., Nelson, D., Snyder, G., Rodriguez-Gomez, V., Torrey, P., & Hernquist, L. 2014, MNRAS, 445, 175

Greif, T. H. & Bromm, V. 2006, MNRAS, 373, 128

Greif, T. H., Johnson, J. L., Bromm, V., & Klessen, R. S. 2007, ApJ, 670, 1

Greif, T. H., Johnson, J. L., Klessen, R. S., & Bromm, V. 2008, MNRAS, 387, 1021

Greif, T. H., Springel, V., White, S. D. M., Glover, S. C. O., Clark, P. C., Smith, R. J., Klessen, R. S., & Bromm, V. 2011, ApJ, 737, 75

Hahn, O. & Abel, T. 2011, MNRAS, 415, 2101

Heger, A. & Woosley, S. E. 2002, ApJ, 567, 532

—. 2010, ApJ, 724, 341

Hirano, S., Hosokawa, T., Yoshida, N., Umeda, H., Omukai, K., Chiaki, G., & Yorke, H. W. 2014, ApJ, 781, 60

Hollenbach, D. & McKee, C. F. 1989, ApJ, 342, 306

Hopkins, P. F. 2015, MNRAS, 450, 53

Hopkins, P. F., Quataert, E., & Murray, N. 2012, MNRAS, 421, 3522

Hummel, J. A., Pawlik, A. H., Milosavljević, M., & Bromm, V. 2012, ApJ, 755, 72

Iliev, I. T., Mellema, G., Shapiro, P. R., & Pen, U.-L. 2007, MNRAS, 376, 534

Ishigaki, M., Kawamata, R., Ouchi, M., Oguri, M., Shimasaku, K., & Ono, Y. 2015, ApJ, 799, 12

Jaacks, J., Choi, J.-H., Nagamine, K., Thompson, R., & Varghese, S. 2012a, MNRAS, 420, 1606

Jaacks, J., Finkelstein, S. L., & Bromm, V. 2018a, MNRAS, 475, 3883

Jaacks, J., Nagamine, K., & Choi, J. H. 2012b, MNRAS, 427, 403

Jaacks, J., Thompson, R., Finkelstein, S. L., & Bromm, V. 2018b, MNRAS, 475, 4396

Jaacks, J., Thompson, R., & Nagamine, K. 2013, ApJ, 766, 94

Jeon, M., Besla, G., & Bromm, V. 2017, ApJ, 848, 85

Jeon, M., Bromm, V., Pawlik, A. H., & Milosavljević, M. 2015, MNRAS, 452, 1152

Jeon, M., Pawlik, A. H., Bromm, V., & Milosavljević, M. 2014, MNRAS, 444, 3288

Johnson, J. L. & Bromm, V. 2006, MNRAS, 366, 247

Johnson, J. L., Dalla Vecchia, C., & Khochfar, S. 2013, MNRAS, 428, 1857

Johnson, J. L., Greif, T. H., & Bromm, V. 2008, MNRAS, 388, 26

Karlsson, T., Bromm, V., & Bland-Hawthorn, J. 2013, Reviews of Modern Physics, 85, 809

Kehrig, C., Vílchez, J. M., Pérez-Montero, E., Iglesias-Páramo, J., Brinchmann, J., Kunth, D., Durret, F., & Bayo, F. M. 2015, ApJL, 801, L28

Kennicutt, Jr., R. C. 1998, ARA&A, 36, 189

Kereš, D., Katz, N., Weinberg, D. H., & Davé, R. 2005, MNRAS, 363, 2

Kitayama, T. & Yoshida, N. 2005, ApJ, 630, 675

Kroupa, P. 2001, MNRAS, 322, 231

Krumholz, M. R. & Tan, J. C. 2007, ApJ, 654, 304

Larson, R. B. 1998, MNRAS, 301, 569

Leitherer, C., Schaerer, D., Goldader, J. D., Delgado, R. M. G., Robert, C., Kune, D. F., de Mello, D. F., Devost, D., & Heckman, T. M. 1999, ApJS, 123, 3

Liu, B. & Bromm, V. 2018, MNRAS, 476, 1826

Livermore, R. C., Finkelstein, S. L., & Lotz, J. M. 2017, ApJ, 835, 113

Ma, X., Hopkins, P. F., Garrison-Kimmel, S., Faucher-Giguère, C.-A., Quataert, E., Boylan-Kolchin, M., Hayward, C. C., Feldmann, R., & Kereš, D. 2017, ArXiv e-prints

Mackey, J., Bromm, V., & Hernquist, L. 2003, ApJ, 586, 1

Madau, P. & Dickinson, M. 2014, ARA&A, 52, 415

Maio, U., Ciardi, B., Dolag, K., Tornatore, L., & Khochfar, S. 2010, MNRAS, 407, 1003

Maio, U., Dolag, K., Ciardi, B., & Tornatore, L. 2007, MNRAS, 379, 963

Mancini, M., Schneider, R., Graziani, L., Valiante, R., Dayal, P., Maio, U., Ciardi, B., & Hunt, L. K. 2015, MNRAS, 451, L70

Maoz, D., Mannucci, F., & Brandt, T. D. 2012, MNRAS, 426, 3282

Matthee, J., Sobral, D., Boone, F., Röttgering, H., Schaerer, D., Girard, M., Pallottini, A., Vallini, L., Ferrara, A., Darvish, B., & Mobasher, B. 2017, ApJ, 851, 145

Mattsson, L., De Cia, A., Andersen, A. C., & Zafar, T. 2014, MNRAS, 440, 1562

McKee, C. F. & Ostriker, E. C. 2007, ARA&A, 45, 565

McLeod, D. J., McLure, R. J., & Dunlop, J. S. 2016, MNRAS, 459, 3812

McLeod, D. J., McLure, R. J., Dunlop, J. S., Robertson, B. E., Ellis, R. S., & Targett, T. A. 2015, MNRAS, 450, 3032

McLure, R. J., Cirasuolo, M., Dunlop, J. S., Foucaud, S., & Almaini, O. 2009, MNRAS, 395, 2196

McLure, R. J., Dunlop, J. S., Bowler, R. A. A., Curtis-Lake, E., Schenker, M., Ellis, R. S., Robertson, B. E., & Koekemoer, A. M. 2013, MNRAS, 432, 2696

McLure, R. J., Dunlop, J. S., de Ravel, L., Cirasuolo, M., Ellis, R. S., Schenker, M., Robertson, B. E., Koekemoer, A. M., Stark, D. P., & Bowler, R. A. A. 2011, MNRAS, 418, 2074

Mesinger, A. & Dijkstra, M. 2008, MNRAS, 390, 1071

Meurer, G. R., Heckman, T. M., & Calzetti, D. 1999, ApJ, 521, 64

Mirocha, J. & Furlanetto, S. R. 2018, ArXiv e-prints

Morton, D. C. 2003, ApJS, 149, 205

Muratov, A. L., Gnedin, O. Y., Gnedin, N. Y., & Zemp, M. 2013, ApJ, 773, 19

Murray, N. 2011, ApJ, 729, 133

Navarro, J. F., Frenk, C. S., & White, S. D. M. 1997, ApJ, 490, 493

Nomoto, K., Kobayashi, C., & Tominaga, N. 2013, ARA&A, 51, 457

Oesch, P. A., Bouwens, R. J., Illingworth, G. D., Labbé, I., Franx, M., van Dokkum, P. G., Trenti, M., Stiavelli, M., Gonzalez, V., & Magee, D. 2013, ApJ, 773, 75

Oesch, P. A., Bouwens, R. J., Illingworth, G. D., Labbé, I., Smit, R., Franx, M., van Dokkum, P. G., & Momcheva, I. 2014, ApJ, 786, 108

Oesch, P. A., Bouwens, R. J., Illingworth, G. D., Labbé, I., & Stefanon, M. 2018, ApJ, 855, 105

Oesch, P. A., Brammer, G., van Dokkum, P. G., Illingworth, G. D., Bouwens, R. J., Labbé, I., Franx, M., & Momcheva, I. 2016, ApJ, 819, 129

Oesch, P. A., Carollo, C. M., Stiavelli, M., Trenti, M., Bergeron, L. E., Koekemoer, A. M., Lucas, R. A., Pavlovsky, C. M., et al. 2009, ApJ, 690, 1350

Okamoto, T., Gao, L., & Theuns, T. 2008, MNRAS, 390, 920

Omukai, K., Hosokawa, T., & Yoshida, N. 2010, ApJ, 722, 1793

Oppenheimer, B. D. & Davé, R. 2006, MNRAS, 373, 1265

O'Shea, B. W., Wise, J. H., Xu, H., & Norman, M. L. 2015, ApJL, 807, L12

Ouchi, M., Mobasher, B., Shimasaku, K., Ferguson, H. C., Fall, S. M., Ono, Y., Kashikawa, N., & Morokuma, T. 2009, ApJ, 706, 1136

Paardekooper, J.-P., Khochfar, S., & Dalla Vecchia, C. 2013, MNRAS, 429, L94

—. 2015, MNRAS, 451, 2544

Pacucci, F., Pallottini, A., Ferrara, A., & Gallerani, S. 2017, MNRAS, 468, L77

Pallottini, A., Ferrara, A., Gallerani, S., Salvadori, S., & D'Odorico, V. 2014, MNRAS, 440, 2498

Pallottini, A., Ferrara, A., Pacucci, F., Gallerani, S., Salvadori, S., Schneider, R., Schaerer, D., Sobral, D., & Matthee, J. 2015, MNRAS, 453, 2465

Papovich, C., Finkelstein, S. L., Ferguson, H. C., Lotz, J. M., & Giavalisco, M. 2011, MNRAS, 412, 1123

Pawlik, A. H., Milosavljević, M., & Bromm, V. 2011, ApJ, 731, 54

Planck Collaboration, Ade, P. A. R., Aghanim, N., Arnaud, M., Ashdown, M., Aumont, J., Baccigalupi, C., Banday, A. J., Barreiro, R. B., Bartlett, J. G., & et al. 2016, A&A, 594, A13

Price, D. J. 2007, PASA, 24, 159

Rachford, B. L., Snow, T. P., Destree, J. D., Ross, T. L., Ferlet, R., Friedman, S. D., Gry, C., Jenkins, E. B., Morton, D. C., Savage, B. D., Shull, J. M., Sonnentrucker, P., Tumlinson, J., Vidal-Madjar, A., Welty, D. E., & York, D. G. 2009, ApJS, 180, 125

Rafelski, M., Neeleman, M., Fumagalli, M., Wolfe, A. M., & Prochaska, J. X. 2014, ApJL, 782, L29

Reddy, N., Dickinson, M., Elbaz, D., Morrison, G., Giavalisco, M., Ivison, R., Papovich, C., Scott, D., Buat, V., Burgarella, D., Charmandaris, V., Daddi, E., Magdis, G., Murphy, E., Altieri, B., Aussel, H., Dannerbauer, H., Dasyra, K., Hwang, H. S., Kartaltepe, J., Leiton, R., Magnelli, B., & Popesso, P. 2012, ApJ, 744, 154

Ricotti, M. & Ostriker, J. P. 2004, MNRAS, 350, 539

Ritter, J. S., Safranek-Shrader, C., Gnat, O., Milosavljević, M., & Bromm, V. 2012, ApJ, 761, 56

Robertson, B. E. & Ellis, R. S. 2012, ApJ, 744, 95

Robertson, B. E., Ellis, R. S., Furlanetto, S. R., & Dunlop, J. S. 2015, ApJL, 802, L19

Safranek-Shrader, C., Agarwal, M., Federrath, C., Dubey, A., Milosavljević, M., & Bromm, V. 2012, MNRAS, 426, 1159

Safranek-Shrader, C., Bromm, V., & Milosavljević, M. 2010, ApJ, 723, 1568

Salpeter, E. E. 1955, ApJ, 121, 161

Salvaterra, R., Ferrara, A., & Dayal, P. 2011, MNRAS, 414, 847

Santoro, F. & Shull, J. M. 2006, ApJ, 643, 26

Sarmento, R., Scannapieco, E., & Cohen, S. 2018, ApJ, 854, 75

Scannapieco, E., Madau, P., Woosley, S., Heger, A., & Ferrara, A. 2005, ApJ, 633, 1031

Schaerer, D. 2002, A&A, 382, 28

—. 2003a, A&A, 397, 527

—. 2003b, A&A, 397, 527

Schechter, P. 1976, ApJ, 203, 297

Schenker, M. A., Robertson, B. E., Ellis, R. S., Ono, Y., McLure, R. J., Dunlop, J. S., Koekemoer, A., Bowler, R. A. A., Ouchi, M., Curtis-Lake, E., Rogers, A. B., Schneider, E., Charlot, S., Stark, D. P., Furlanetto, S. R., & Cirasuolo, M. 2013, ApJ, 768, 196

Schmidt, K. B., Treu, T., Trenti, M., Bradley, L. D., Kelly, B. C., Oesch, P. A., Holwerda, B. W., Shull, J. M., & Stiavelli, M. 2014, ApJ, 786, 57

Schneider, R., Ferrara, A., Natarajan, P., & Omukai, K. 2002, ApJ, 571, 30

Schneider, R., Hunt, L., & Valiante, R. 2016, MNRAS, 457, 1842

Schneider, R., Omukai, K., Bianchi, S., & Valiante, R. 2012, MNRAS, 419, 1566

Sedov, L. I. 1959, Similarity and Dimensional Methods in Mechanics

Shimizu, I., Inoue, A. K., Okamoto, T., & Yoshida, N. 2014, MNRAS, 440, 731

Simcoe, R. A., Sullivan, P. W., Cooksey, K. L., Kao, M. M., Matejek, M. S., & Burgasser, A. J. 2012, Nature, 492, 79

Sluder, A., Ritter, J. S., Safranek-Shrader, C., Milosavljević, M., & Bromm, V. 2016, MNRAS, 456, 1410

Smith, A., Becerra, F., Bromm, V., & Hernquist, L. 2017, MNRAS, 472, 205

Smith, A., Bromm, V., & Loeb, A. 2016, MNRAS, 460, 3143

Smith, B. D., Wise, J. H., O'Shea, B. W., Norman, M. L., & Khochfar, S. 2015, Monthly Notices of the Royal Astronomical Society, 452, 2822

Sobral, D., Matthee, J., Brammer, G., Ferrara, A., Alegre, L., Rottgering, H., Schaerer, D., Mobasher, B., & Darvish, B. 2017, ArXiv e-prints

Sobral, D., Matthee, J., Darvish, B., Schaerer, D., Mobasher, B., Röttgering, H. J. A., Santos, S., & Hemmati, S. 2015, ApJ, 808, 139

Somerville, R. S. & Davé, R. 2015, ARA&A, 53, 51

Song, M., Finkelstein, S. L., Ashby, M. L. N., Grazian, A., Lu, Y., Papovich, C., Salmon, B., Somerville, R. S., Dickinson, M., Duncan, K., Faber, S. M., Fazio, G. G., Ferguson, H. C., Fontana, A., Guo, Y., Hathi, N., Lee, S.-K., Merlin, E., & Willner, S. P. 2016, ApJ, 825, 5

Spitzer, L. 1978, Physical processes in the interstellar medium

Springel, V. & Hernquist, L. 2003, MNRAS, 339, 289

Stacy, A. & Bromm, V. 2013, MNRAS, 433, 1094

Stacy, A., Bromm, V., & Lee, A. T. 2016, MNRAS, 462, 1307

Stacy, A., Greif, T. H., & Bromm, V. 2010, MNRAS, 403, 45

Taylor, G. 1950, Royal Society of London Proceedings Series A, 201, 175

The Enzo Collaboration, Bryan, G. L., & Norman, M. L. 2014, ApJS, 211, 19

Thompson, R. 2014, pyGadgetReader: GADGET snapshot reader for python, Astrophysics Source Code Library

Thompson, R., Nagamine, K., Jaacks, J., & Choi, J.-H. 2014, ApJ, 780, 145

Tornatore, L., Ferrara, A., & Schneider, R. 2007, MNRAS, 382, 945

Trenti, M., Bradley, L. D., Stiavelli, M., Oesch, P., Treu, T., Bouwens, R. J., Shull, J. M., & MacKenty, J. W. 2011, ApJL, 727, L39

Trenti, M., Perna, R., Levesque, E. M., Shull, J. M., & Stocke, J. T. 2012, ApJL, 749, L38

Trenti, M., Stiavelli, M., Bouwens, R. J., Oesch, P., Shull, J. M., Illingworth, G. D., Bradley, L. D., & Carollo, C. M. 2010, ApJL, 714, L202

Tumlinson, J. & Shull, J. M. 2000, ApJL, 528, L65

Turk, M. J., Abel, T., & O'Shea, B. 2009, Science, 325, 601

Turk, M. J., Smith, B. D., Oishi, J. S., Skory, S., Skillman, S. W., Abel, T., & Norman, M. L. 2011, ApJS, 192, 9

Wang, F. Y. 2013, A&A, 556, A90

Wang, F. Y., Bromm, V., Greif, T. H., Stacy, A., Dai, Z. G., Loeb, A., & Cheng, K. S. 2012, ApJ, 760, 27

Weinmann, S. M. & Lilly, S. J. 2005, ApJ, 624, 526

White, S. D. M. & Frenk, C. S. 1991, ApJ, 379, 52

White, S. D. M. & Rees, M. J. 1978, MNRAS, 183, 341

Wiersma, R. P. C., Schaye, J., & Smith, B. D. 2009, MNRAS, 393, 99

Wilkins, S. M., Bouwens, R. J., Oesch, P. A., Labbé, I., Sargent, M., Caruana, J., Wardlow, J., & Clay, S. 2016, MNRAS, 455, 659

Wilkins, S. M., Bunker, A. J., Lorenzoni, S., & Caruana, J. 2011, MNRAS, 411, 23

Wilkins, S. M., Coulton, W., Caruana, J., Croft, R., di Matteo, T., Khandai, N., Feng, Y., Bunker, A., & Elbert, H. 2013, MNRAS, 435, 2885

Wise, J. H. & Abel, T. 2005, ApJ, 629, 615

—. 2007, ApJ, 671, 1559

Wise, J. H., Demchenko, V. G., Halicek, M. T., Norman, M. L., Turk, M. J., Abel, T., & Smith, B. D. 2014, MNRAS, 442, 2560

Wise, J. H., Turk, M. J., Norman, M. L., & Abel, T. 2012, ApJ, 745, 50

Wolcott-Green, J. & Haiman, Z. 2011, MNRAS, 412, 2603

Xu, H., Ahn, K., Norman, M. L., Wise, J. H., & O'Shea, B. W. 2016a, ApJL, 832, L5

Xu, H., Norman, M. L., O'Shea, B. W., & Wise, J. H. 2016b, ApJ, 823, 140

Yan, H.-J., Windhorst, R. A., Hathi, N. P., Cohen, S. H., Ryan, R. E., O'Connell, R. W., & McCarthy, P. J. 2010, Research in Astronomy and Astrophysics, 10, 867

Yoshida, N., Abel, T., Hernquist, L., & Sugiyama, N. 2003, ApJ, 592, 645

Yoshida, N., Bromm, V., & Hernquist, L. 2004, ApJ, 605, 579

Yue, B., Ferrara, A., & Xu, Y. 2016, MNRAS, 463, 1968

Yung, L. Y. A., Somerville, R. S., Finkelstein, S. L., Popping, G., & Davé, R. 2018, ArXiv e-prints

Zackrisson, E., Binggeli, C., Finlator, K., Gnedin, N. Y., Paardekooper, J.-P., Shimizu, I., Inoue, A. K., Jensen, H., Micheva, G., Khochfar, S., & Dalla Vecchia, C. 2017, ApJ, 836, 78

Zackrisson, E., Inoue, A. K., & Jensen, H. 2013, ApJ, 777, 39